ELECTRIC AND FERROELECTRIC CONTROL OF ELECTRONIC AND MAGNETIC PROPERTIES OF OXIDE HETEROSTRUCTURES

WENXIONG ZHOU

NATIONAL UNIVERSITY OF SINGAPORE

2016

ELECTRIC AND FERROELECTRIC CONTROL OF ELECTRONIC AND MAGNETIC PROPERTIES OF OXIDE HETEROSTRUCTURES

WENXIONG ZHOU

(*B. SC. SICHUAN UNIVERSITY, CHINA*)

A THEIS SUBMITTED FOR THE DEGREE OF DOCTOR OF PHILOSOPHY IN SCIENCE

DEPARTMENT OF PHYSICS

NATIONAL UNIVERSITY OF SINGAPORE

2016

DECLARATION

I hereby declare that the thesis is my original work and it has been written by me in its entirety. I have duly acknowledged all the sources of information which have been used in this thesis.

This thesis has also not been submitted for any degree in any university previously.

_____ _____

Wenxiong Zhou

11 April 2016

ACKNOWLEDGEMENTS

Looking back at the past four years of my PhD study, it's been a fulfilling and memorable journey. I am so lucky to have so many kind and brilliant people who accompanied me through the hardships and joys, frustrations and excitements, tears and laughter. Here, I would like to take this opportunity to express my gratitude to these lovely people.

First of all, I would like to thank my supervisor Prof. Ariando. Thanks to Ariando for his efforts in supervising my study and research over the past four years. Thanks for being so kind and patient with me. Honestly, PhD study was never easy for me, however, his kindness and patience served as great consolation. Thanks for giving me so much freedom and supporting my research unconditionally. Thanks for guiding me through these frustrations and hardships. I still remember those times, when he helped me to revise my slides and rehearsed with me until midnights for the oral presentations during 2016 MRS spring meeting held in Phoenix, United states. He showed me by himself the meaning of being professional and hard-working. Thanks for everything!

I would also like to thank Prof. T. Venkatesan for his support and assistance during my PhD study. His passion about science and research would always inspire me. Talking with him is also fun and informative. Thanks to Venky for making NUSNNI-NanoCore like a big family.

I would also like to thank Prof. Chen Jingsheng and Prof. J. M. D. Coey for their help with my experiments and discussing the data with us.

Miss Alina Gales, Mr. Wu Yuping, Mr. Peter Stutz, Mr. Aian Rosales and Mrs. Ivy Rosales, the first year in Singapore with you guys was so fun and amazing.

Last and most importantly, I would like to thank my parents and my family, thank you and love you so much for your love, not only during my PhD study but throughout my whole life.

TABLE OF CONTENTS

VIII

ABSTRACT

Complex oxides host a wide variety of exotic physical properties, such as ferromagnetism, superconductivity and ferroelectricity, due to the strong correlation and delicate balance between charge, spin, orbit and lattice. The thin films, interfaces and heterostructures composed of these complex oxides show even more intriguing properties due to symmetry breaking at the interface and are promising for future multifunctional electronics. For practical applications, it is important to unveil the origin of these properties and control them with external stimuli.

In this thesis, we study the origins of electronic and magnetic properties of oxide heterostructures and tune them with electric and ferroelectric field effect. Compared to other modulation techniques, electric and ferroelectric modulations are of particular interest as they do not cause any structural or chemical changes. Firstly, we show soft phonon induced electronic transport anomaly at the cubic-to-tetragonal phase transition temperature in n-type $SrTiO_3$, which is the "silicon" of oxide electronics. As far as we know, this electron-soft phonon scattering in $SrTiO_3$ is explicitly shown for the first time. These results shall provide some new insights into the conduction mechanism in n-type $SrTiO_3$. Next, we study ferroelectric control of the two-dimensional electron gas in a $LaAlO_3/Ba_xSr_{1-x}TiO_3/SrTiO_3$ heterostructure. We find that the conductivity of the two-dimensional electron gas can be systematically controlled by varying the thickness of the ferroelectric $Ba_xSr_{1-x}TiO_3$ layer. In addition, we show the coexistence of ferroelectricity and two-dimensional electron gas in this heterostructure by observing the interaction between the

depolarization field of $Ba_xSr_{1-x}TiO_3$ and the built-in electric field of $LaAlO_3$. Our approach provides an alternate route to control the two-dimensional electron gas with ferroelectricity. On the other hand, these results also provide evidence for the coexistence of two seemly incompatible properties (ferroelectricity and two-dimensional electron gas). Finally, we study ferroelectric control of the magnetic properties of Pt thin films in a $Pt/BaTiO_3/SrTiO_3$ heterostructure. Ferromagnetism was found in Pt thin films by electric and magnetic measurements, as well as first-principles calculations. The unusual ferromagnetism was found to be induced by ferroelectric $BaTiO_3$. These results provide a new routine to tune an otherwise paramagnetic material into ferromagnetic with ferroelectricity.

LIST OF PUBLICATIONS

1. <u>W. X. Zhou</u>, J. Zhou, S. W. Zeng, Z. Huang, C. J. Li, H. J. H. Ma, K. Han, Z. S. Lim, D. Y. Wan, L. C. Zhang, T. Venkatesan, Y. P. Feng and Ariando, "Electron-soft phonon scattering in n-type $SrTiO_3$" ***Phys. Rev. B***, 94, 195122 (2016).

2. <u>W. X. Zhou</u>, S. W. Zeng, J. Zhou, C. J. Li, R. Guo, J. X. Xiao, Z. Huang, W. M. Lü, H. J. H. Ma, K. Han, P. Yang, D. Y. Wan, K. Y. Zeng, J. S. Chen, T. Venkatesan, Y. P. Feng and Ariando, "Coexistence of ferroelectricity and two-dimensional electron gas" (under preparation).

3. Z. Huang, K. Han, S. W. Zeng, M. Motapothula, A. Y. Borisevich, S. Ghosh, W. M. Lü, C. J. Li, <u>W. X. Zhou</u>, Z. Q. Liu, J. M. D. Coey, T. Venkatesan and Ariando, "The effect of polar fluctuation and lattice mismatch on carrier mobility at oxide interfaces" **Nano Letters**, 16, 2307 (2016).

4. S. W. Zeng, W. M. Lü, Z. Huang, Z. Q. Liu, K. Han, K. Gopinadhan, C. J. Li, R. Guo, <u>W. X. Zhou</u>, H. J. H. Ma, L. Jian, T. Venkatesan and Ariando, "Liquid-gated high mobility and quantum oscillation of the two-dimensional electron gas at an oxide interface" **ACS Nano** 10, 4532 (2016).

5. K. Han, N. Palina, S. W. Zeng, Z. Huang, C. J. Li, <u>W. X. Zhou</u>, D. Y. Wan, L. C. Zhang, X. Chi, R. Guo, J. S. Chen, T. Venkatesan, A. Rusydi and Ariando, "Controlling Kondo-like scattering at the $SrTiO_3$-based interfaces" **Scientific Reports** 6, 25455 (2016).

6. H. J. H. Ma, J. Zhou, M. Yang, Y. Liu, S. W. Zeng, <u>W. X. Zhou</u>, L. C. Zhang, T. Venkatesan, Y. P. Feng and Ariando, "Anomalous anisotropic magnetoresistance in nonmagnetic perovskite oxide heterostructures" (submitted).

7. W. M. Lü, C. J. Li, Q. Li, J. X. Xiao, L. M. Zheng, X. Renshaw Wang, Z. Huang, S. W. Zeng, K. Han, <u>W. X. Zhou</u>, K. Y. Zeng, J. S. Chen, Ariando, T. Venkatesan and W. W. Cao, "Multi non-volatile state resistive switching arising from ferroelectricity and oxygen vacancy migration" (submitted).

8. K. Han, Z. Huang, S. W. Zeng, C. J. Li, <u>W. X. Zhou</u>, X. Renshaw Wang, T. Venkatesan and Ariando, "Uncovering Shubnikov-de Haas Oscillations at the $(La,Sr)(Al,Ta)O_3/SrTiO_3$ Interface" (submitted).

9. D-Y. Wan, B. X. Yan, J. Hong, W. S. Zeng, Z. Huang, C. J. Li, L. C. Zhang, K. Han, <u>W. X. Zhou</u>, Ariando, P. Yang, R. Xu, Q-H, Xu, T. Venkatesan, "Comparison of water splitting efficiencies of MNbO3 (M = Sr, Ca, Ba)" (Submitted).

LIST OF TABLES

LIST OF FIGURES

XV

XX

LIST OF SYMBOLS

B Magnetic field

M   Magnetization

K   Kelvin

e elementary charge

MR   Magnetoresistance

R Resistance

R_s Sheet resistance

R_H Hall resistance

ρ Resistivity

σ Conductivity

T Temperature

T_c Critical temperature or phase transition temperature

I Current

V Voltage

V_G Gate voltage

μ Mobility

n Carrier density

d lattice constant

uc   Unit cell

P_{O2} Oxygen partial pressure

PLD   Pulsed laser deposition

AFM   Atomic force microscopy

PFM   Piezoresponse force microscopy

TEM   Transmission electron microscopy

PPMS   Physical properties measurement system

SQUID   Superconducting quantum interference device

XRD   X-ray diffraction

Chapter 1 Introduction

1.1 Oxides: physics and applications

Silicon-based semiconductor electronics have improved our life quality dramatically over the past decades. The continuous improvement of the performance of the electronics has almost never failed our expectations as predicted by the famous Moore's law [1]. However, new challenges, such as quantum confinement and interference effect, emerge in the process of pursing smaller, faster and smarter electronics [2]. These challenges will inevitably lead to the failure of Moore's law. As a matter of fact, this is happening right in front of our eyes as the transistor size continues to scale down from 14 to 10 nm [3]. As also pointed out by many institutes and scientists, the Moore's law is dying in the next decade or so [3]. The question is: what can be done if the Moore's law is dying?

Many possible solutions to the above question have been proposed by researchers. Several examples are given below.

(1) New computers: Spintronics and Quantum computer. Unlike conventional computers, which manipulate charges, spintronics involve manipulation of spin degrees of freedom in solid-state systems [4]. On the other hand, unlike conventional computers, which have two definite states (0 or 1), quantum computers use quantum bits, which can be in superpositions of states [5]. By controlling coherent quantum mechanical waves, a quantum computer can dramatically improve our computational power for particular tasks [5]. Both spintronics and

quantum computer open up new possibilities for next generation computing and electronics.

(2) Complex structure design: from 2D to 3D. By designing more complex structures, more transistors can be integrated onto one chip and more functions can be realized. For example, the development of 3D printing technique may offer more precise and complex control over the device structure as compared to conventional lithography [6]. Another example is the Gate-all-around field effect transistor (GAAFET), which may provide a viable approach toward ultimate scaling of the Metal-oxide-semiconductor field effect transistor (MOSFET) [7].

(3) Artificial intelligence. The competition between AlphaGo and Lee Sedol in 2016 has clearly shown the power of artificial intelligence. By improving the software and algorithm, more intelligent electronics can be developed.

Apart from the above mentioned solutions, another solution is to replace conventional semiconductors with multi-functional materials, such as oxides, which host more versatile and exotic physical properties compared to conventional semiconductors [8, 9]. In this way, more functions could be realized in a limited size.

Oxides, especially complex oxides, are important not only for fundamental physics, but also for potential applications. The strong correlation and delicate balance between spin, orbit, charge and lattice in complex oxides provide a versatile playground to study condensed matter physics, such as electron-electron interaction, electron-phonon interaction, spin-orbit coupling [8, 10]. On the other hand, these correlations and interactions give rise to intriguing

and useful electronic, magnetic, thermal and optical properties, which could be used in future electronics. Some examples of the properties are: insulating (e.g. $SrTiO_3$, $LaAlO_3$), conducting (e.g. $SrRuO_3$), semiconducting (e.g. TiO_2), ferromagnetism (e.g. $SrRuO_3$, $La_{1-x}Sr_xMnO_3$), ferroelectricity (e.g. $BaTiO_3$, $PbTiO_3$), superconductivity (e.g. $YBa_2Cu_3O_{7-x}$), metal-insulator transition and various charge, spin and orbital orderings [8].

As to applications, many oxides have been commercially used. For example, Indium gallium zinc oxide (IGZO) based transparent field-effect transistors have been used for high-resolution displays by the technology giants-Apple and Sharp [11-12]. Lead zirconate titanate (PZT) based materials are used in ultrasound transducers, atomic force microscope actuators and piezoelectric sensors [13]. Barium strontium titanate (BST) has been used as dielectric materials in commercially available capacitors due to its large dielectric constant [14]. With the development of oxide technologies, more oxides are expected to find their applications in future electronics.

In view of both fundamental physics and potential applications, it is important to unveil the origin of these physical properties and control them with external stimuli. In this thesis, we study the origins of electronic and magnetic properties of oxide heterostructures and tune them with electric and ferroelectric field effect. Compared to other modulation techniques, electric and ferroelectric modulations are of particular interest as they do not cause any structural or chemical changes. Generally, this thesis consists of three projects: (1) Electron-soft phonon scattering in n-type $SrTiO_3$ (2) Coexistence of ferroelectricity and two-dimensional electron gas in $LaAlO_3/Ba_xSr_{1-}$

$_x$TiO$_3$/SrTiO$_3$ (001) heterostructure and (3) Ferroelectricity induced ferromagnetism in paramagnetic Pt thin films.

In Chapter 1, I introduce some general information and electric and ferroelectric control of electronic and magnetic properties in the field of complex oxides.

In Chapter 2, I discuss the experimental methods that were used in this thesis.

In Chapter 3, we show soft phonon induced electronic transport anomaly at the cubic-to-tetragonal phase transition temperature in n-type SrTiO$_3$, which is the "silicon" of oxide electronics. As far as we know, this electron-soft phonon scattering in SrTiO$_3$ is explicitly shown for the first time. These results shall provide some new insights into the conduction mechanism in n-type SrTiO$_3$.

In Chapter 4, we study ferroelectric control of the two-dimensional electron gas in a LaAlO$_3$/Ba$_x$Sr$_{1-x}$TiO$_3$/SrTiO$_3$ heterostructure. We find that the conductivity of the two-dimensional electron gas can be systematically controlled by varying the thickness of the ferroelectric Ba$_x$Sr$_{1-x}$TiO$_3$ layer. In addition, we show the coexistence of ferroelectricity and two-dimensional electron gas in this heterostructure by observing the interaction between the depolarization field of Ba$_x$Sr$_{1-x}$TiO$_3$ and the built-in electric field of LaAlO$_3$. Our approach provides an alternate route to control the two-dimensional electron gas with ferroelectricity. On the other hand, these results also provide evidence for the coexistence of two seemly incompatible properties (ferroelectricity and two-dimensional electron gas).

In Chapter 5, we study ferroelectric control of the magnetic properties of Pt thin films in a Pt/BaTiO$_3$/SrTiO$_3$ heterostructure. Ferromagnetism was found in Pt thin films by electric and magnetic measurements, as well as first-principles calculations. The unusual ferromagnetism was found to be induced by ferroelectric BaTiO$_3$. These results provide a new routine to tune an otherwise paramagnetic material into ferromagnetic with ferroelectricity.

In Chapter 6, we summarize the main results of Chapter 2-5 and discuss our future plans.

1.2 ABO$_3$ Perovskite oxides

Perovskite oxide is an important member of the oxide family. Many important oxides, such as SrTiO$_3$ (STO), BaTiO$_3$ (BTO), LaAlO$_3$ (LAO), SrRuO$_3$ (SRO), take the perovskite structure and can be described by a common chemical formula as ABO$_3$. The 'A' cation generally comes from Group 1 or Group 2 in the periodic table, i.e. the alkali and alkaline earth metals, for example potassium in KTaO$_3$, strontium in SrTiO$_3$. In some compounds, the 'A' cation may also come from rare earth metals, for example lanthanum in LaAlO$_3$. The 'B' cation generally comes from the transition metals, for example titanium in SrTiO$_3$ and ruthenium in SrRuO$_3$.

Figure 1.1 shows a typical sketch of the ABO$_3$ perovskite structure, where the 'A' cations sit at the corners of the cubic, the 'B' cation lies at the center of the cubic and the O^{2-} anions lie at the surface centers of the cubic. This ABO$_3$ unit cell (uc) can be further divided into two sublayers-AO and BO$_2$-along (001) direction, as shown in Fig. 1.1 (b). Here, m and n stand for the net charges for each layer, for example, in STO, the two sublayers are (SrO)^0 and (TiO$_2$)^0,

where the valences of Sr, Ti and O are +2, +4 and -2, respectively. We will see in later chapters that the net charge for each layer is very important for the electronic, magnetic and optical properties in some systems.
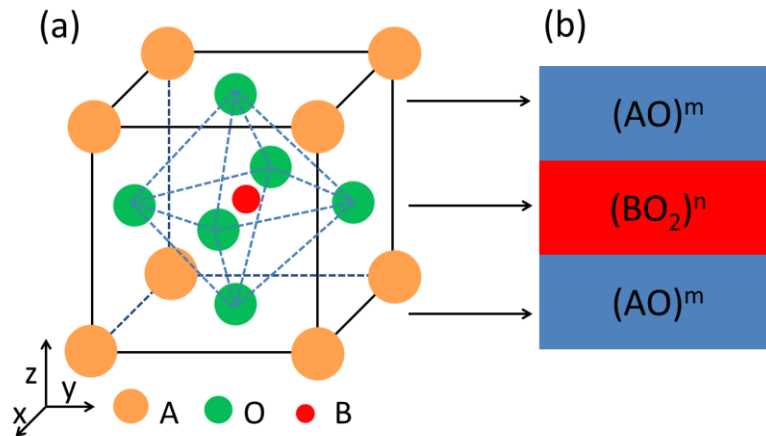
Figure 1.1 (a) Sketch of ABO_3 perovskite structure. (b) Sublayers-(AO) and (BO_2) for ABO_3 perovskite structure along (001) direction. Here, m and n represent net charge for AO and BO_2 layer, respectively.

The complex ABO_3 structure and various choices for the A and B cations give researchers a lot of possibilities to play with the physical (e.g. structure, symmetry) and chemical (e.g. different elements) properties of the perovskite oxides. In the next section, I will discuss in detail about the different properties for different perovskite oxides, which are studied in this thesis.

1.2.1 SrTiO₃-the silicon of oxide electronics

As silicon is the core for semiconductor-based industry, STO, a prototype perovskite oxide, is the key for oxide electronics. It is also one of the main focuses of this thesis. Here, I would introduce the structural, electrical, optical and magnetic properties of STO.

STO was first synthesized in the late 1940s. Early interests were evoked on its unusual and large dielectric response, its intriguing cubic-to-tetragonal phase

transition at T_c=105-110 K, the conduction mechanism in STO (when doped with electrons) and its absence of ferroelectricity.

In its bulk form, at room temperature, STO is a centrosymmetic paraelectric insulator with a band gap ~3.27 eV [15]. It undergoes a cubic-to-tetragonal second order antiferrodisplacive phase transition at T_c=105-110 K when the temperature is lowered [16]. Figure 1.2 (a) and (b) show the cubic and tetragonal structure of STO above and below T_c, respectively. In the cubic phase, the lattice constants a=b=c (a, b, c is lattice constant along x, y, z direction, respectively), and the TiO_6 octahedron lies at the center of the cubic. In the tetragonal phase, a=b<c, and the nearest TiO_6 octahedra rotate out-of-phase (clockwise and anti-clockwise) around the z axis.

Generally, a crystallographic phase transition can be described by a soft phonon mode whose eigenvectors approximate the ionic displacements occurring at T_c [16]. In addition, the energy of the soft phonon mode decreases in energy remarkably as T_c is approached [16]. In STO, the cubic-to-tetragonal phase transition is described by the zone corner phonon Γ_{25} (111) at T_c [16]. Figure 1.3 shows the temperature dependence of the energy of the soft phonon. It softens from high temperature to T_c and splits into two branches-A_{1g} (upper branch) and E_g (lower branch)-below T_c as the symmetry is lowered from cubic to tetragonal phase. This symmetry breaking doubles the unit cell from cubic to tetragonal phase and consequently the Brillouin zone corner Γ_{25} (111) phonon is folded onto the zone center of the tetragonal phase [16, 17].
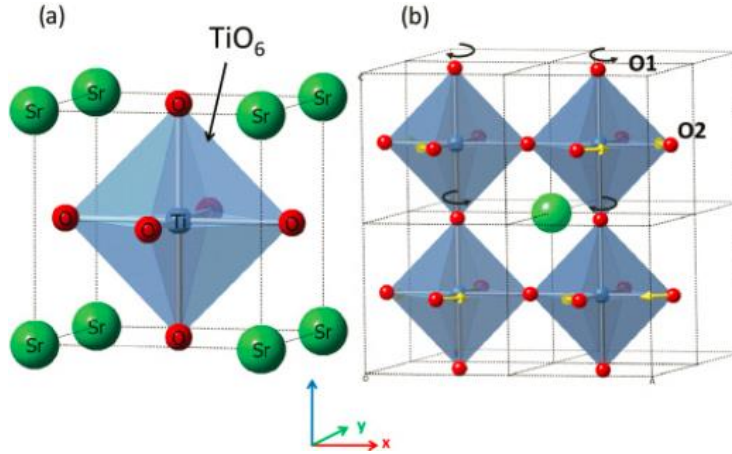
Figure 1.2 (a) and (b) Cubic and tetragonal structure for STO, respectively. O1 and O2 in (b) denote the nonrotating and rotating oxygen, respectively, adapted from [18].
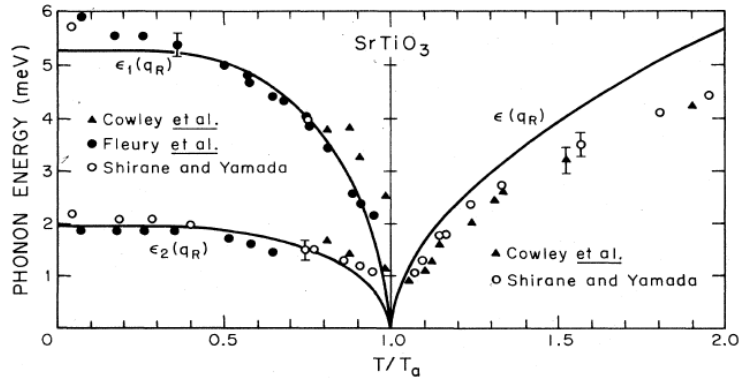
Figure 1.3 The energy of the soft phonon dependence on temperature. Here, temperature is normalized by the phase transition temperature T_a (or T_c), adapted from [16].

Although STO is a band insulator, itinerant electrons can be introduced into STO by chemical doping (Nb, La or Ta), high-vacuum annealing and argon milling [19-21]. In addition, it becomes superconducting below ~0.3 K and was the first oxide insulator discovered to be superconducting [22]. STO serves as a prototype to study the electron-electron, electron-phonon and phonon-phonon scattering in strongly correlated systems and the conduction mechanism has been controversial since the 1950s [19-27]. In the low temperature region (T<100 K), the conduction mechanism is generally explained by the Baber scattering, which considers both Coulomb interaction

and phonon-mediated electron-electron scatterings [20, 25-28]. The Baber scattering invokes a multi-band system with two different electron masses, and the momentum transfer between these two electron reservoirs give rise to the T^2 dependence of resistivity [27]. However, above 100K, the resistivity deviates from the Baber T^2 dependence [27]. In addition, the monotonic increase of mobility (μ) with decreasing temperature is either explained by the monotonic increase of dielectric constant (ε_r) and thus the transverse optical (TO) zone centre phonon scattering or the longitudinal optical (LO) phonon scattering [23, 29]. Nevertheless, attempts to quantitatively understand temperature dependent resistivity and mobility in STO in this region were unclear and controversial [20, 25-27].

In 2005, it was found that Ar^+-irradiated STO can emit blue light at room temperature when it is excited with a 325 nm He-Cd laser [21]. This finding provided possibilities to use STO in potential oxide-based optoelectronic devices [21]. In addition, this photoluminescence (PL) was found to be associated with the oxygen vacancies which were introduced during the Ar^+ irradiation. On one hand, the oxygen vacancies introduce itinerant electrons (two electrons per oxygen vacancy) in STO, on the other hand, they stabilize hole levels in self-trapped states [21]. The PL spectra can thus be used to study the oxygen vacancy concentration and the in-gap states in STO-based systems [30, 31]. It was found that PL spectra can give qualitative information about the oxygen vacancy concentration in STO-based systems, that is, higher oxygen vacancy concentration gives larger PL intensity [30, 31].

In its stoichiometric form, STO is diamagnetic [32]. However, experiments as well as first-principles have shown that ferromagnetism can be induced in STO [33-37]. The origin of the observed ferromagnetism is still controversial, several mechanisms have been proposed: oxygen vacancy, titanium vacancy or Ti^{3+} ions [33-37].

Apart from the rich exotic properties mentioned above, STO is also important for its compatibility with other oxides. Its cubic structure with an intermediate lattice constant (3.905 Å) makes it suitable to be used as a substrate to prepare oxide interfaces and heterostructures [38]. Moreover, chemical and thermal treatment method of STO substrate found in the 1990s has enabled sub-atomic control of its surface, making STO one of the state-of-art substrates [39, 40]. Some examples of such heterostructures are $LaAlO_3$/$SrTiO_3$, $BaTiO_3$/ $SrTiO_3$, $LaMnO_3$/ $SrTiO_3$. $LaAlO_3$/$SrTiO_3$ heterostructure will be discussed in detail in later   chapters.
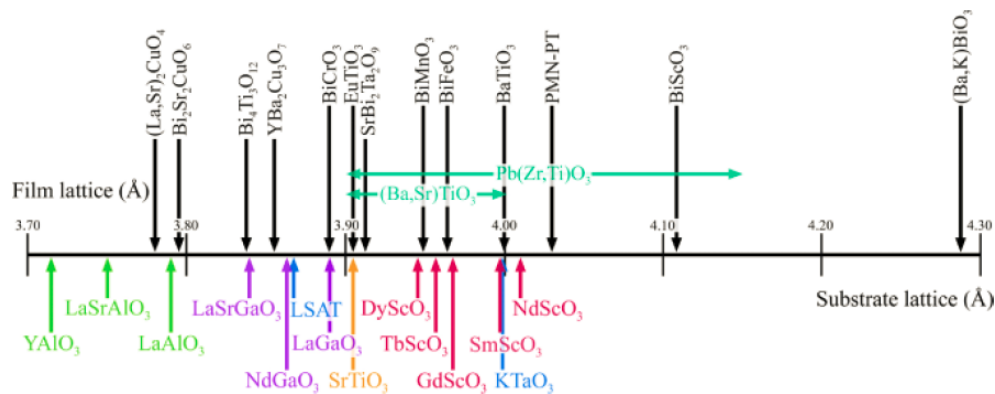
Figure 1.4 A number line showing the pseudocubic or pseudotetragonal in-plane lattice constants in angstroms for some perovskite oxides, adapted from [38].

1.2.2 BaTiO$_3$-a prototype ferroelectric

BaTiO$_3$ (BTO) is another important member of the perovskite oxide family and a prototype ferroelectric. In this section, I will discuss the physical nature, as well as the applications of ferroelectricity by using BTO as an example.

Ferroelectricity (FE) is a property of certain materials that have a spontaneous electric dipole moment even in the absence of an external electric field. The term ferroelectricity is used in analogy to ferromagnetism (FM). A ferromagnetic material has a long-range ordering of spins, while a ferroelectric material has a long-range ordering of electric dipoles. Similar to a ferromagnetic material, a ferroelectric material also has a Curie temperature (T_c). Below T_c, the material is ferroelectric and the center of positive charges of the material does not coincide with the center of negative charges, which gives rise to the spontaneous electric dipole moment. Above T_c, the material is paramagnetic and the spontaneous electric dipole moment disappears. The balance between the ferroelectric state and the paraelectric state is determined by two competing forces-the long-range Coulomb force (which favors the ferroelectric state) and the short-range repulsion (which favors the paraelectric state) [41-43]. Additionally, it was found by Cohen in 1992 that hybridization between titanium $3d$ states and oxygen $2p$ states is essential for the ferroelectricity of BTO [42].

There are generally two types of ferroelectrics, i.e. displacive and order-disorder. The perovskite oxide ferroelectrics, such as BTO, PbTiO$_3$ (PTO), are generally considered as the former type. Similar to the phase transition of STO discussed in last section, the displacive phase transition between the ferroelectric state and the paraelectric state can also be described by a soft

11

phonon mode. Here, I will discuss the soft phonon modes of BTO as an example.
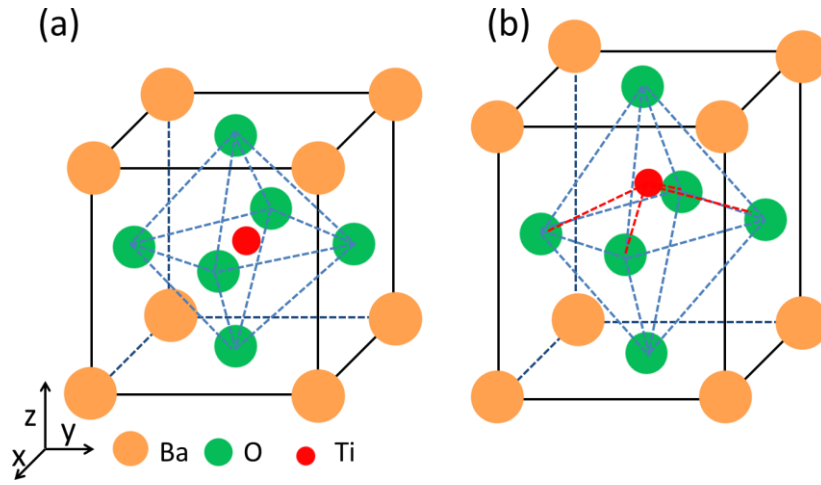
Figure 1.5 A schematic view of the cubic (a) and tetragonal (b) structure of BTO.

In its bulk form, BTO is an insulator with a bandgap of 3.2 eV [44]. It undergoes a series of phase transitions from high-temperature paraelectric cubic to ferroelectric tetragonal, orthorhombic and rhombohedral phases at 403, 287 and 197 K, respectively [45]. Figure 1.5 shows the cubic (a) and tetragonal structure (b) of BTO. In the cubic phase, the Ti ion sits at the center of the cubic unit cell, while in the tetragonal phase, the out-of-plane lattice constant is larger than the in-plane lattice constant and the Ti ion is displaced from the center of the oxygen octahedron along the [0 0 1] direction. While in the Ti ion is displaced along [0 1 1] and [1 1 1] direction for the orthorhombic and rhombohedral phase, respectively. These phase transitions are described by the evolution of the F_{1u} soft phonon mode, as shown in Fig. 1.6. From high temperature to low temperature, the triply-degenerate F_{1u} mode softens and splits into a non-degenerate A_1 mode and a doubly-degenerate E mode at the cubic-to-tetragonal phase transition temperature due to the symmetry breaking.

Upon further cooling, the doubly-degenerate E mode splits into two non-degenerate modes-B_1 and B_2 at the tetragonal-to-orthorhombic phase transition temperature. Finally, at the orthorhombic-to-rhombohedral phase transition temperature, the B_2 mode transforms into the E mode [46]. At each phase transition, one non-degenerate component stabilizes abruptly while the other components continue to soften on cooling [46].
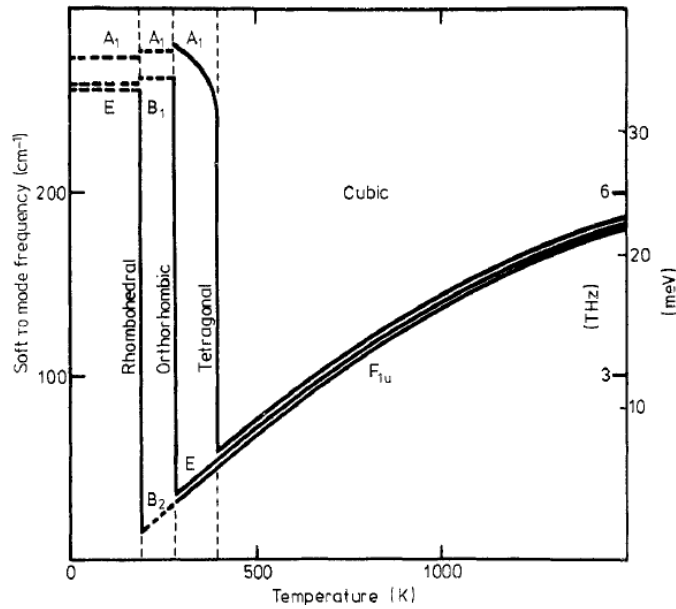
Figure 1.6 A schematic plot of the evolution of the temperature dependent F_{1u} soft phonon, adapted from [46].

The soft phonon description of the phase transitions of BTO has proven its usefulness in explaining the physical properties of BTO, for example, the dielectric constant. In the Lyddane –Sachs-Teller (LST) relation:

$$\frac{\varepsilon(0)}{\varepsilon(\infty)} = \prod_{j}^{N} \frac{\omega_{LOj}^2}{\omega_{TOj}^2}$$

13

where $\varepsilon(0)$ and $\varepsilon(\infty)$ is the static and high-frequency dielectric constant, respectively, ω_{LO} and ω_{TO} is the eigenfrequency of the longitudinal and transverse optical mode, respectively. It is generally found that the optical modes with higher frequencies exhibit no sizeable temperature dependence. And $\varepsilon(0)$ is directly related to the frequency of the lowest soft phonon modes [47]. Figure 1.7 shows the temperature dependence of the dielectric constant of BTO. One can clearly see that $\varepsilon(0)$ inversely relates to the frequency of the soft phonon modes of BTO in Fig. 1.6.
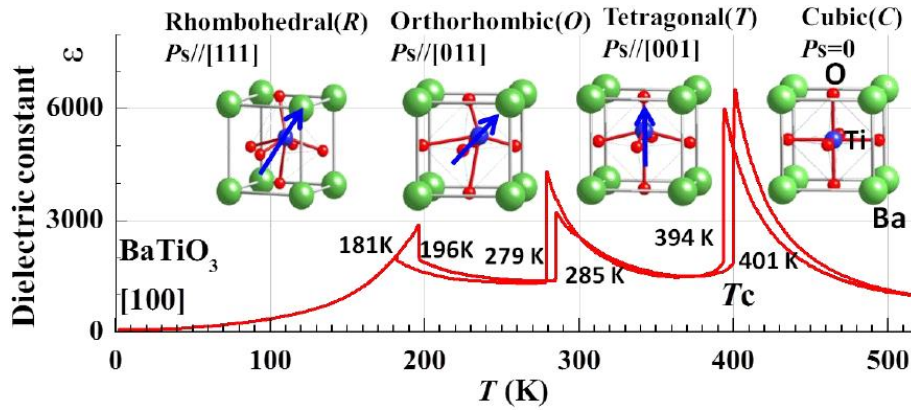
Figure 1.7 Temperature dependent dielectric constant of BTO single crystal along [100] direction. The relative displacement of Ti in the oxygen octahedron and the corresponding spontaneous polarization is also shown in each phase, adapted from [48].

Despite the success of the soft phonon theory in the displacive ferroelectrics, it has been proposed that BTO has both displacive and order-disorder components [49-51]. In the purely order-disorder phase transition picture, the Ti ion is at all temperatures above T_c located at one of the eight positions shifted from the center along the body diagonals of the unit cell, i.e. in every single unit cell, the polarization is pointing along one of the eight <1 1 1> directions [49-51]. Only the rhombohedral phase is completely ordered, that is, all the polarizations are directed along the same [1 1 1] direction. And all the

14

other high-symmetry phases are disordered [49-51]. The numbers of the allowed directions along which the Ti ion is displaced are 1, 2, 4 and 8 for the rhombohedral, orthorhombic, tetragonal and cubic phase, respectively [49-51]. These allowed directions then determine the macroscopic spontaneous polarization direction to be along [1 1 1], [0 1 1] and [0 0 1] for the rhombohedral, orthorhombic and tetragonal phase, respectively. The cubic phase is paraelectric without a polarization. [49-51].

Although the microscopic mechanism for the ferroelectricity of BTO is still under debate between the displacive and order-disorder model, macroscopically, the spontaneous polarization direction is conclusive, that is, [1 1 1], [0 1 1] and [0 0 1] for the rhombohedral, orthorhombic and tetragonal phase, respectively, as shown in Fig. 1.7.

1.3 Oxide thin films, heterostructures and interfaces

With the development of oxide thin film growth techniques, such as molecular beam epitaxy (MBE) and pulsed laser deposition (PLD), high quality heterostructures can now be prepared with atomically sharp interfaces. Compared to the bulk materials, oxide thin films, heterostructures and interfaces show even more abundant and unexpected properties due to the symmetry breaking at the surfaces/interfaces, reduced dimension, strain and defects *etc*.

In the case of thin films, one well-known example is the observation of room-temperature ferroelectricity in strained and even strain-free STO thin films of a few nanometers, despite the fact that bulk STO is paraelectric [52-54]. Another example is the large enhancement of the ferroelectricity in strained

BTO thin films, whose Curie temperature and polarization can be dramatically enhanced compared to its bulk counterpart [55, 56].

In the case of heterostructures and interfaces, some prominent examples are: (1) The observation of a high-mobility two-dimensional electron gas (2DEG) at the interface of $LaAlO_3/SrTiO_3$ (LAO/STO), although both LAO and STO are band insulators [57].

(2) The observation of the antiferromagnetic-to-ferromagnetic phase transition of $LaMnO_3$ (LMO) thin film deposited on a STO (001) substrate when LMO thickness exceeds 6 unit cells [58].

(3) The observation of ferromagnetism in $LaMnO_3/SrMnO_3$ superlattice, although both $LaMnO_3$ and $SrMnO_3$ are non-magnetic [59].

As most of my research is related to the LAO/STO interface, I will introduce the properties and possible origins of the 2DEG at this interface in detail.

1.3.1 $LaAlO_3/SrTiO_3$ interface-properties

As discussed in section 1.2.1, STO is a band insulator with a band gap of ~3.27 eV [15]. LAO is also a band insulator with a band gap of ~5.6 eV [57]. $SrTiO_3$ has a cubic structure at room temperature with a lattice constant of 3.905 Å, while LAO maintains a rhombohedral phase at room temperature and transforms into a cubic phase at temperatures above 875 K [60, 61]. For simplicity, the rhombohedral phase of LAO is often treated as a pseudocubic structure with a lattice constant of 3.868 Å [62]. Structurally, as shown in Fig. 1.1, one unit cell of STO can be divided into two charge-neutral sublayers-

$(TiO_2)^0$ and $(SrO)^0$, while LAO has alternating negatively charged $(AlO_2)^{-1}$ and positively charged $(LaO)^+$ layers.

In 2004, Ohotomo and Hwang first reported a high-mobility two-dimensional electron gas (2DEG) at the *n*-type interface of LaAlO$_3$/SrTiO$_3$ (LAO/STO), which has an atomic layer stacking sequence of AlO$_2$-LaO-TiO$_2$-SrO at the interface [57]. However, the p-type interface with an atomic layer stacking sequence of LaO-AlO$_2$-SrO-TiO$_2$ is insulating [57]. Figure 1.8 shows the sheet resistance, Hall coefficient and Hall mobility of *n*-type 60 Å LAO/STO samples prepared with different oxygen partial pressures. One can see that all the samples show metallic behavior and the samples prepared with 10^{-6} torr oxygen partial pressure show mobility as high as 10,000 cm^2 V^{-1} s^{-1} at low temperature [57]. Since then, it has drawn intense attentions as new properties continue to emerge at this interface.
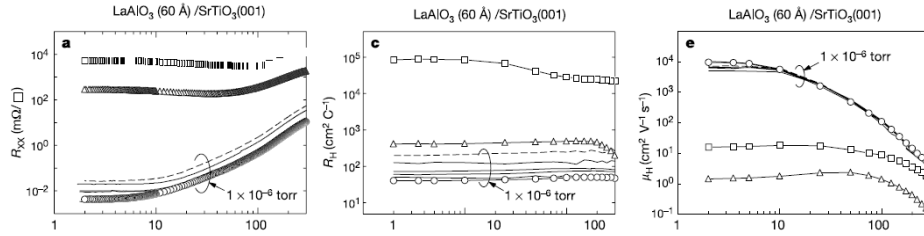
Figure 1.8 Electronic transport properties of the two-dimensional electron gas at the n-type LAO/STO interface. Temperature dependence of sheet resistance (a), Hall coefficient (c) and Hall mobility (e) for 60 Å LAO/STO samples prepared with different oxygen partial pressures, adapted from [57].

In 2006, it was found that LAO has to be thicker than 4 uc for the LAO/STO interface to be conducting. Fig. 1.9 (a) and (b) show LAO thickness dependence of sheet conductance and sheet carrier density of the 2DEG, respectively. Below 4 uc of LAO, the interface has a sheet conductance of 10^{-9} Ω^{-1}, while beyond 4 uc of LAO, the sheet conductance increases by 4 orders

of magnitude to around 10^{-5} Ω^{-1}. Similarly, the sheet carrier density is negligibly small below 4 uc of LAO and increases to around 2×10^{13} cm^{-2} beyond 4 uc of LAO. These results indicate an insulator-metal transition from 3 to 4 uc of LAO [63].
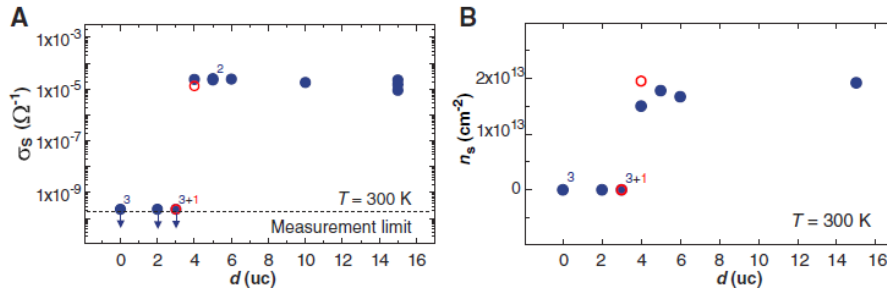
Figure 1.9 LAO thickness dependence of sheet conductance (a) and sheet carrier density (b) of the 2DEG at LAO/STO interface at room temperature, adapted from [63].

In 2007, Reyren *et al.* found that the 2DEG at LAO/STO interface becomes superconducting below a critical temperature ~200 mK and that the superconducting layer is confined to 10 nm within STO at the LAO/STO interface [64]. As shown in Fig. 1.10, a clear metal-superconductor transition can be observed for 8 uc LAO/STO and 15 uc LAO/STO at a critical temperature of 200 and 100 mK, respectively.
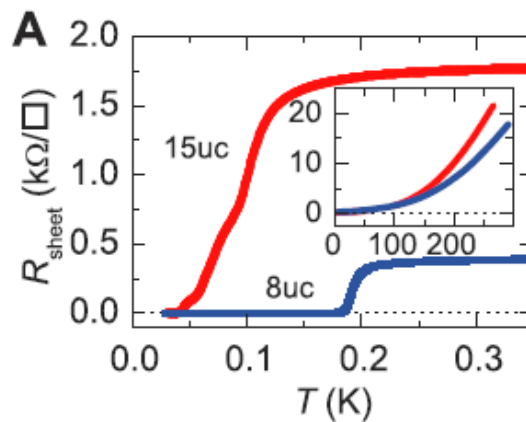
Figure 1.10 Temperature dependent sheet resistance for 8 uc LAO/STO and 15 uc LAO/STO, adapted from [64].

18

Also in 2007, Brinkman *et al.* discovered magnetic properties at the LAO/STO interface, although both LAO and STO are non-magnetic [65]. As shown in Fig. 1.11 (left), the samples grown beyond an oxygen partial pressure of 10^{-4} mbar show an upturn at low temperature, a signature of the Kondo effect, which describes the scattering of itinerant electrons by localized magnetic moments. Figure 1.11 (right) shows a clear hysteresis loop of the magnetoresistance of a LAO/STO sample grown at 10^{-3} mbar [65].
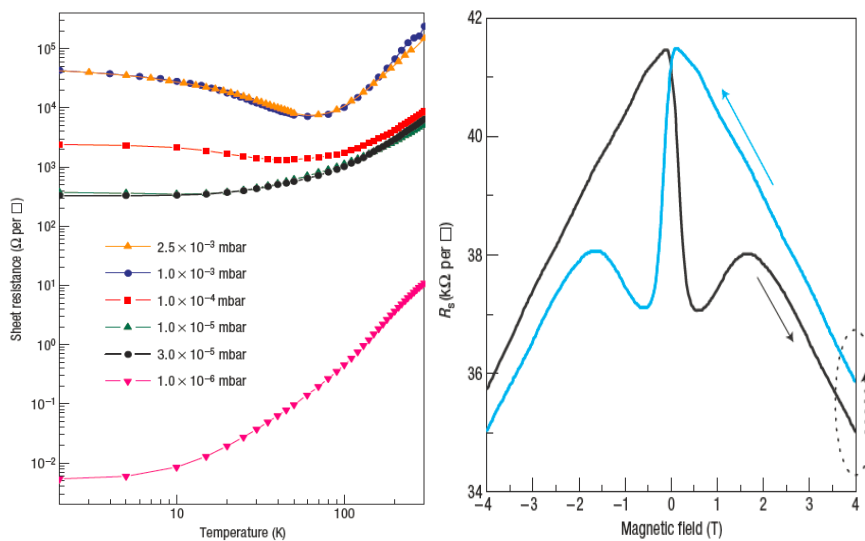
Figure 1.11 Magnetic properties at LAO/STO interface. (left) Temperature dependent sheet resistance for LAO/STO samples prepared at different oxygen partial pressures. (right) Magnetic field dependent sheet resistance at 0.3K of a conducting LAO/STO sample grown at 10^{-3} mbar, adapted from [65].

Later, several groups reported the coexistence of superconductivity and ferromagnetism at LAO/STO interface, which makes this interface even more interesting [66-69]. Ferromagnetism and superconductivity are generally considered as two incompatible properties as ferromagnetism destroys the Cooper pairs, which are responsible for superconductivity. Figure 1.12 shows the direct mapping of the coexistence of ferromagnetism and superconductivity at LAO/STO interface by scanning superconducting

quantum interference device (SQUID). Figure 1.12 (a) shows the magnetic patches in a uniform paramagnetic background, while weak diamagnetic superconducting susceptibility can be observed in Fig. 1.12 (b). These results indicate the nanoscale phase separation of superconductivity and ferromagnetism.
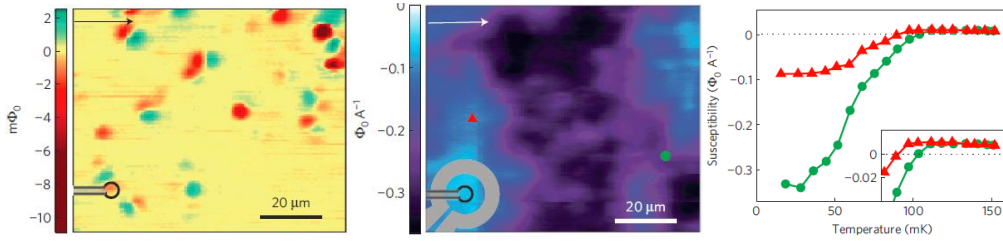
Figure 1.12 Coexistence of ferromagnetism and superconductivity at LAO/STO interface. (left) Scanning SQUID mapping of the magnetic order at LAO/STO interface. (middle) Susceptometry mapping of the superfluid density at 40 mK. (right) Temperature dependent susceptibility taken at the two spots in the middle image. Adapted from [67].

Apart from the above mentioned properties, some other interesting properties, such as 2D quantum oscillations [70, 71], Rashba spin-orbit interaction [72, 73], have also been observed at LAO/STO interface.

1.3.2 LaAlO$_3$/SrTiO$_3$ interface-origins

To explain the observed 2DEG at LAO/STO interface, several possible mechanisms have been proposed. Each of them can explain certain experimental results and the exact origin is still under debate. In this section, I will introduce these mechanisms.

(1) The most popular model so far is the polar catastrophe model. As shown in Fig. 1.13 (a), the polar discontinuity at the *n*-type interface (with a sequence of AlO$_2$-LaO-TiO$_2$-SrO) would result in a diverging potential with LAO thickness. To avoid this potential divergence, 0.5

e$^-$ per unit cell is transferred from the surface of LAO to the interface of LAO/STO. This process reconciles the potential divergence as shown in Fig. 1.13 (c). As a result, the Ti^{4+} ion at the interface becomes Ti$^{3.5+}$, which can be treated as a mixture of Ti^{4+} and Ti^{3+}. Meanwhile, the transferred electrons serve as the source for the 2DEG [74].

Similarly, from a simple ionic picture, the polar discontinuity also exists at the *p*-type interface (with a sequence of LaO-AlO$_2$-SrO-TiO$_2$). One would expect 0.5 hole per unit cell to be transferred from the surface of LAO to the interface of LAO/STO, as shown in Fig. 1.13 (b) and (d). However, in this case, no mixed valence is available to host the 0.5 hole. Thus, an atomic reconstruction is required [74].

This model successfully explained the 4 uc critical thickness of LAO for the metal-insulator transition [63] and the insulating behavior for the *p*-type interface [57]. However, challenges to this model were posed by several experimental observations. The first one is the far less experimentally observed carrier density (2-3×10^{13} cm^{-2}) as compared to that (3.4×10^{14} cm^{-2}) predicted by the polar catastrophe model [75]. Another challenge is the observation of the absence of built-in electric field in LAO as measured by X-ray photoemission [76].
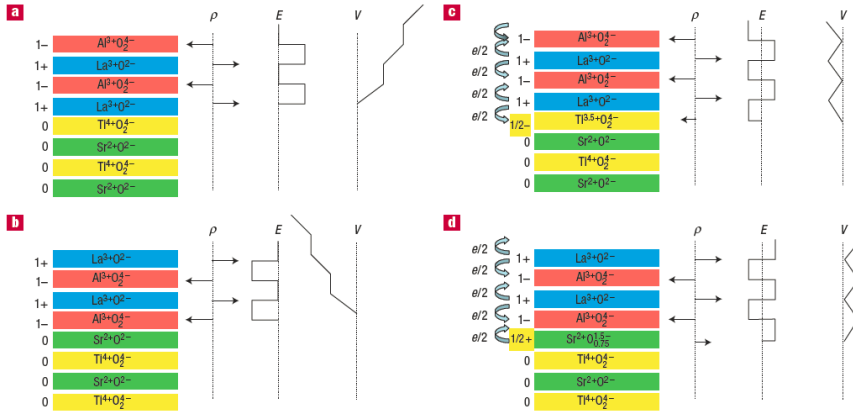
Figure 1.13 The polar catastrophe model at LAO/STO interface. The distribution of charge, electric field and potential for unreconstructed (a) and reconstructed (c) *n*-type LAO/STO (001), respectively. (b) and (d) shows the analogous unreconstructed and reconstructed interface for *p*-type LAO/STO (001), respectively. Adapted from [74].

(2) Oxygen vacancy formation in STO. Almost all the LAO/STO interfaces in the literature are grown in vacuum at elevated temperature (typically around 700 ℃), this sample preparation process may introduce oxygen vacancies in STO. In addition, the bombardment of LAO may also contribute to the formation of oxygen vacancies, especially when the samples are prepared by PLD. Each oxygen vacancy may contribute two itinerant electrons [30]. This mechanism is supported by the observation of a 2DEG at the interface of amorphous LAO and STO. However, the persistence of conductivity after eliminating oxygen vacancies with oxygen annealing in crystalline LAO/STO samples indicates that oxygen vacancy is not essential for the observation of 2DEG [30].

(3) Cation interdifussion at the interface. The high-temperature and high-energy preparation condition for LAO/STO interface could result in intermixing of La and Sr or Al and Ti at the interface. As introduced in

section 1.2.1, La doped STO is conducting, which may explain the origin of the 2DEG. This mechanism is supported by the surface X-ray diffraction measurements [77]. However, this mechanism can not explain the insulating behavior of the *p*-type LAO/STO interface, where the cationic intermixing is also expected [57]. More importantly, high resolution TEM experiments showed very sharp interface with little intermixing [74].

(4) Polarity-induced defects [75]. It is proposed that the polar discontinuity at the LAO/STO interface spontaneously induces oxygen vacancies at LAO surface and Ti-on-Al antisite defects at the interface. And the surface oxygen vacancy is responsible for the observed 2DEG at the interface, while the Ti-on-Al antisite defect is responsible for the observed interfacial ferromagnetism. This mechanism is the most recent proposed mechanism and the authors claimed that it is the most comprehensive mechanism. However, more experimental results are needed to verify this mechanism.

In summary of the four mechanisms, each of them can explain certain experimental results while each of them also has certain drawbacks. It should be noted that several mechanisms may coexist in the experimental samples. For example, the conductivity of the as-grown crystalline LAO/STO (001) samples normally has contributions from both oxygen vacancies and polar catastrophe [30].

1.4 Electric and ferroelectric control of electronic properties

It's well known that the physical properties of a material can be modulated by an external electric field. The most famous example is the metal-oxide-

semiconductor field effect transistor (MOSFET). Figure 1.14 shows a schematic of a typical MOSFET, which is composed of a channel and four terminals-drain, source, gate and body. When an external electric field is applied between the gate and body, the insulating oxide dielectric layer becomes polarized and it can attract or repel electrons in the channel. As a result, an electron accumulation or depletion layer is formed in the channel, which correspond to a low-resistance (large source-drain current) and a high-resistance state (small source-drain current), respectively.

In addition to MOSFET, electric field effect can also be used to control the physical properties of oxide thin films, heterostructures and interfaces. As an example, the electric field effect modulation of LAO/STO interface is introduced below.
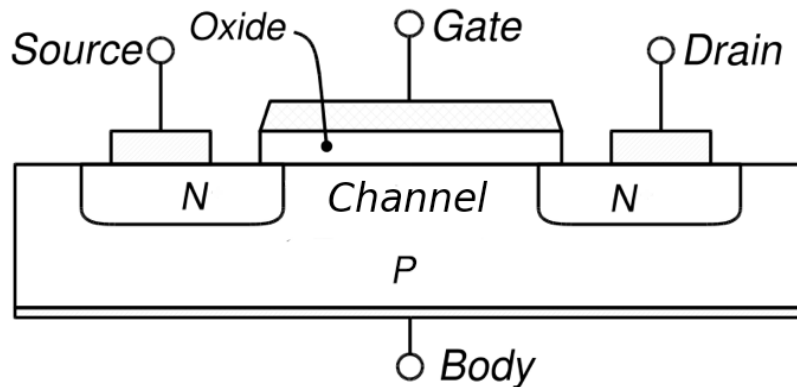
Figure 1.14 A schematic diagram of a typical MOSFET, adapted from [78]

1.4.1 Electric field modulation of LaAlO₃/SrTiO₃ interface

In the literature, there are basically three configurations for electric field modulation, i.e. back gating, top gating and ionic liquid gating, of LAO/STO interface.

In 2006, Thiel *et al.* first observed an insulator-metal transition for a 3 uc LAO/STO insulating sample by applying a gate voltage on STO, as shown in Fig. 1.15. In this back-gating configuration, STO was used as the dielectric. By reversibly change the gate voltage, the sheet resistance can be switched between a high-resistance state and a low-resistance state, which is analogous to a MOSFET [63]. The gate voltage applied on STO modulates both carrier density and carrier mobility, with the latter taking the dominant role [79]. Later, it was reported by Caviglia *et al.* that a quantum phase transition between an insulating state and a superconducting state could be reversibly controlled with a gate voltage [80]. In addition, several groups reported that the superconducting transition temperature T_c of the LAO/STO interface could also be modulated with a gate voltage [71, 73, 79]. Furthermore, it was found that the spin-orbit coupling energy [72, 73] and the Shubnikov-de Haas (SdH) oscillations [70, 71] were also gate voltage dependent.
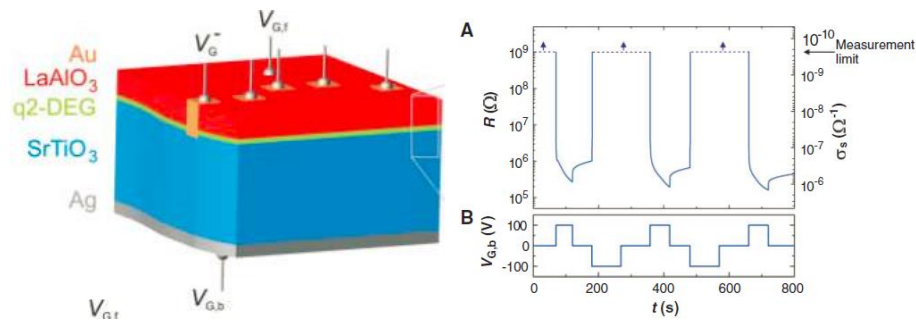
Figure 1.15 (left) The back gating configuration for LAO/STO interface. A gate voltage was applied between V_G^- and $V_{G,b}$. (right) Sheet resistance (top) and gate voltage (bottom) dependence on time at 300K for a 3 uc LAO/STO sample. Adapted from [63].

In the top-gating configuration, a gate voltage is applied on LAO, i.e. LAO serves as the dielectric. As shown in Fig. 1.16, the drain-source current, and, thus the resistance of the 2DEG at LAO/STO interface, can be modulated by sweeping the gate voltage applied on LAO [81]. As compared to the back-

gating configuration, this configuration normally requires much smaller gate voltage. By using the tip of a conducting atomic force microscope (CAFM) as the top electrode, Jeremy Levy and coworkers have exploited reversible nanoscale (~2 nm) control of the conductivity of a 3 uc LAO/STO sample [82-84]. Furthermore, LAO/STO-based single electron transistor has been realized by using this atomic force microscope lithography technique [84].
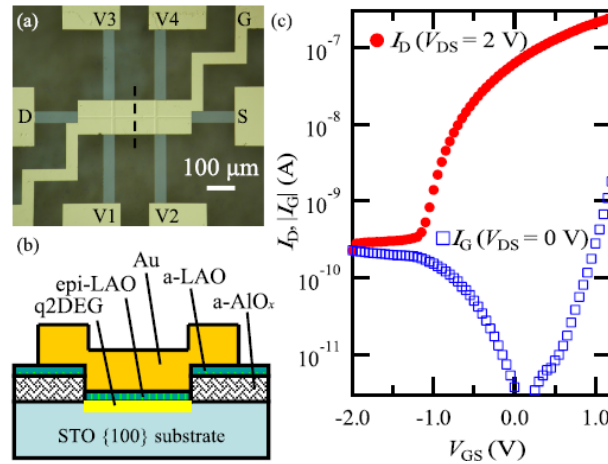
Figure 1.16 (a) and (b), top and side view of the back-gating configuration of LAO/STO interface. (c) Gate voltage dependent drain-source current (I_D) and leakage current (I_G) with fixed drain-source voltage (V_{DS} = 2V). Adapted from [81].

In the liquid gating configuration, a gate voltage is applied on the ionic liquid, as shown in Fig. 1.17. Similar to back gating and top gating configuration, the carrier density and mobility of the 2DEG at LAO/STO interface can also be modulated. The advantage of this technique lies in its strong capability of accumulating and depleting electrons (~10^{15} cm^{-2}) [85, 86]. Large enhancement of carrier mobility of the 2DEG at LAO/STO interface has been realized by strong depletion of the carrier density [85].
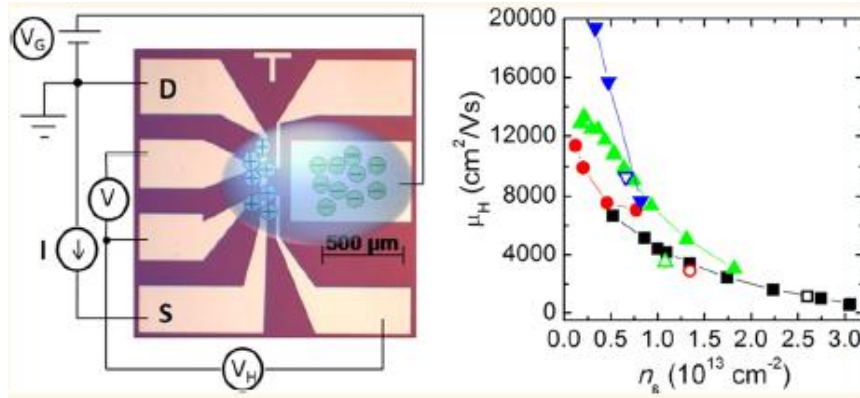
Figure 1.17 (left) Top view of the Hall bar structure of a LAO/STO sample. The ionic liquid covers the transparent bluish area. (right) Mobility dependence on carrier density as a result of ionic liquid gating. Adapted from [85].

1.4.2 Ferroelectric modulation of LaAlO$_3$/SrTiO$_3$ interface

As discussed above, electric field modulation has been efficient and fruitful in controlling the physical properties of the 2DEG at LAO/STO interface. However, the switched state will gradually revert back to its original state after removing the electric field [79, 87]. For practical applications, it is important to tune the 2DEG in a reversible and non-volatile manner. This can be realized by integrating ferroelectricity in LAO/STO heterostructure. In the literature, there are basically four configurations for ferroelectric modulation of LAO/STO interface.

The first configuration is ferroelectric top gating, as shown in Fig. 1.18 [88-90]. A ferroelectric Pb(Zr$_{0.2}$Ti$_{0.8}$)O$_3$ (PZT) layer is deposited on LAO/STO. By applying a gate voltage on PZT, the polarization direction of PZT can be reversibly switched between a downward and an upward state. The different polarization directions of PZT generate different electric fields in LAO/STO, and, thus, the conductance of the 2DEG is modulated. The switched "on" and "off" state can be preserved even after removing the external electric field, as

27

shown in Fig. 1.18 (c). In addition, similar effect has also been reported by replacing PZT with BiFeO$_3$ [90].
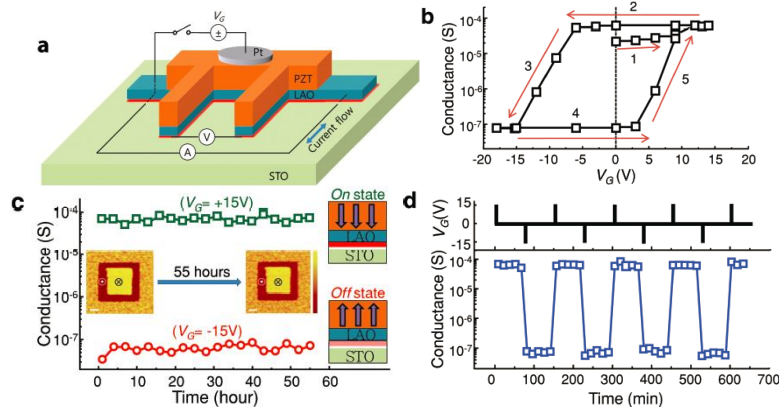
Figure 1.18 Ferroelectric top gating control of the 2DEG at LAO/STO interface. (a) Schematic diagram of the structure of a Pt/PZT/LAO/STO sample with a Hall bar. (b) Gate voltage dependent conductance of the 2DEG. (c) Time dependent conductance of the 2DEG switched with a positvie (green line) and negative voltage (red line). The external gate voltage was turned off at time t = 0. (d) Reversible switch of the conductance with alternating positive and negative voltage pulses. Adapted from [88].

Another configuration has a ferroelectric/STO structure, where a polar ferroelectric layer is deposited on STO substrate. As shown in Fig. 1.19, at the KNbO$_3$/STO interface, the same polar discontinuity as that of LAO/STO interface is also present. This polar discontinuity is expected to generate a 2DEG at KNbO$_3$/STO interface. As KNbO$_3$ is ferroelectric, modulation of the conductivity of the 2DEG can be realized by switching the polarization direction of KNbO$_3$. As shown in Fig. 1.19 (c), the calculated density of states (DOS) shows a high-resistance and low-resistance state corresponding to different polarization directions of KNbO$_3$ [91]. Apart from KNbO$_3$, several other ferroelectrics have also been proposed to generate 2DEG at the ferroelectric/STO interface, such as BiFeO$_3$ (BFO) [92] and BTO [93].
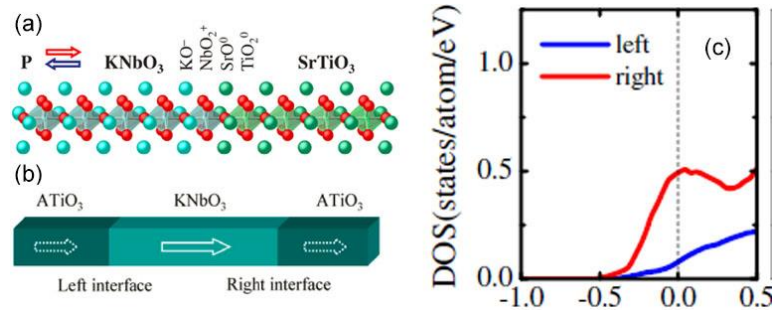
Figure 1.19 Ferroelectric control of the 2DEG at $KNbO_3$/STO interface. (a) Atomic structure of $KNbO_3$/STO interface showing polar discontinuity at $KNbO_3$/STO interface. (b) Schematic illustration of the STO/$KNbO_3$/STO unit cell used in [91] with the polarization direction indicated by the arrow. (c) DOS at the two interfaces in (b).

The other two configurations are: LAO/ferroelectric substrate and LAO/STO/ferroelectric substrate as shown in Fig. 1.20. In the LAO/ferroelectric configuration, if a 2DEG is present at LAO/ferroelectric interface, its conductivity is expected to be modulated by switching the polarization direction of the ferroelectric substrate. Theoretically, a switchable 2DEG has been predicted at LAO/BTO interface [94]. In the LAO/STO/ferroelectric configuration, the 2DEG at LAO/STO interface can be modulated by switching the polarization direction of the ferroelectric substrate. A LAO/STO/BTO structure has been theoretically proposed [95].
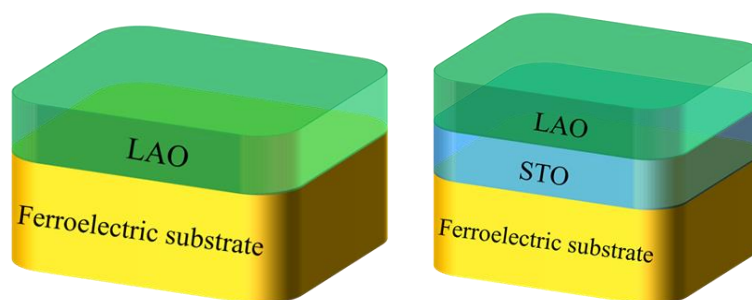
Figure 1.20 Ferroelectric control of the 2DEG at LAO/ferroelectric interface (left) and (right) LAO/STO interface (right) by switching the ferroelectric substrate.

It should be noted that, for the four configurations discussed in this section, only the first configuration has been experimentally realized. All the others are theoretical predictions, which haven't been realized in experiments to the best of my knowledge.

Apart from electric and ferroelectric modulations, other techniques, such as light illumination [96], strain [97], capping layer [98] and surface polar adsorbates [99], have also been successfully applied to tune the conductivity of the 2DEG at LAO/STO interface.

1.5 Electric and ferroelectric control of magnetic properties

Not only can electric field effect modulate electronic properties of a material as discussed in section 1.4, it can also control magnetic properties through magnetoelectric coupling. Electric control of ferromagnetism has triggered intense researches in recent years due to its fundamental and technological importance, especially in view of recent developments in magnetoelectronics and spintronics [100, 101]. The drawback of large power assumption due to magnetic writing in current electronics can be overcome by electric field control of magnetism, which relies on zero-current, gate-controlled operations [102].

The early interests of electric field control of magnetism lied in semiconductors. One prominent example is the control of Curie temperature of magnetic semiconductor (In,Mn)As thin film [100] by modulating the carrier concentration with an external electric field. Another example is the control of magnetic anisotropy of magnetic semiconductor (Ga,Mn)As thin film [103].

Later, electric field control of magnetism was extended into ferromagnetic metal and complex oxides. For example, electric field control of coercive field, magnetic anisotropy and Curie temperature in ferromagnetic metal thin films [104, 105]. For complex oxides, electric field control of Curie temperature and magnetic phase transition has been demonstrated in manganites [106, 107].

Non-volatile control of ferromagnetism has been realized by switching the polarization of the ferroelectrics in epitaxial ferroelectric/ferromagnet heterostructures. As an example, I introduce the ferroelectric control of the magnetic properties of FeRh thin film on a ferroelectric BTO substrate, as reported in Ref. [108].

FeRh exhibits an antiferromagnetic-to-ferromagnetic phase transition at T^*=350 K. As can be seen in the top panel of Fig. 1.21 (b), the magnetization increases from around 50 e.m.u.cm^{-3} at 350 K to nearly 800 e.m.u.cm^{-3} at 400 K, indicating the antiferromagnetic-to-ferromagnetic phase transition under zero gate voltage. When a positive voltage (V_g = 21 V) is applied (which corresponds to a BTO polarization pointing away from FeRh), the T^* is shifted to 375 K, which is 25 K higher than the original state (second panel in Fig. 1.21 (b)). Furthermore, the original state can be restored after removing the gate voltage (third panel in Fig. 1.21 (b)). When a negative gate voltage (V_g= -21 V) is applied (which corresponds to a BTO polarization pointing towards FeRh), the T^* is again shifted to higher temperature, although smaller than that at 375 K (fourth panel in Fig. 1.21 (b)). Figure 1.21 (c) shows the difference between the gated and original states, which clearly shows the large magnetization change with an external electric field. It was found that two

mechanisms contribute to this large magnetoelectric coupling at FeRh/BTO interface: (1) Voltage induced strain. (2) Electrostatic effect.
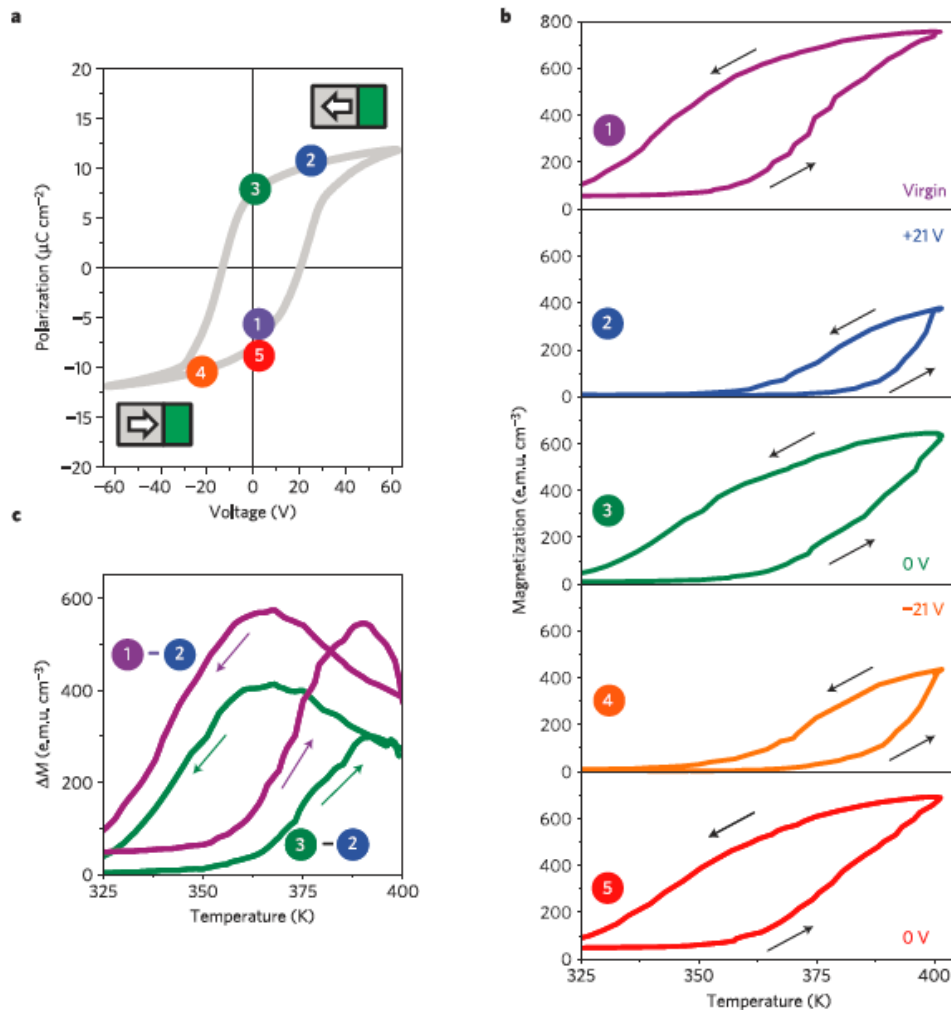
Figure 1.21 Ferroelectric modulation of magnetization in a FeRh/BTO (001) heterostructure. (a) BTO polarization dependence on gate voltage. The green and gray rectangle stands for FeRh and BTO, respectively. The arrows represent polarization direction of BTO. (b) FeRh magnetization dependence on temperature for different gate voltages. (c) Magnetization difference between different curves in (b). Adapted from [108].

Some other prominent examples are: (1) Electric field control of magnetic properties of ferromagnetic $La_{0.67}Sr_{0.33}MnO_3$ thin films on ferroelectric BTO substrate [109]. (2) Electric field control of local ferromagnetism by using the multiferroelectric $BiFeO_3$ [110]. (3) Electric field control of magnetic properties in $Pb(Zr_{0.2}Ti_{0.8})O_3/La_{0.8}Sr_{0.2}MnO_3$ heterostructure [111].

One important application of electric field control of ferromagnetism is multiferroic tunnel junction (MFTJ), which can be considered as a combination of magnetic tunnel junction (MTJ) and ferroelectric tunnel junction (FTJ).

As shown in Fig. 1.22, a MTJ has a FM/I/FM structure, i.e. two ferromagnetic metal (FM) electrodes sandwiching a thin insulator (I) layer. In a MTJ, electrons can travel from one FM electrode to the other FM electrode by tunneling through the thin insulator layer. The tunneling probability or the tunneling current is spin-dependent (or magnetization-dependent). There are two configurations for the magnetization of the two FM electrodes: (1) Parallel, the tunneling current is large and the corresponding tunneling magnetoresistance (TMR) is small. (2) Anti-parallel, the tunneling current is small and the corresponding TMR is large. The difference in TMR in these two configurations is due to the disproportion of the number of electrons parallel and anti-parallel to the magnetization direction of a FM [112]. As a result of the two different configurations, two resistance states can be obtained as shown in the lower panel of Fig. 1.22.

On the other hand, FTJ has a NM/FE/NM structure, i.e. two normal metal (NM) electrodes sandwiching a thin ferroelectric (FE) insulator layer. Similar to MTJ, electrons can travel from one electrode to the other by tunneling through the FE layer. In a FTJ, the tunneling current is polarization-dependent. The two configurations for the electric polarization of the ferroelectric layer are: (1) Pointing-up, the tunneling current is large and the corresponding tunneling electroresitance (TER) is small. (2) Pointing-down, the tunneling current is small and the corresponding TER is large. Several mechanisms have

been proposed to explain the polarization-dependent TER: (a) the electrostatic potential across the junction (b) interface bonding strength and (c) strain associated with the piezoelectric response [112].

By replacing the insulator layer of a MTJ with a ferroelectric layer (or equivalently, by replacing the NM electrodes with FM electrodes in a FTJ), a MFTJ can be constructed, which has a FM/FE/FM structure, i.e. two ferromagnetic metal electrodes sandwiching a ferroelectric insulating layer. The key property of a MFTJ is the coexistence of spin-dependent and polarization-dependent current in one device. Therefore, four resistance states can be obtained corresponding to different configurations of spin and polarization, as shown in Fig. 1.22 (c) [112].
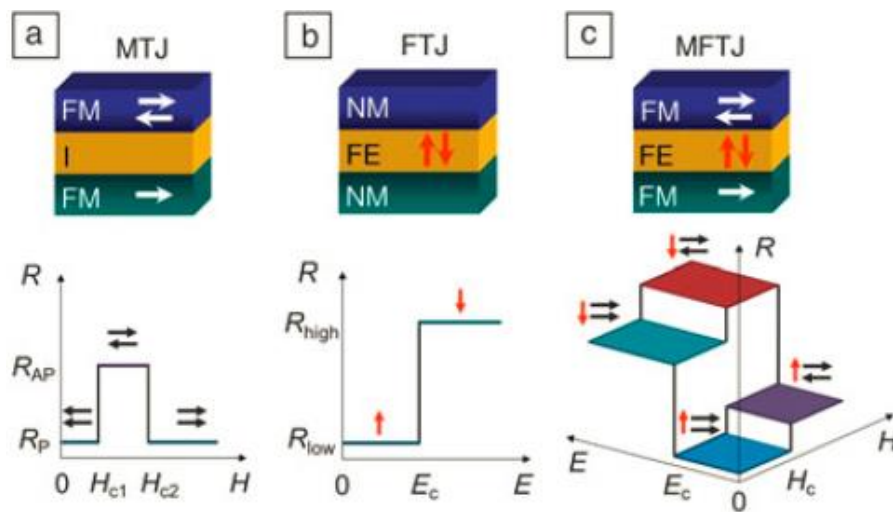
Figure 1.22 Schematic structures of the three types of tunnel junctions. (a) MTJ (b) FTJ and (c) MFTJ, respectively. Here, FM, I, NM, and FE stand for ferromagnetic metal, insulator, normal metal and ferroelectric, respectively. Horizontal and vertical arrows represent the direction of magnetization and polarization, respectively. Lower panels indicate the resistance response of these tunnel junctions to electric field (E) and magnetic field (H). Adapted from [112].

Experimentally, several groups have realized four-state MFTJ with different materials. Figure 1.23 shows the tunneling resistance dependence on magnetic

field for two different polarizations of the ferroelectric layer in a La$_{0.7}$Sr$_{0.3}$MnO$_3$/Ba$_{0.5}$Sr$_{0.5}$TiO$_3$/ La$_{0.7}$Sr$_{0.3}$MnO$_3$ MFTJ [113].
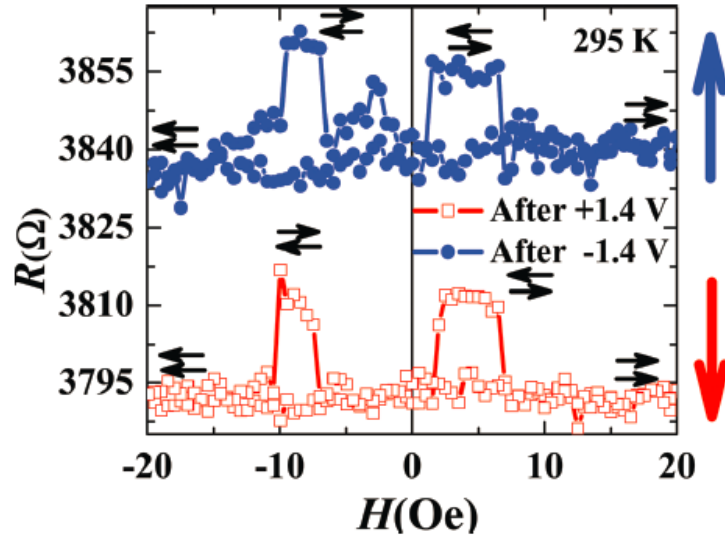
Figure 1.23 Experimental realization of four resistance states in a La$_{0.7}$Sr$_{0.3}$MnO$_3$/Ba$_{0.5}$Sr$_{0.5}$TiO$_3$/ La$_{0.7}$Sr$_{0.3}$MnO$_3$ MFTJ. Magnetic field dependent tunneling resistance corresponding to upward (blue arrow) and downward (red arrow) polarization of Ba$_{0.5}$Sr$_{0.5}$TiO$_3$. Adapted from [113].

On the other hand, the TMR can be controlled by the polarization direction of the ferroelectric layer in a reversible and non-volatile manner. As shown in Fig. 1.24, the TMR of the Fe/BaTiO$_3$/La$_{0.67}$Sr$_{0.33}$MnO$_3$ MFTJ can be reversibly controlled by switching the polarization direction of the BTO layer with an external electric pulse [102]. Here, TMR is defined as $(R_{ap}-R_p)/R_p$, and R_{ap} and R_p are the resistance in the anti-parallel and parallel magnetic configurations, respectively.
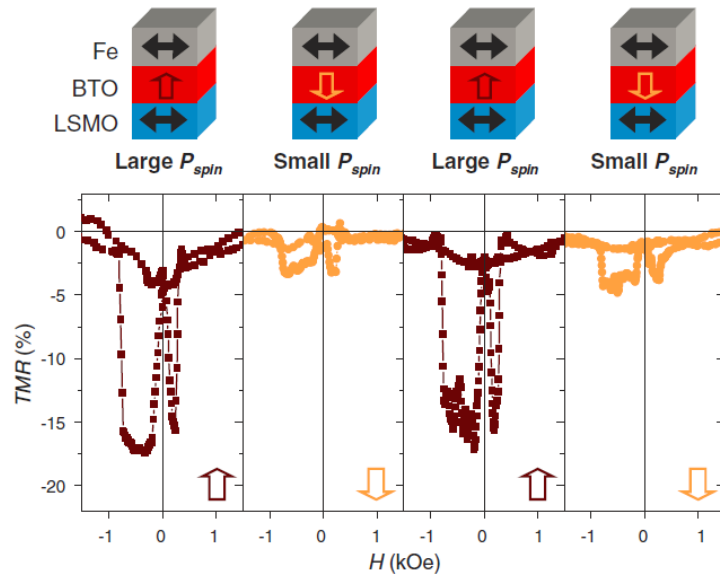
Figure 1.24 TMR dependence on magnetic field (H) with repeated switch of the polarization direction of the ferroelectric layer in a $Fe/BaTiO_3/La_{0.67}Sr_{0.33}MnO_3$ MFTJ, adapted from [102].

Other experimental demonstrations of MFTJ include: $Co/Pb(Zr_{0.2}Ti_{0.8})O_3/La_{0.7}Sr_{0.3}MnO_3$ heterostructure by Pantel *et al.* [114] and $La_{0.67}Sr_{0.33}MnO_3/BiFeO_3/ La_{0.67}Sr_{0.33}MnO_3$ heterostructure by Hambe *et al.*[115].

Although electric and ferroelectric control of ferromagnetism is promising for future applications, the exact origin is still under debate and some fundamental issues remain unsolved, such as the stability of ferroelectric thin films, the role of structural and interfacial defects, the ferroelectric and ferromagnetic dead layers *etc.*[112].

Chapter 2 Experimental methods

This chapter focuses on the experimental methods that were used in this thesis. It covers the following topics: (1) sample preparation (2) surface and structure characterization (3) electrical properties characterization (4) magnetic properties characterization.

2.1 Sample preparation

2.1.1 Substrate treatment

A good substrate with smooth surface is critical for high-quality epitaxial growth of oxide thin films and heterostructures, especially for the layer-by-layer two-dimensional growth. In many cases, the substrate quality or termination directly determines the physical properties of the thin films, heterostructures and interfaces. For example, as mentioned in section 1.3.1, the LAO/STO interface with TiO_2-terminated substrate (*n*-type) is conducting while it becomes insulating with SrO-terminated substrate (*p*-type) [57]. Another example is that the polarization direction of $BiFeO_3$ grown on $La_{0.7}Sr_{0.3}MnO_3$ can be directly controlled by the termination of $La_{0.7}Sr_{0.3}MnO_3$ (MnO_2-terminated or $La_{0.7}Sr_{0.3}O$-terminated) [116].

In this section, I introduce the treatment methods for three types of substrates that were used in this thesis-STO, Nb doped STO (NST) and $(LaAlO_3)_{0.3}(Sr_2AlTaO_6)_{0.7}$ (001) (LSAT).

STO substrate is probably the most commonly used substrate for oxide thin films. The commercially available STO substrate normally has a mixed termination, i.e. SrO and TiO_2. In 1994, Kawasaki *et al.* obtained TiO_2-terminated STO (001) substrate by selective etching of SrO with a pH-

controlled NH_4F-HF solution [39]. Later, in 1998, this technique was improved by Koster *et al.*[40]. In this thesis, the STO substrates were treated in three steps following this method. Firstly, the STO substrate is ultrasonically treated in deionized water for 10 minutes and then dried with flowing nitrogen. Secondly, the dried substrate is ultrasonically treated in buffered NH_4F-HF solution for 30 seconds and then dried with flowing nitrogen. Thirdly, the substrate is annealed in air at 950 °C for 1.5 hour with a ramping up and ramping down rate of 5 °C/min and 3 °C/min, respectively.

Figures 2.1 (a) and (b) show the atomic force microscopy (AFM) image of an as-received and treated STO (001) substrate, respectively. It can be seen that the treated surface is much smoother than the as-received one. Figures 2.1 (c) and (d) show the surface profile along the straight lines depicted in (a) and (b), respectively. Clear and sharp steps with a step height of ~0.4 nm (which corresponds to one unit cell of STO) can be seen in (d), while the step height in (c) is not well-defined. These results indicate that the three-step treatment significantly improves the surface quality of the STO substrate.

This three-step treatment can also be applied to NST (001) substrates and similar results to those of STO can be obtained. For LSAT (001), it is annealed in air at 1300 °C for 2 hours with a ramping up and ramping down rate of 5 °C/min. This process results in high surface quality similar to that of STO.
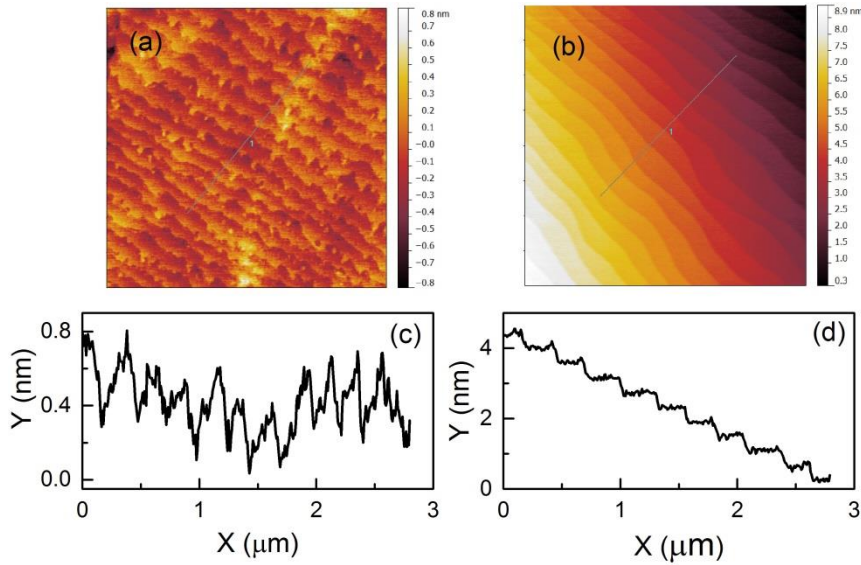
Figure 2.1 Atomic force microscopy image (4×4 μm^2) of an as-received (a) and HF treated (b) STO (001) substrate. (c) and (d) show surface profiles along the solid lines in (a) and (b), respectively.

2.1.2 Pulsed laser deposition

Pulsed laser deposition (PLD) is a physical vapor deposition technique. Most of the samples studied in this thesis were prepared by this technique. PLD has been widely used to deposit oxide thin films since the first successful preparation of superconducting Y-Ba-Cu-O thin films in 1987 by Dijkkamp *et al.*[117]. As compared to other deposition techniques, PLD is relatively simple, has a fast growth rate, very versatile and does not require ultrahigh vacuum.

Figure 2.2 shows schematic diagram of the PLD setup in our laboratory. The main parts of the setup are: a vacuum chamber, a KrF excimer laser with a wavelength of 248 nm, vacuum pumps, substrate and target carousel and reflection high-energy electron diffraction (RHEED).

The basic steps for thin film depositions are: (1) Pump down the base vacuum level of the main chamber down to 10^{-8}-10^{-9} torr to minimize contamination. (2) Load the substrate and target to their corresponding carousel and set up the

distance between the substrate and target. (3) Set up the gas pressure (O_2, N_2 or Ar) and heat the substrate to designated temperature. (4) Turn on laser and adjust its energy to ablate the target and start the deposition process. Both the target and substrate can be rotated by their corresponding carousels. This rotation process gives more homogenous films, especially for thick films. (5) After the deposition, the sample is cooled down to room temperature and unloaded.

Next, I discuss step (4) in details as it is the key step in the whole PLD process. During this step, a plume, which consists particles like atoms, molecules and plasma *etc.*, is generated from the target and then nucleates on the substrate, forming the thin films. Due to the high energy particles, the deposition process is far from equilibrium. Depending on the thermodynamic parameters of the deposition process and the substrate surface, the initial growth modes can typically be classified into three types: (i) Layer-by-Layer type or Frank-van der Merwe type, which means that each new layer starts to grow only after the last one has completed (ii) Island type or Volmer-Weber type, which means island formation on substrate due to a multi-layer conglomerate of adsorbed atoms. (iii) Mixed type or Stranski-Krastanov type, which is a mixture of the previous two types. To ensure high surface and interface quality of the thin films, the layer-by-layer type is highly desirable.

To achieve layer-by-layer growth, a smooth substrate, such as HF-treated STO, is needed. In addition, the thermodynamics can be controlled experimentally by the substrate temperature, laser energy density and deposition pressure. In my experiments, I normally used substrate temperature of 700-950 °C, laser

energy density of 1-2 J/cm^2 and oxygen pressure of 10^{-4}-10^{-3} torr. To monitor the growth mode, an *in-situ* RHEED was used during the deposition. A brief introduction to RHEED is discussed in the next section.
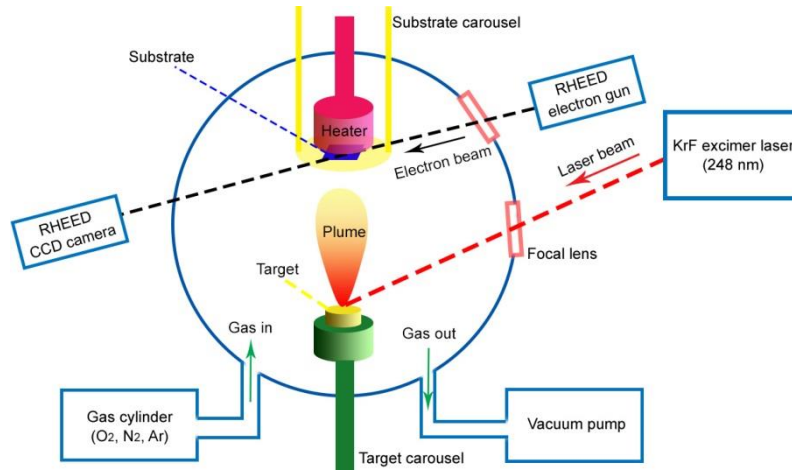
Figure 2.2 Schematic diagram of the main parts of a PLD chamber equipped with an *in-situ* RHEED.

2.1.3 RHEED

RHEED is a common technique used in molecular beam epitaxy (MBE) and PLD to characterize the surface of crystalline thin films. As shown in Fig. 2.2, a high-energy (10-50 KeV) electron beam emitted from an electron gun strikes the substrate at a glancing angle ($< 8°$). The small glancing angle makes the electrons only sensitive to a few unit cells of the sample surface, and thus, RHEED is a surface-sensitive technique. Subsequently, a small fraction of the incident electrons is diffracted by the substrate and interfere constructively at some specific angle, forming RHEED patterns on the CCD camera. In real experiments, the electron gun is kept in ultra-high vacuum ($\sim 10^{-9}$ torr) to minimize electron scattering by impurities. While RHEED can operate in a wide temperature range (from room temperature to hundreds of degrees), I

normally operated RHEED at the sample growth temperature (normally several hundred degrees) to monitor the film deposition process.

Figure 2.3 shows the RHEED pattern of a HF-treated TiO_2-terminated STO (001) substrate at 760 ℃. The two main features are: (1) Some discrete bright spots lying on two circles, which are called the zeroth and first Laue zone as shown in the figure. (2) Some bright streaks, which are called Kikuchi lines.
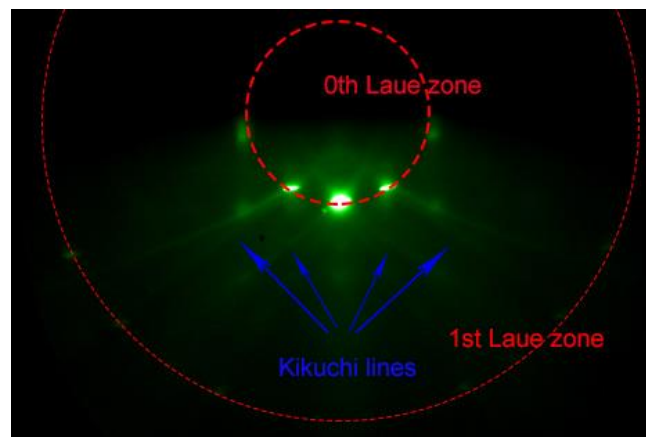
Figure 2.3 RHEED pattern of a TiO_2-terminated STO (001) substrate. The zeroth and first Laue zone are shown as dashed red circles and the Kikuchi lines are indicated by the blue arrows.

The RHEED pattern can be explained by electron diffraction theory. Basically, the two conditions for electron diffraction are: (1) Energy conservation and (2) Momentum conservation. The simplest model is electron diffraction by a one-dimensional crystal, as shown in Fig. 2.4 (a)-(b). The condition for constructive interference is:

$$a \bullet \cos \theta_i - a \bullet \theta_f = n \bullet \lambda \qquad \text{(eq. 2.1)}$$

where a is the lattice constant for the one-dimensional lattice, θ_i and θ_f stand for the incident and diffracted angle of the electrons, respectively. n is an

integer and λ is the wavelength of the electrons. In reciprocal space, eq. 2.1can be written as:

$$k \bullet \cos \theta_i - k \bullet \theta_{f} = B_n \qquad \text{(eq. 2.2)}$$

where $k = 2\pi/\lambda$ and $B_n = 2\pi n/a$. Since the diffraction process is elastic, the incident and diffracted electrons have the same wavelength (λ) and wave-vector (k). From eq. 2.2, one can see that the final states of the diffracted electrons form concentric circles at the base of cones of half angle θ_f, as shown in Fig. 2.4 (b) [118].

For thin film depositions, a more realistic model needs to be considered, i.e. a two-dimensional lattice. Since RHEED is surface-sensitive, a two-dimensional lattice is enough to understand the main features during our experiments. In this model, the energy and momentum conservation conditions are:

$$|\mathbf{k}_f| = |\mathbf{k}_i| \qquad \text{(eq. 2.3)}$$

$$\mathbf{k}_f - \mathbf{k}_i = \mathbf{G}_m \qquad \text{(eq. 2.4)}$$

where $\mathbf{k}_f$ and $\mathbf{k}_i$ are the wave-vectors of diffracted and incident electrons, respectively, $\mathbf{G}_m$ is a reciprocal lattice vector. These conditions can be transformed into Ewald-Laue conditions as shown in Fig. 2.4 (c)-(d). The energy conservation condition is represented by an Ewald sphere as shown in Fig. 2.4 (c). Since the reciprocal lattice for a two-dimensional lattice is a family of evenly spaced parallel rods, constructive interference only happens at the intersection of the Ewald sphere and the parallel rods, as shown in Fig. 2.4 (d). These intersections are the bright spots observed in the RHEED pattern.
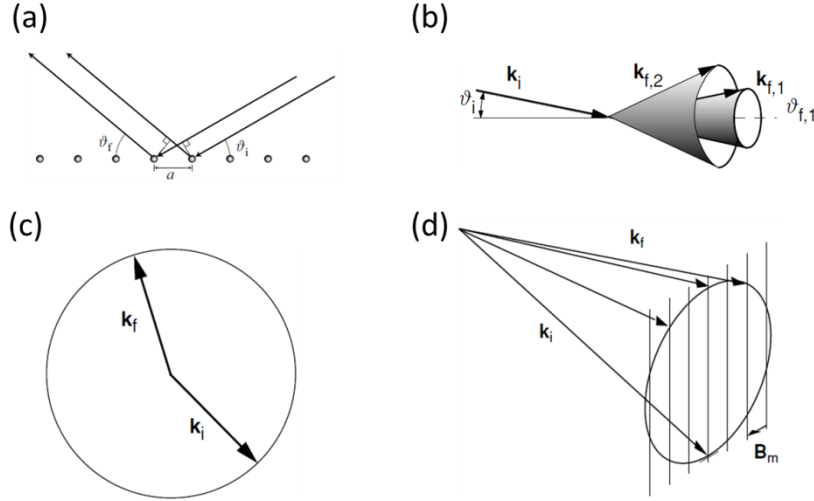
Figure 2.4 Electron diffraction conditions for one-dimensional ((a)-(b)) and two-dimensional lattice ((c)-(d)). Here, a is the lattice constant for the one-dimensional lattice. K_i and K_f stand for the wave-vector of incident and diffracted electrons, respectively. ϑ_i and ϑ_f stand for the incident and diffracted angle of the electrons, respectively. B_m is the reciprocal lattice vector of the two-dimensional lattice. Adapted from [118].

The Kikuchi lines are formed by the diffraction of the inelastically scattered electrons. The underlying mechanism is more complex and beyond the scope of this thesis. Nevertheless, the information one can get from the sharp Kikuchi lines is that the crystal has perfect surface and bulk lattices [118].

RHEED pattern can also be used to determine the lattice parameter of the substrate or thin film if the distance between the camera and the pattern and the electron energy are known. As shown in Fig. 2.5, by using the Ewald-Laue method, in reciprocal space, the angle between diffracted beams φ can be written as:

$$\varphi = 2\pi/k \cdot a \qquad\qquad \text{(eq. 2.5)}$$

where k is the wave-vector of the electrons and a is the lattice constant. In real space, φ can be written as:

$$\varphi = \tan^{-1}(d/L) \qquad\qquad (eq.\ 2.6)$$

where d is the distance between the bright spots in the RHEED pattern and L

is the distance between the camera and the RHEED pattern.
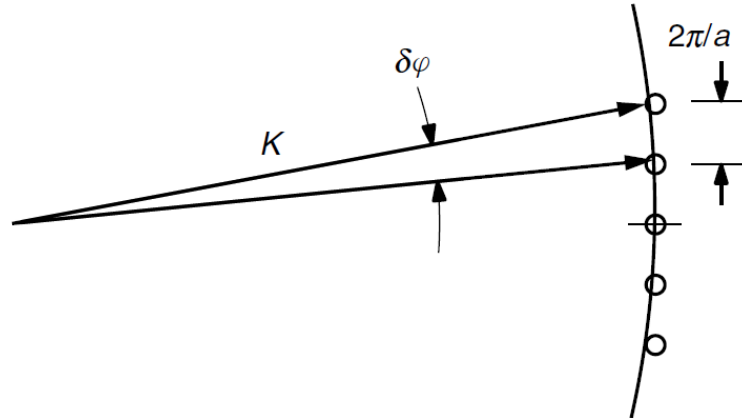
Figure 2.5 Lattice parameter measurement from RHEED pattern, adapted from [118].

Having explained the RHEED pattern, we now show how to monitor the

layer-by-layer deposition of thin films. During the deposition, we monitor the

specular spot of the RHEED pattern. Figure 2.6 (a) shows the real-time

monitor of RHEED intensity as a function of time for a 15 uc LAO on STO

(001) substrate. The inset shows similar pattern as that of Fig. 2.3, indicating

that the LAO thin film is fully constrained on STO substrate. Here, one

oscillation indicates one unit cell of LAO deposition. As shown in Fig. 2.5 (b),

the RHEED intensity oscillates with different coverage of LAO on the

substrate. The RHEED intensity is proportional to the roughness, and thus, the

coverage of the thin film. The rougher is the surface, the more electrons are

diffusively scattered, and thus, less electrons can contribute to the RHEED

intensity. From RHEED oscillations, the growth rate of the thin film can be

determined, which allows us to control the film thickness down to sub-atomic

layer level.
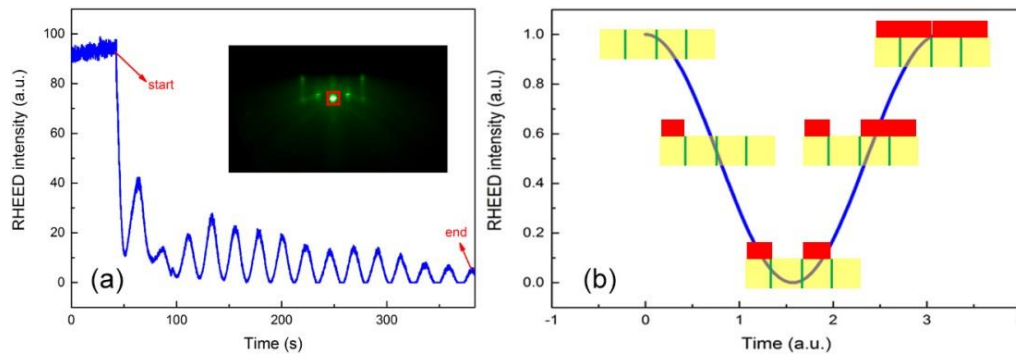
Figure 2.6 (a) RHEED oscillations during a deposition of 15 uc of LAO on STO (001). The inset shows the RHEED pattern after the deposition. (b) Schematic illustration of the relation between the oscillation and film coverage, here the yellow and red rectangles represent the substrate and one unit cell of the film, respectively.

2.2 Surface and structure characterization

2.2.1 Atomic force microscopy

Atomic force microscopy (AFM) is a method to measure the surface of a

sample with a lateral resolution of several nanometers and a vertical resolution

of less than 1 Å [119]. The high resolution and relatively simple setup have

made AFM one of the most popular and important techniques to measure,

image and manipulate sample surfaces at the nanometer scale.

So how does AFM measure the surface of a sample surface? By "touching" it

with a sharp tip [120]. I illustrate the measurement process with the help of

Fig. 2.7, which is a schematic diagram of the main components of an AFM

setup. Basically, the main components are: a sharp tip attached to a cantilever,

a focused laser beam and a split 4-cell photodiode. During the measurement,

the tip is scanned over the sample and the cantilever is either bended or

twisted due to the tip-sample forces. To amplify the small movement of the

cantilever and increase the sensitivity, a laser beam is shone on the cantilever and reflected onto the split 4-cell photodiode. Thus, the bending or twisting of the cantilever can be simultaneously transformed into electronic signals, which give information of the sample surface.
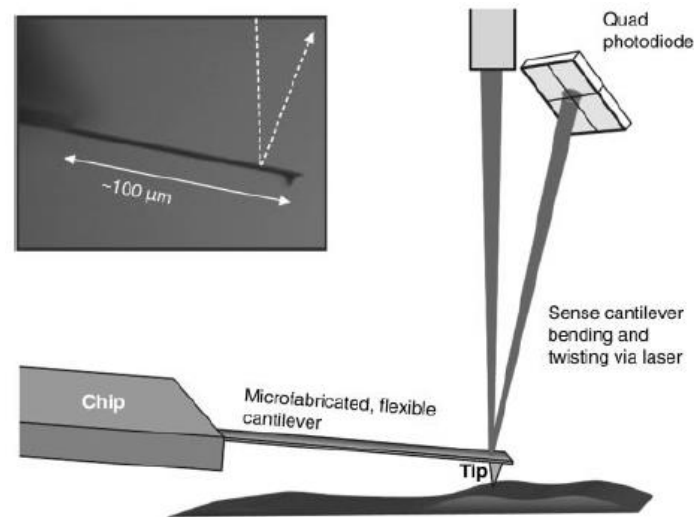
Figure 2.7 Schematic illustration of the main components of a AFM setup. The inset is an optical image of the cantilever/tip. Adapted from [120].

The origin of the resultant image is the tip-sample forces. In experiments, the forces can be very complex depending on the environment (e.g. liquid or air), and temperature *etc.* As all my experiments are carried out in air at room temperature, we only consider this special case here. In this situation, the main forces are: van der Waals (vdw) and electrostatic repulsion. And the most important parameter for these forces is the tip-sample distance. As shown in Fig. 2.8, when bringing the tip and sample close from infinite distance, the van der Waals attractive force starts to build up due to the dipole-dipole interaction between the atoms from the tip and the sample. On further decreasing the tip-sample distance below 1 nm, the electrostatic repulsion increases steeply due to the Pauli exclusion principle. The overall potential is phenomenologically expressed by the Lennard-Jones (L-J) potential [121].

47
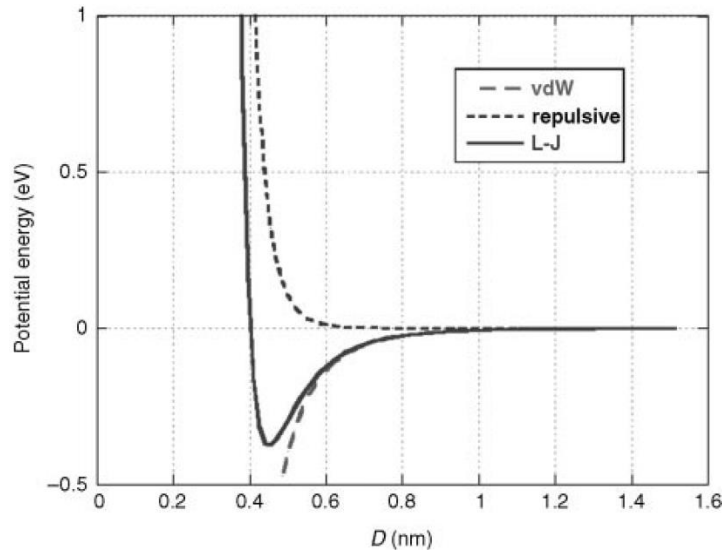
Figure 2.8 Distance dependence of L-J potential overlaid on Van der Waals (vdW) and electrostatic repulsive potentials. Here, positive and negative energy correspond to repulsive and attractive forces, respectively. Adapted from [121].

There are generally three operation modes for AFM, i.e. contact mode, non-contact mode and tapping mode. In contact mode, the tip and sample surface is always in close contact with a small tip-sample distance (usually in the repulsive region of Fig. 2.8). And the topographic image of the surface is recorded by scanning the sample with a constant tip-sample distance. In non-contact mode, contrary to contact mode, the tip does not contact the sample surface during the measurement. The cantilever is oscillated at or close to its resonant frequency, and the topographic image of the surface is recorded with a constant amplitude or frequency by adjusting the tip-sample distance. The oscillation amplitude is typically a few nanometres, and hence, in the attractive region of Fig. 2.8. Both contact mode and non-contact mode have their strengths and weaknesses. For contact mode, although it is the easiest mode, the tip may damage the sample during the experiment. For non-contact

48

mode, although it's suitable for soft samples, it fails if the sample is covered with a thin fluid contaminant layer. As an intermediate mode, the tapping mode combines the merits and circumvents the drawbacks of the contact mode and non-contact mode, and hence, it is the most popular mode in ambient environment. The operation principle of the tapping mode is similar to that of non-contact mode, except that the tip will contact the sample. All the AFM images in this thesis are taken in the tapping mode in air at room temperature and an example is shown in Fig. 2.1.

2.2.2 X-ray diffraction

X-ray diffraction (XRD) is one of the most important techniques to determine the atomic and molecular structure of a crystal. The working principle for XRD is schematically shown in Fig. 2.9. An incident X-ray beam with a fixed wavelength (λ) is shone on the crystal and reflected by different crystal planes. Subsequently, the intensity of the reflected X-ray is monitored by a collector. Under certain conditions, the reflected X-ray interfere constructively, giving rise to intensity peaks in XRD spectra. The diffraction conditions are: (1) energy conservation and (2) momentum conservation. As the scattering process is elastic, the energy conservation condition means that the incident and diffracted X-rays have the same wavelength. The momentum conservation condition can be expressed as:

$$2d\sin\theta = n\lambda \qquad\qquad \text{(e.q. 2.7)}$$

where d is the distance between two adjacent crystal planes, i.e. lattice constant, θ is the incident angle, n is an integer, λ is wavelength of the X-ray. In our XRD, we use Cu K_α line, which has a wavelength of 1.5406 Å.
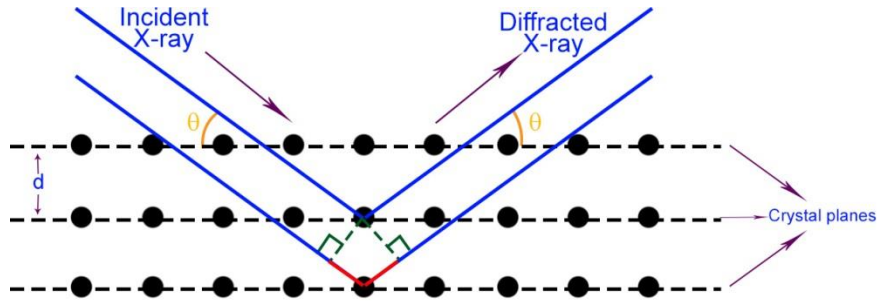
Figure 2.9 Schematic illustration for XRD. Here, d is the distance between two adjacent crystal planes, i.e. lattice constant. θ is the incident angle. The path difference of the X-ray diffracted by different crystal planes is coloured in red.

The most common mode for XRD is the θ–2θ scan mode. In this mode, the direction of the X-ray source is fixed, while the sample is rotated from 0 to θ, in the meantime, the detector is rotated from 0 to 2θ. The rotation speed of the detector is always two times of that of the sample. Figure 2.10 shows the θ–2θ scan for a 100 nm $Ba_{0.5}Sr_{0.5}TiO_3$ (BST)/STO (001) sample. From the peak position, we can calculate the out-of-plane c-axis lattice constant of the thin film by using eq. 2.7. For the (002) peak of BST, 2θ=44.38°, n=2, λ=1.5406 Å, hence the out-of-plane constant d=4.08 Å. Both bulk STO and BST are cubic with lattice parameters of 3.905 Å and 3.95 Å, respectively. So one can see that BST thin film grown on STO (001) substrate is under in-plane compressive strain with an elongated out-of-plane constant.

It should be noted that θ–2θ scan can only give information of the out-of-plane c constant. To gain full structural information of the thin film, reciprocal space mapping (RSM) is required. RSM is an important tool to decide the structure of a crystal and the strain status of a thin film. Not only can it measure the out-of-plane c constant, but also in-plane constants (a and b). More details about RSM will be discussed in later chapters. While XRD can

50

operate in a wide range of temperature and pressure, all the XRD images in this thesis were taken at room temperature in air.
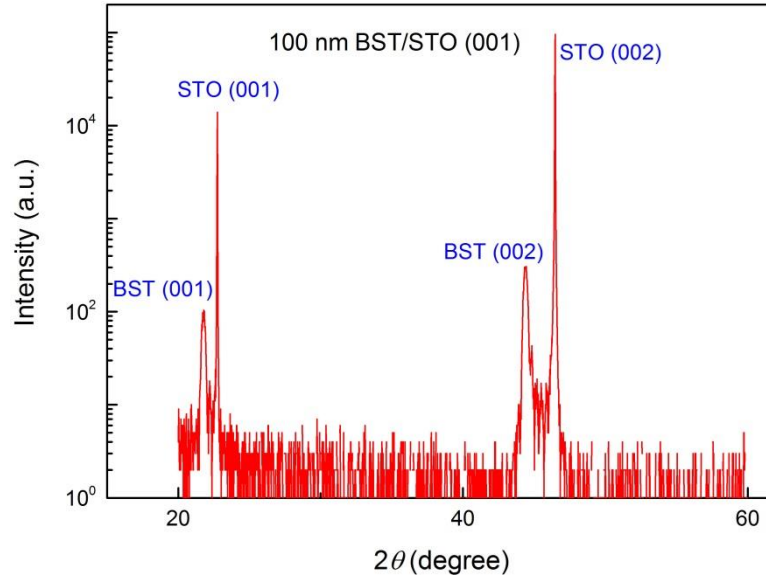
Figure 2.10 XRD θ–2θ scan of a 100 nm $Ba_{0.5}Sr_{0.5}TiO_3$ (BST) thin film deposited on a STO (001) substrate.

2.3 Electrical properties characterization

After analyzing the surface and structure of the samples, I now turn to discuss the electronic transport properties, which are the key properties for any electronics. All the transport properties were measured with a Quantum Design physical properties measurement system (PPMS), which allows one to control temperature from 2 to 400 K and apply an external magnetic field as large as 9 T. All the contacts were made with an ultrasonic aluminum wire bonder. This section covers three topics: (1) resistance (resistivity) measurement (2) Hall measurement and (3) magnetoresistance measurement.

2.3.1 Resistance measurement

Resistance is probably the most fundamental property for conductors. In this thesis, we study both two dimensional electron gas (2DEG) and three dimensional electron gas (3DEG). The resistances for 2DEG and 3DEG are

51

characterized by sheet resistance and resistivity, respectively. For a normal 3DEG, its resistance is defined as:

$$R = \frac{\rho L}{TW} \qquad \text{(eq. 2.8)}$$

Where R and ρ are resistance and resistivity, respectively. L, T and W are width, length and width of the conductor, respectively, as shown in Fig. 2.11. One can see that resistivity is independent of the geometry of the conductor and intrinsic of a material.

When the thickness of the conductor is much smaller than its length and width, i.e. $T<<L$, $T<<W$, the three dimensional conductor transforms into a two dimensional conductor, i.e. 2DEG. For a 2DEG, we define sheet resistance (R_s) as:

$$R = \frac{\rho L}{TW} = \frac{R_s}{W}L \qquad \text{(e.q. 2.9)}$$

$$R_s = \frac{\rho}{T} \qquad \text{(e.q. 2.10)}$$

One can see that R_s is independent of the geometry of the conductor, i.e. intrinsic to the material, as long as the thickness of the conductor is fixed.
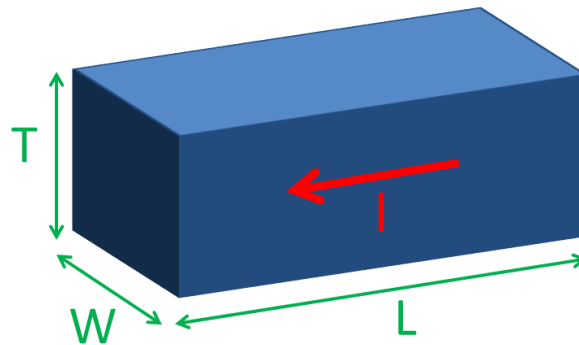
Figure 2.11 Geometry for resistivity measurement. Here, W, L, and T stand for width, length and thickness of the conductor. The current (I) flows from right to left as indicated by the red arrow.

Experimentally, to eliminate the contact resistance, a 4-probe measurement is required. There are generally two geometries for 4-probe measurement: Van der Pauw (VdP) geometry and linear geometry. Fig. 2.12 shows schematic diagram of the two geometries for a LAO/STO sample which has a dimension of $5\times5\times0.5$ mm^3.

In the VdP geometry, the current flows along one edge of the sample and the voltage is probed on the opposite edge. If the current flows from lead 1 to 2 and voltage is probed along lead 3 to 4, a resistance can be defined as $R_{12,34}$. Similarly, one can define $R_{34,12}$, $R_{14,23}$ and $R_{23,14}$. From reciprocity theorem, we know that $R_{12,34}= R_{34,12}$ and $R_{14,23}= R_{23,14}$. The relationship between R_s, $R_{12,34}$ and $R_{14,23}$ were formulated by Van der Pauw [122] as:

$$e^{\frac{-\pi R_{12,34}}{R_s}} + e^{\frac{-\pi R_{14,23}}{R_s}} = 1 \qquad\qquad \text{(eq. 2.11)}$$

If the resistance is isotropic (which is the case for all my samples), then $R=R_{12,34}= R_{14,23}$. Finally, the sheet resistance R_s can be simplified as:

$$R_s = \frac{\pi R}{\ln 2} \approx 4.53R \qquad\qquad \text{(eq. 2.12)}$$

In the linear geometry, if the current flows from lead 1 to 4 and the voltage is probed between lead 2 and 3, a resistance can be defined as $R_{14,23}$. Similarly, one can define $R_{41,32}$. If the resistance is isotropic, then $R= R_{14,23}= R_{41,32}$. To obtain the sheet resistance R_s in linear geometry, one has to fabricate a Hall bar to define the length (L) and width (W) of the conducting channel. Then, R_s can be obtained by using eq. 2.9.

One can see that the VdP method is relatively simpler as compared to the linear method, as the former does not require additional Hall bar fabrication. In this thesis, all the resistance measurements were carried out in the VdP geometry due to its simplicity. Fig. 2.13 shows temperature dependent sheet resistance (R_s-T) of a 10 uc LAO/STO sample from 2 to 300 K by using the VdP geometry. From the R_s-T curve, one can see that the sample is fully metallic from 300 to 2K as R_s increases monotonically with increasing temperature.
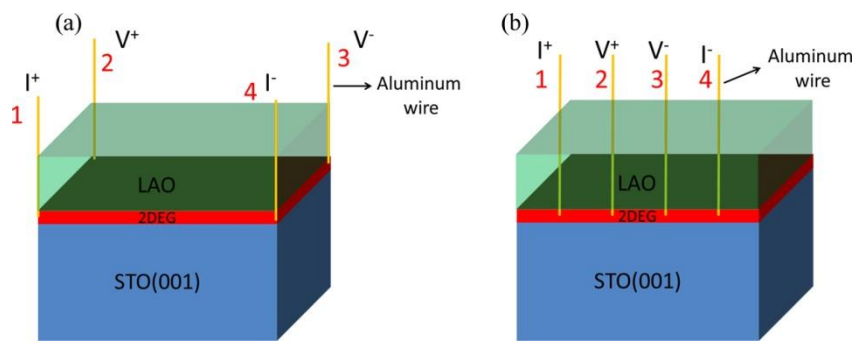
Figure 2.12 Schematic illustration of van der Pauw (a) and linear (b) measurement of resistance of the 2DEG at LAO/STO interface. The four contacts (1, 2, 3 and 4) are formed by aluminum wire bonding. Current flows from I^+ to I^- and voltage is probed between V^+ and V^-. The sample dimension is $5 \times 5 \times 0.5$ mm^3.
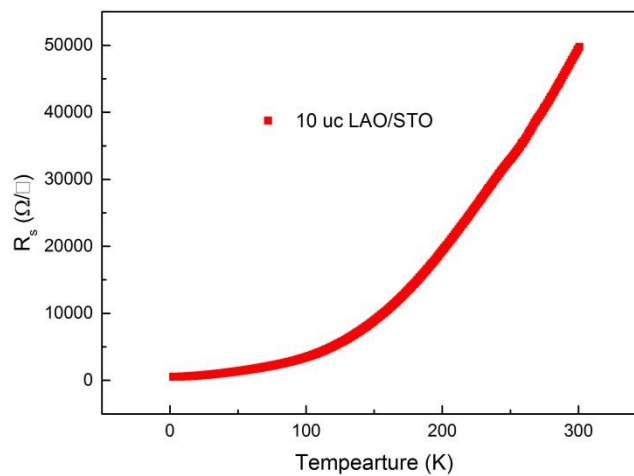
Figure 2.13 Sheet resistance dependence on temperature for a 10 uc LAO/STO sample from 2-300K. The sample was deposited at T=760 ℃ and P_{O2}=10^{-3} torr. Subsequently, it was annealed in air at T=600 ℃ for 1 hour.

2.3.2 Hall measurement

Hall measurement is another important measurement to characterize a conductor. From Hall measurement, we can get important information, such as carrier type (electron or hole), carrier density and carrier mobility. These information help us to understand the band structure, electron-electron scattering, electron-phonon scattering *etc.* of a material.

Figure 2.14 shows the geometry for Hall measurement of a three-dimensional conductor with length *L*, width *W* and thickness *T*. A current (*I*) flows along the *L* edge of the conductor. When an external magnetic field (*B*) is applied perpendicular to the current, the charges of the current are deflected by the Lorentz force, leading to positive and negative charge accumulation at different edges of the conductor, as shown in Fig. 2.14. These accumulated charges create a Hall voltage (V_H) along *W* edge. Finally, the equilibrium condition is reached when the Lorentz force is equal to the electrostatic force created by the Hall voltage, i.e.

$$qvB=qE=qV_H/W \qquad \text{(eq. 2.13)}$$

where *q* and *v* are the charge and velocity of the carrier, respectively. *E* is the electric field created by the Hall voltage. *B*, V_H and *W* have been defined above. The current (*I*) created by the mobile charged carriers is defined as:

$$I=qnv(WT) \qquad \text{(eq. 2.14)}$$

where *n* is three-dimensional carrier density, *I*, *q*,*v*, *W* and *T* have been defined above.

From eq. 2.13 and 2.14, one can derive Hall resistance as:

55

$$R_H = V_H/I = B/(qnT) \qquad \text{(eq. 2.15)}$$

Therefore, the three dimensional carrier density n can be deduced if one knows the Hall voltage V_H, current I, the applied magnetic field B, the charge of the carrier q and the thickness of the sample T.

Furthermore, the resistivity ρ of a conductor can be written as:

$$\rho = \frac{1}{nq\mu} \qquad \text{(eq. 2.16)}$$

Where μ is the mobility of the charge carrier, which describes how quickly the carrier can move in the conductor. Hence, one can deduce μ by measuring the resistivity ρ, the charge of the carrier q and the three dimensional carrier density n. As all the systems I studied are n-type conducting, i.e. only itinerant electrons contribute to the current, q in eq. 2.13-2.16 can be replaced with negative elementary charge $-e$.

For a two-dimensional electron gas, we define sheet carrier density as:

$$n_s = nT \qquad \text{(eq. 2.17)}$$

From eq. 2.15 and 2.17, one can derive:

$$R_H = -\frac{B}{en_s} \qquad \text{(eq. 2.18)}$$

Therefore, the two-dimensional sheet carrier density n_s can be obtained.

Furthermore, if one notice that sheet resistance (R_s) is defined as resistivity divided by the thickness of the conductor (T) and that sheet carrier density (n_s) is defined as three-dimensional carrier density (n) multiplied by the thickness

of the conductor (T), then by combining eq. 2.10, 2.17 and 2.18, one can derive:

$$\mu = \frac{1}{eR_s n_s} \qquad\qquad \text{(eq. 2.19)}$$

Where μ is the mobility for a two-dimensional electron gas.
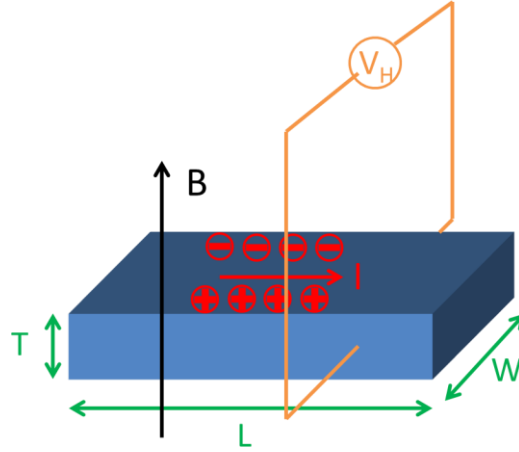
Figure 2.14 Geometry for Hall measurement of a three-dimensional conductor.

Experimentally, we use the Van der Pauw geometry to measure the Hall effect. As shown in Fig. 2.15 (a), a current is applied between lead 2 and 4, while the Hall voltage is measured perpendicular to the current, i.e. between lead 1 and 3. Figure 2.15 (b) shows Hall measurement data of an as-grown 10 uc LAO/STO sample at 300 K, from -9 to 9 T, by using the Van der Pauw geometry. The negative slope indicates that the charge carrier is electron. From linear fitting of the experimental data, one can find that the slope of the straight line is -5.90 Ω/T. By using eq. 2.18, the sheet carrier density n_s is deduced to be 1.06×10^{14} cm^{-2}. From the resistance measurement, the sheet resistance R_s is found to be 8783 Ω. Thus, by using eq. 2.19, the carrier mobility μ is deduced to be 6.7 cm^{2}V^{-1}s^{-1}.
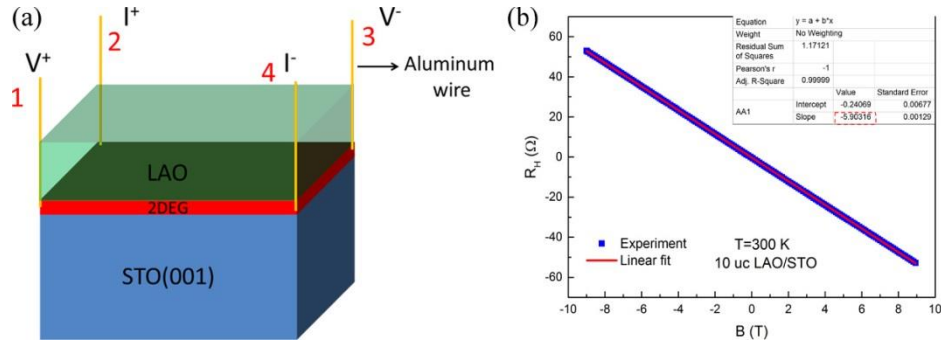
Figure 2.15 (a) Schematic illustration of Van der Pauw geometry for Hall measurement. (b) Hall resistance dependence on magnetic field for an as-grown 10 uc LAO/STO sample at 300 K. Inset shows the details of linear fitting of the experimental data.

It should be noted that the Hall effect introduced above is generally referred as normal Hall effect, which is generally observed in non-magnetic metal with one type of charge carrier. For normal Hall effect, the Hall resistance dependence on magnetic field is linear. However, for some materials, the Hall resistance dependence on magnetic field is non-linear. This type of Hall effect is called anomalous Hall effect (AHE), which involves either ferromagnetism [123] or multiple types of carriers [124]. Detailed discussion of AHE will be provided in later chapters.

2.3.3 Magnetoresistance measurement

Magnetoresistance (MR) measurement is the measurement of resistance with external magnetic field. It is defined as:

$$\text{MR} = \frac{R(B) - R(0)}{R(0)} \times 100\% \qquad \text{(eq. 2.20)}$$

Where $R(B)$ and $R(0)$ are resistances with a magnetic field of B and 0, respectively. MR is generally measured in a linear 4-probe geometry as shown in Fig. 2.12 (b), the external magnetic field can be applied along any direction depending on different experiments.

In the literature, there are many types of MR, such as ordinary MR, anisotropic MR (AMR), giant MR (GMR), clossal MR (CMR), tunnelling MR (TMR) and extraordinary MR (EMR) *etc.* In addition, MR is dependent on many external factors, such as temperature, the magnitude of magnetic field, the angle between current and magnetic field, localization, antilocalization and the magnetic properties of the materials *etc.* Due to the complexity of MR, here, I only introduce the ordinary MR and AMR, the others will be discussed in later chapters if applicable.

For a normal non-magetic metal, MR is normally positive and quite small (smaller than one percent). In the presence of an external magnetic field, an electron orbits around the magnetic field due to the Lorentz force. Thus it does not contribute to electric current until it is scattered. After the scattering, the electron will begin another cyclotron obit and so on. Overall, the net effect is that the electron's mean free path is decreased by the magnetic field because it is deflected away from its initial path by the Lorentz force. In this case, MR is proportional to the square of magnetic field, i.e. B^2. This is known as Kohler's rule:

$$MR = \frac{\Delta\rho}{\rho(0)} = a(\frac{B}{\rho(0)})^2 \qquad\qquad (eq.\ 2.21)$$

where $\rho(0)$ is the resistivity without magnetic field and $\Delta\rho$ is the difference of resistivity with and without magnetic field. B is magnetic field and a is a constant.

For a typical magnetic metal, the sign and magnitude of the MR is dependent on the relative direction of the current I and the magnitization M (or the external magnetic field). As shown in Fig. 2.16, the two most important configurations are: (1) parallel configuration, where I is parallel to M and (2)

perpendicular configuration, when *I* is perpendicular to *M*. Figure 2.17 shows

MR measurement of a 30 nm Ni thin film in the two configurations. One can

see that the two MR curves are quite different and hysteretic. The peak

positions correspond to the coercive field. The hysteresis loops indicates that

MR is related to magnetization, rather than magnetic field. In this case, the

Kohler's rule is modified as:

$$MR = \frac{\Delta\rho}{\rho(0)} = a\left(\frac{B}{\rho(0)}\right)^2 + b\left(\frac{M}{\rho(0)}\right)^2 \qquad \text{(eq. 2.22)}$$

Where *M* is magnitization, *a* and *b* are constants.
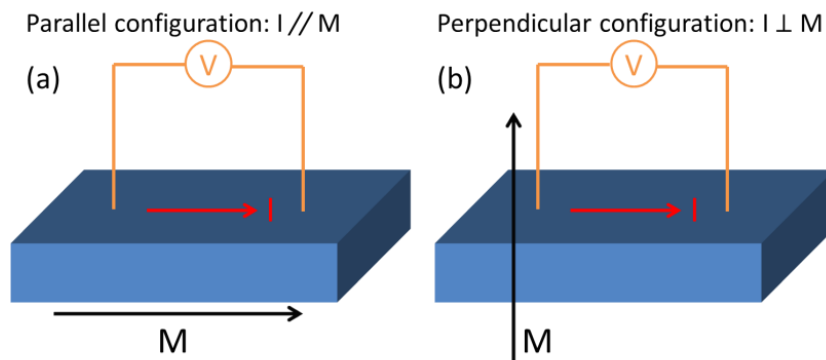
Figure 2.16 Parallel (a) and (b) perpendicular configurations for MR measuremnt, respectively.
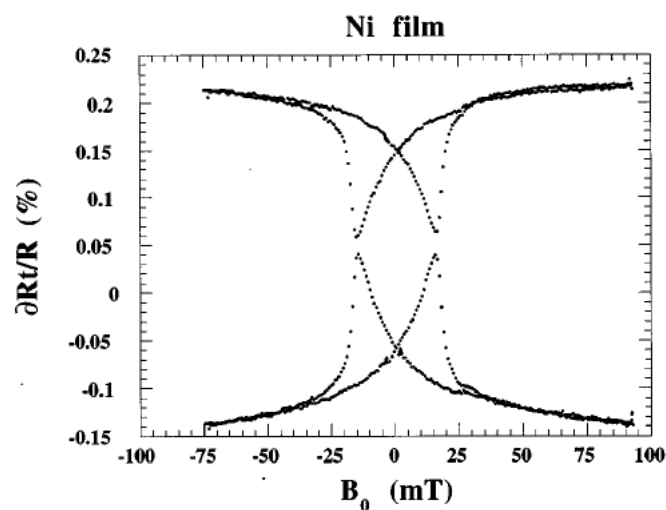
Figure 2.17 MR measurement of 30 nm Ni thin film in parallel (top) and transverse (bottom) geometry, respectively. Adapted from [125].

60

2.4 Magnetic properties characterization

Depending on their response to an external magnetic field, materials are generally classified into one of the following categories: diagmagnetic, paramagnetic, ferromagentic, antiferromagnetic and ferrimagnetic. In this thesis, I only focus on diamagnetism, paramagnetism and ferromagnetism.

Diamagnetism occurs in all materials with completely filled shells, and thus, the total spin magnetic moment is zero. Examples of diamagnets are: He, Ne, Ar and $SrTiO_3$. These materials are weakly repelled by an external magnetic field. On the other hand, paramagnetism occurs in atoms or ions with partially filled outer shells. Examples of paramagnets are: Na, Au and Pt. These materials are weakly attracted to an external magnetic field. Ferromagnetism occurs when all spins are aligned and point along the same direction below Curie temperature (T_c). Examples of ferromagnets are: Fe, Co, Ni and $SrRuO_3$. Ferromagnets are strongly attracted to an external magnetic field, as compared to paramagnets.

Experimentally, we focus on two types of measurements: temperature dependent magnetic moment (*m-T*) measurement and magnetic field dependent magnetic moment (*m-H*) measurement. We used a Quantum Design Superconducting Quantum Interference Device-Vibrating Sample Magnetometer (SQUID-VSM) system to do these measurements. It allows us to control temperature from 400 to 2 K and magnetic field from -7 to 7 T. In addition, its high sensitivity (10^{-11} Am^2) allows us to measure weak magnetic signals, such as that of ultrathin ferromagnetic films.

Figure 2.18 shows qualitative scheme of the *m-H* and *m-T* curves for diamagnetism, paramagnetism and ferromagnetism. For diamagnetism, the *m-*

H curve is linear with a negative slope and the *m-T* curve is almost constant with a negative magnetic moment.
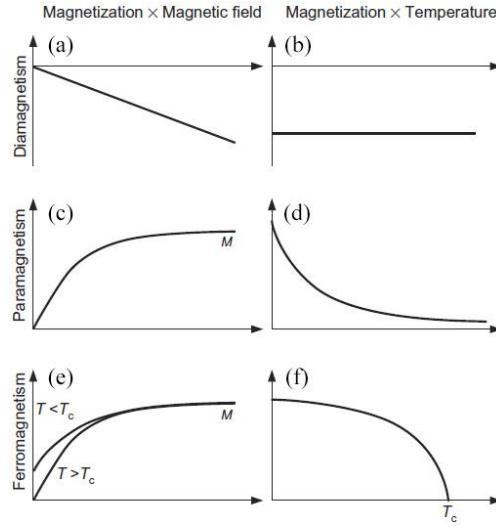
Figure 2.18 Qualitative scheme of the *m-H* and *m-T* curves for diamagnetism ((a) and (b)), paramagnetism ((b) and (c)) and ferromagnetism ((e) and (f)). Adapted from [126].

For paramagnetism, both the *m-H* and *m-T* curves are non-linear. The *m-H* curve can be fitted with Langevin equation:

$$M = N\mu L\left(\frac{\mu B}{k_B T}\right) = N\mu[\coth\left(\frac{\mu B}{k_B T}\right) - \frac{k_B T}{\mu B}] \qquad \text{(eq. 2.23)}$$

where *M* is magnetization (magnetic moment per unit volume), *N* is the number of magnetic moment per unit volume, μ is the magnitude of the magnetic moments, $L\left(\frac{\mu B}{k_B T}\right)$ is the Langevin function, *B* is magnetic field, k_B is Boltzmann constant and *T* is temperature. The *m-T* curve for paramagnetism can be fitted with the Curie-Langevin law:

$$M = \frac{C}{T}B \qquad \text{(eq. 2.24)}$$

where *C* is a constant called Curie constant. *M*, *T* and *B* have been defined. During the measurement, *B* is kept a constant, and thus, *M* is inversely proportional to *T*.

For ferromagnetism, both the *m-H* and *m-T* curves are the same as those of paramagnetism above Curie temperature T_c. Below T_c, the *m-T* curve gradually increases with decreasing temperature due to spontaneous magnetization of a ferromagnet. A more comprehensive picture of the *m-H* curve for a ferromagnet is shown in Fig. 2.19. The *m-H* (or *M-H*) hysteresis loop is probably the most fundamental experimental proof from ferromagnetism. Initially, the ferromagnet is in an non-magnetic, virgin state due to domain walls formation. Upon application of external magnetic field, domain walls start to align along with the external magnetic field and reveal the spontaneous magnetization (M_s). After removing the external magnetic field, the magnetization remains and is called remanence (M_r). The coercive field or coercivity (H_c) is the reverse field required to reduce the magnetization to zero.
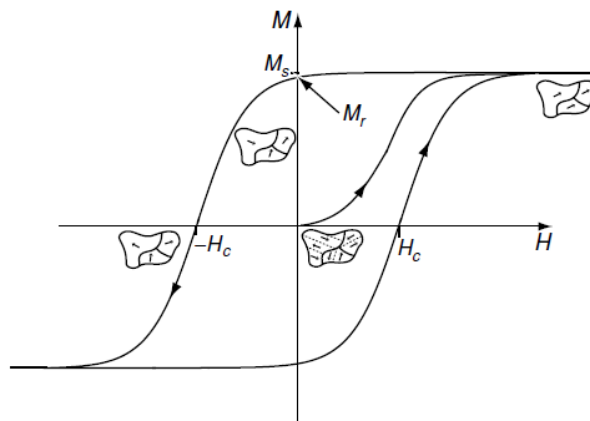
Figure 2.19 The hysteretic *M-H* loop of a ferromagnet. H_c, M_s and M_r represent coercive field, spontaneous magnetization and remanence, respectively. Adapted from [32].

The origin of ferromagnetism in different materials are normally explained by different mechanisms or models, for example the mean field theory of ferromagnetism for localized electrons, Heisenberg model for localized electrons, Stoner's band model of ferromagnetism for 3*d* metals, Ruderman-

Kittel-Kasuya-Yoshida (RKKY) interaction in $4f$ alloy and double exchange interaction in manganese oxides. It is difficult and unrealistic to cover every mechanism in this thesis, and thus, I will only discuss the origin of ferromagnetism based on specific materials in later chapers.

Chapter 3 Electron-soft phonon scattering in *n*-type SrTiO$_3$

Abstract

SrTiO$_3$ undergoes a cubic-to-tetragonal phase transition at T_c=105-110K, which can be described by a Brillouin zone corner Γ_{25} (111) soft phonon. Despite the fact that clear anomalies in lattice constant, specific heat, thermal expansion coefficient and sound velocity have been observed, the correlation between phase transition and electronic transport properties in n-type doped SrTiO$_3$ is still controversial. Here, we report phase transition induced electronic transport anomaly in temperature dependence of the temperature coefficient of resistance (TCR) consistently observed in a wide variety of SrTiO$_3$-based systems by detailed transport measurements and first-principles calculations. The observed TCR anomaly, which can be well fitted with the electron-Γ_{25} soft phonon scattering around T_c, is found to be caused by anomalies in both mobility and carrier density, with the former taking the dominant role. Moreover, the magnitude of the anomaly is found to decrease with increasing carrier density as a result of competing electron-electron and electron- Γ_{25} soft phonon scattering. These findings demonstrate the role of the electron-Γ_{25} soft phonon scattering in the conducting and possibly the superconducting mechanism in SrTiO$_3$-based systems.

3.1 Motivation

As introduced in section 1.2.1, due to its excellent physical properties and suitability as a substrate or buffer layer for oxide heterostructures, SrTiO$_3$ (STO) can be considered as the "silicon" for oxide electronics. As a prototype perovskite oxide, STO serves as a versatile playground for studying various strongly correlated effects, such as electron-electron coupling [19, 20, 23, 25,

26, 28, 101], electron-phonon scattering [19, 20, 23-26, 28, 101], metal-insulator transition [127], superconductivity [22, 128], ferroelectricity [53, 54] and ferromagnetism [66].

In its stoichiometric form, STO is a non-polar band insulator with an indirect bandgap ~ 3.27eV [15]. Itinerant electrons can be introduced into bulk STO (3D) by chemical doping (Nb, Zr, La or Ta), high-vacuum annealing and argon milling [19-21]. Alternatively, two-dimensional (2D) electron liquid can be induced at the interface of a polar oxide and STO by polar discontinuity [57] (such as $LaAlO_3/SrTiO_3$) or at the surface of STO by electrostatic doping with ionic liquid gating [129]. At low temperatures (<100 K), the conduction mechanism for both the 3D and 2D electrons can be well explained by the Baber electron-electron scattering, which considers both Coulomb and phonon-mediated electron-electron scatterings [20, 25, 26, 28, 30]. However, above 100 K, the resistivity deviates from Baber T^2 dependence [27]. In addition, the monotonic increase of electron mobility with decreasing temperature is either explained by the monotonic increase of dielectric constant and thus the TO zone centre phonon scattering [23] or the LO phonon scattering [29]. Furthermore, it was recently found by Lin *et al.* that the resistivity T^2 dependence for the single-band dilute $SrTiO_{3-\delta}$ could not be explained by the two known mechanisms for T^2 behavior-Baber scattering and Umklapp process, indicating the absence of a microscopic theory for momentum decay through electron-electron scattering in STO [27].

It is well known that STO undergoes an antiferrodisplacive soft-mode phase transition from cubic to tetragonal structure at T_c=105-110 K [16]. This second order phase transition is attributed to the softening of the zone corner phonon

Γ_{25} (111) at T_c [16]. Over the past decades, anomalies in physical properties associated with this phase transition at T_c, such as lattice constant [130], specific heat [131], thermal expansion coefficient [132] and sound velocity [133], have been observed experimentally. However, since the 1960s, the correlation between the phase transition and electronic transport properties in n-type STO remains controversial and unclear, although there have been theoretical predictions in 1972 [17]. Understanding the correlation between the phase transition and electronic transport properties is critical to improve our understanding of the second order phase transition and the electronic transport properties in STO as it lies at the boundary of the high and low temperature region.

With this long-standing problem in mind, we report, in this chapter, for the first time the phase transition induced electronic transport anomaly at T_c in n-type STO by detailed transport measurements and first-principles calculations. Unlike n-type BaTiO$_3$ (e.g. BaTiO$_{3-\delta}$), which shows resistivity discontinuity at its first-order phase transition temperatures [45], the resistivity of STO-based systems at its T_c is continuous and smooth. However, the temperature coefficient of resistance (TCR) shows a small but non-trivial peak at T_c for all the studied STO-based systems, regardless of the origin of the conductivity (defects, chemical doping or polar-discontinuity), dimension of the electron gas (3D or 2D) and crystalline direction, as long as the conducting channel lies in free-standing STO. Here, TCR is defined as TCR= $(1/R)(\mathrm{d}R/\mathrm{d}T)$. Due to the second order nature of the phase transition, the anomaly of TCR at T_c was found to be very small, on the order of 0.1%. We found that the anomaly in TCR is caused by anomalies in both carrier density and mobility, with the

latter dominating the change. Furthermore, it was found that the magnitude of the anomaly increases as carrier density decreases.

3.2 Experimental methods

To obtain a comprehensive picture of the correlation between phase transition and electronic transport properties in n-type STO, we prepared seven sets (A-G) of samples. $SrTi_{1-x}Nb_xO_3$ (NST) (001) single crystals (set A), oxygen deficient $SrTiO_{3-\delta}$ (001) single crystals (set B), $LaAlO_3/SrTiO_3$ (LAO/STO) (001) heterostructures (set C), $LaAlO_3)_{0.3}$-$(Sr_2AlTaO_6)_{0.7}$/STO (LSAT/STO) (001) heterostuctures (set D), $LaAlO_3/SrTiO_3$ (LAO/STO) (110) heterostructures (set E), $LaAlO_3/SrTiO_3/NdGaO_3$ (LAO/STO/NGO) (110) heterostrctures (set F) and $LaAlO_3/SrTiO_3/LaAlO_3)_{0.3}$-$(Sr_2AlTaO_6)_{0.7}$ (LAO/STO/LSAT) (001) heterostructures (set G).

Set A and B samples are three-dimensional conducting samples. NST samples (set A) with different Nb concentrations, *i.e.,* 0.01, 0.05, 0.1 and 0.5 wt% were commercially obtained from CrysTec GmbH, Germany. STO single crystals were annealed at 800℃, 10^{-6} torr for different durations to obtain oxygen deficient $SrTiO_{3-\delta}$ (set B).

Set C to G samples are two-dimensional conducting samples, which were prepared by pulsed laser deposition (PLD) equipped with *in-situ* reflection high-energy electron diffraction (RHEED). All the samples were prepared at 760℃ and an oxygen partial pressure of 10^{-3} torr with the fluence of laser energy of 1.5 J/cm^2 and laser repetition rate of 1 Hz. For set C and D, LAO or LSAT were deposited on atomically flat TiO_2-terminated STO (001) substrates from single crystalline LAO and LSAT target, respectively. The

STO (001) substrates were treated prior to the deposition with the standard method discussed in section 2.1.1. For set E samples, the deposition process were the same as that of set C and D, the only difference is the substrate treatment process. The STO (110) substrates were annealed in air at 1050 ℃ for 3 hours without HF treatment [134]. After the deposition, set C and E samples were post-annealed in air at 600 ℃ for 1 hour to compensate oxygen vacancies. For set F and G samples, STO and LAO were deposited successively on NGO (110) and LSAT (001) substrates, respectively. The NGO (110) and LSAT (001) substrates were annealed in air for 2 hours at 1050 ℃ and 1300 ℃ to obtain B-site terminated surfaces, respectively [62].

All the samples have a dimension of $5\times5\times0.5$ mm^3. Electrical contacts were formed on the corners of the samples by an aluminum wire bonder and all the electronic transport properties were measured in a Quantum Design physical property measurement system (PPMS) in the Van der Pauw geometry.

3.3 Electronic transport properties

3.3.1 Three-dimensional electron liquid

We first investigated the electronic transport properties of the three-dimensional conducting samples, *i.e.* NST and SrTiO$_{3-\delta}$, which can be viewed as three-dimensional electron liquids (3DEL).

Figure 3.1 shows electronic transport properties of a NST (0.01wt% Nb doped) and a SrTiO$_{3-\delta}$ sample. Both samples show fully metallic behavior from 300 to 2 K, no anomaly in temperature dependent resistance (*R-T*) curves can be observed in the whole temperature range as shown in Fig. 3.1 (a)-(b) (left scale). The resistance of the NST sample decreases monotonically from 2.94

Ω at 300 K to 4.83×10^{-4} Ω at 2 K. Similarly, the resistance of the SrTiO$_{3-\delta}$ sample also decreases monotonically from 6.23 Ω at 300 K to 1.99×10^{-3} Ω at 2 K. However, as shown by the right scale of (a)-(b), two peaks are visible for temperature dependent TCR for both samples. The main peak located at 10-30 K is a natural consequence of the Fermi liquid nature in STO-based systems at low temperature (2-100K). For a fermi liquid, whose resistance can be expressed as $R=AT^2+R_0$, where A is a constant and R_0 is residual resistance, a peak is expected at $(R_0/A)^{1/2}$ for TCR. A detailed discussed of the Fermi liquid behavior can be found in **Section 3.3.3**. Besides this main peak, a small peak can be observed around 108K, which coincides with the phase transition temperature T_c (105-110 K) of STO. Figures 1 (c)-(d) emphasize this peak by showing TCR over the temperature range 95-115 K.

To gain further insights into this TCR anomaly at 108 K, we performed detailed Hall measurements over the temperature range 95-115 K for every 0.5 K. The magnetic field was scanned from -2 to 2 T during the Hall measurements. Figures 3.1(c)-(d) show carrier density dependence on temperature (n-T) for each sample. Here, n is divided by n_{115K} for better visibility. The slope of each n/n_{115K}-T curve shows a sudden change around 108 K. The carrier density for each sample increases as temperature decreases from 115 to 95 K. As explained in one of our previous works, this increase is caused by the increase of the dielectric constant of STO as temperature is lowered [135]. It should be noted that the absolute change of carrier density over the temperature range 95-115 K is quite small (only a few percent). For the NST sample, n is 1.441×10^{18} and 1.405×10^{18} cm^{-3} at 95 and 115 K, respectively. For the SrTiO$_{3-\delta}$ sample, n is 8.658×10^{17} and 8.508×10^{17} cm^{-3} at

95 and 115 K, respectively. Figures 1(g)-(h) (left scale) show mobility
dependence on temperature (μ-T) extracted from the Hall measurements. Both
μ-T curves are smooth without any anomaly from 95 to 115 K. However, if we
define temperature coefficient of mobility (TCμ) similar to TCR as
TCμ=$(1/\mu)(d\mu/dT)$, a clear step of TCμ can be observed at 108K.
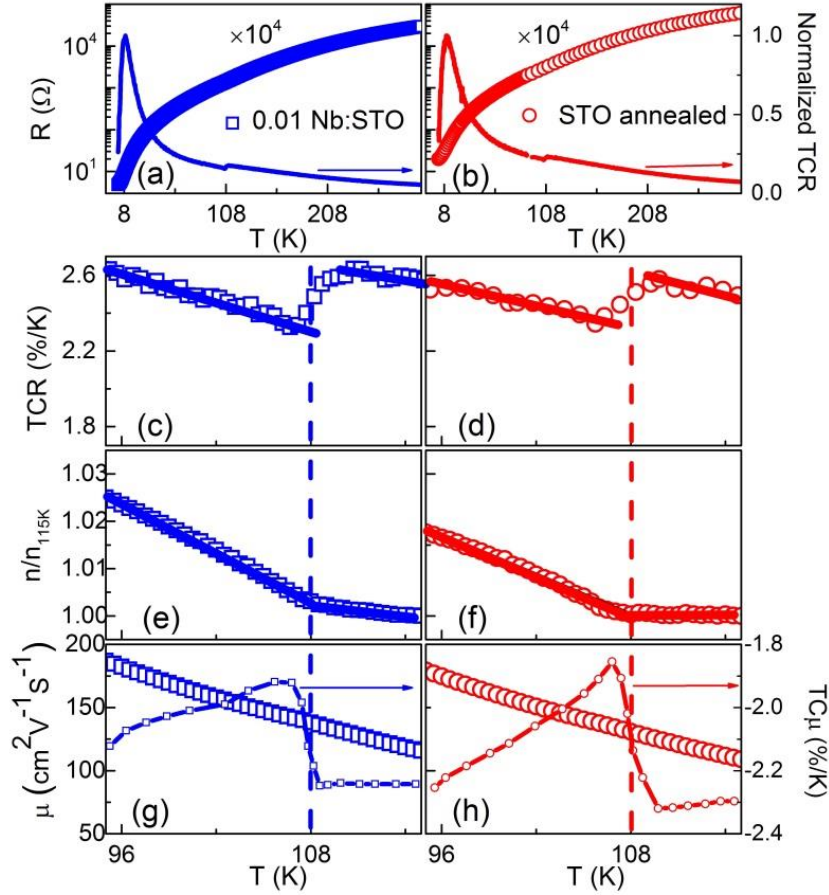
Figure 3.1 Electronic transport anomaly of 3DEL at T_c. (a)-(b): (left scale)
Temperature dependence of resistance for 0.01 wt% Nb:STO and high
vacuum, 1h annealed STO single crystal, respectively. The resistance in (a)
and (b) is multiplied by a factor of 10^4. (right scale) Temperature dependence
of TCR, which is normalized by its main peak for each sample for better
visibility. (c)-(d): Temperature dependence of TCR over the temperature range
95-115 K for the same samples in (a)-(b). (e)-(f): Temperature dependence of
n/n_{115K} over the temperature range 95-115K, n is divided by n_{115K} for each
sample for better comparison. The straight lines in (c)-(f) are guides for the
eyes. (g)-(h): Temperature dependence of carrier mobility μ (left scale) and
TCμ (right scale).

3.3.2 Two-dimensional electron liquid

Since the discovery of a high-mobility two dimensional electron liquid (2DEL) at LAO/STO interface by Ohtomo and Hwang in 2004, this interface has attracted a lot of attentions [57]. Over the past decade, 2DEL has been observed in a wide variety of oxide heterostructures, such as LSAT/STO [136], Al_2O_3/STO [137] and $LaTiO_3$/STO [138]. In all these heterostructures, STO is almost exclusively selected as the substrate. The 2DEL in these heterostructures lies in STO within a few nanometers from the interface [139-141]. With this background in mind, one would thus expect similar electronic transport anomaly in STO-based 2DEL if the anomaly is originated from the phase transition of STO.

To check the electronic transport anomaly in 2DEL, we studied two heterostructures, i.e. LAO/STO and LSAT/STO. Figure 3.2 shows electronic transport properties of a 10 uc LAO/STO and a 10 uc LSAT/STO sample. One can see that the transport properties of the 2DEL shown in Fig. 3.2 closely resemble those of the 3DEL shown in Fig. 3.1. The same TCR peak, carrier density anomaly and TCμ anomaly at 108 K in Fig. 3.1 can be observed in Fig. 3.2. Although the quantities may differ from sample to sample, the behavior is qualitatively the same for all the samples, regardless of the origin of the carrier or the dimension of the electron liquid. We note that, similar to the 3DEL, the absolute change of the two-dimensional carrier density over the temperature range 95-115 K is also quite small. For the 10 uc LAO/STO sample, n is 3.010×10^{13} and 2.910×10^{13} cm^{-2} at 95 and 115 K, respectively. For the 10 uc LSAT/STO sample, n is 2.064×10^{13} and 2.018×10^{13} cm^{-3} at 95 and 115 K, respectively.
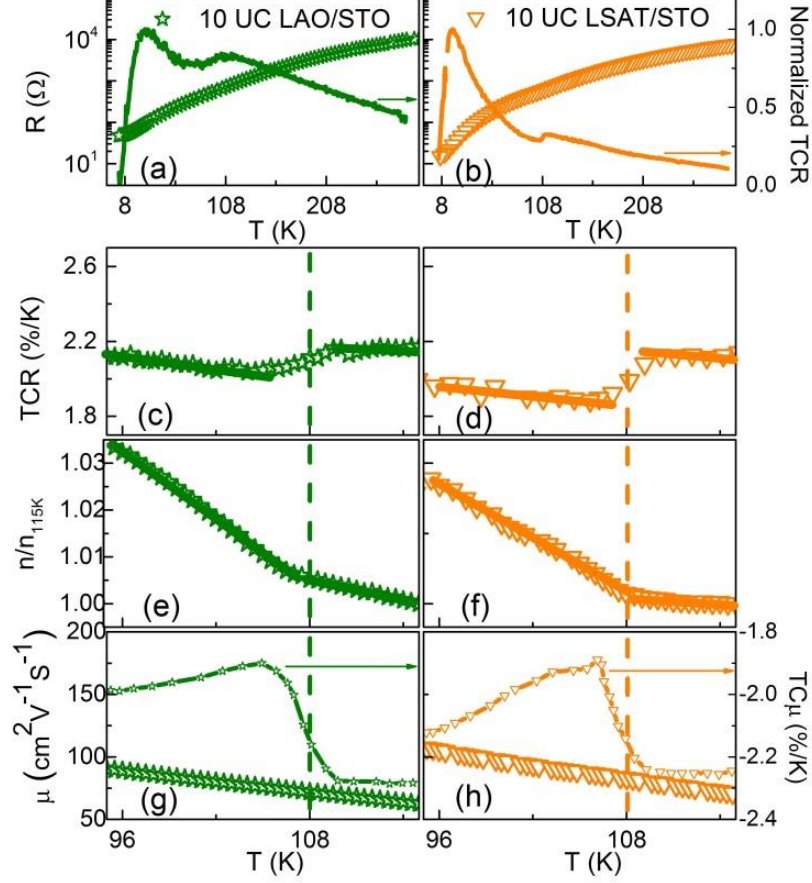
Figure 3.2 Electronic transport anomaly of 2DEL at T_c. (a)-(b): (left scale) Temperature dependence of resistance for 10uc LAO/STO and 10uc LSAT/STO, respectively. (right scale) Temperature dependence of TCR, which is normalized by its main peak for each sample for better visibility. (c)-(d): Temperature dependence of TCR over the temperature range 95-115K for the same samples in (a)-(b). (e)-(f): Temperature dependence of n/n_{115K} over the temperature range 95-115K, n is divided by n_{115K} for each sample for better comparison. The straight lines in (c)-(f) are guides for the eyes. (g)-(h): Temperature dependence of carrier mobility μ (left scale) and TCµ (right scale).

As discussed in section 3.2, the LAO/STO (001) and LSAT/STO (001) samples shown in Fig. 3.2 were post-annealed in air after the deposition to compensate the oxygen vacancies. We further found that the electronic transport anomaly is also present in as-grown samples, *i.e.* it is independent of this post-annealing process. Generally, the 2DEL in post-annealed LAO/STO (001) heterostructure is believed to come from polar discontinuity solely, while the 2DEL in as-grown LAO/STO (001) heterostructure originates from

both polar discontinuity and oxygen vacancies [30]. Figure 3.3 shows the electronic transport properties of an as-grown 10 uc LAO/STO (001) sample. Similar TCR and TCµ behaviour to that of post-annealed LAO/STO sample can be observed. However, by comparing Fig. 3.2(e) and Fig. 3.3(b), one can see that the *n-T* curves show different behaviour for the two samples. The carrier density of the post-annealed sample increases with decreasing temperature, which is attributed to the enhancement of dielectric constant of STO with lower temperature [135]. The carrier density of the as-grown sample, on the contrary, decreases with decreasing temperature, which is attributed to the freeze-out of oxygen-vacancy-induced carriers with lower temperature [127]. Nevertheless, if one defines temperature coefficient of carrier density as TCn= TCR= $(1/n)(dn/dT)$, a clear step can be observed at 108 K, as shown in Fig. 3.3 (b) (right scale). These results indicate that the anomaly at 108 K is independent of the origin of the 2DEL.
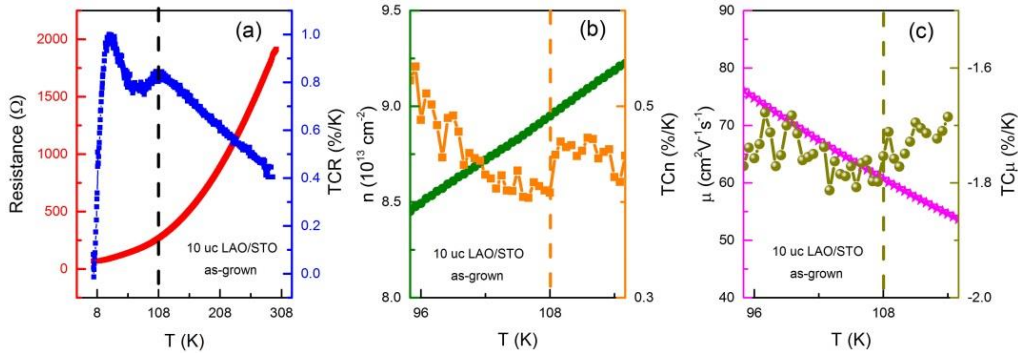
Figure 3.3 Electronic transport anomaly of an as-grown 10 uc LAO/STO sample. (left scale) Temperature dependent resistance (a), carrier density (b) and mobility (c). (right scale) Temperature dependent TCR (a), TCn (b) and TCµ.

Apart from LAO/STO (001) heterostructure, we note that the 2DEL in LAO/STO (110) also shows anomaly at 108 K, as shown in Fig. 3.4. The sheet resistance of the LAO/STO (110) sample is anisotropic along the two in-plane

directions , which can be explained by a buckling model in Ref. [142]. Both the TCR along ($1\bar{1}0$) and (001) directions show an anomaly at 108 K, as shown in Fig. 3.4 (b). These results indicate that the anomaly at 108 K is independent of crystalline direction of the STO substrate.
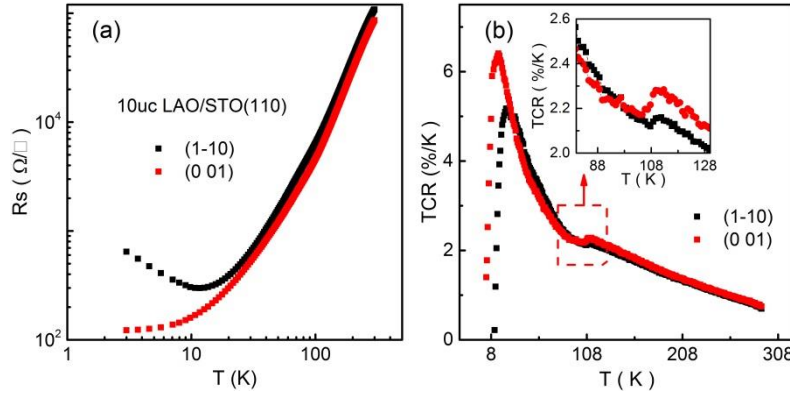
Figure 3.4 Temperature dependence of sheet resistance (a) and TCR (b) for a 10uc LAO/STO(110) sample along two different measurement directions: (1-10) and (001). The inset in (b) shows an enlarged view for TCR over the range 80-130K.

3.3.3 Fermi liquid behaviour of *n*-type SrTiO₃ at low temperature

In the low temperature region (<100 K), the conduction mechanism in *n*-type STO can be well described by the Fermi liquid theory [27]. As mentioned in Section 3.3.1, the resistance of a Fermi liquid can be expressed as $R=AT^2+R_0$, where A is a constant and R_0 is residual resistance. By applying the Fermi liquid theory, the main peak in all the temperature dependent TCR curves can be well fitted. In Fig. 3.5 (a)-(b), we show the fitting of a 0.05wt% NST sample and a 10uc LAO/STO sample as an example for 3D and 2D electron liquid, respectively. The fitting curves are obtained by fitting the resistivity at low temperature (2-100 K) with $\rho=AT^2+\rho_0$, then the red solid lines are obtained by calculating the fitted data with $(TCR)_{\text{fitting}} =(1/\rho)(d\rho/dT)$. One can

see that the fitting curves match well with the experimental data at low temperature.

Furthermore, as shown in Table 1, ρ_0 and A are obtained for NST samples with different doping concentrations to calculate the position of the first peak with $T_1=(\rho_0/A)^{1/2}$. The fitted peak position T_1 is in good agreement with the experimental peak position $T_1{}'$. In addition, The extracted ρ_0 and A values are in good agreement with that reported by Lin $et~al.$[27].
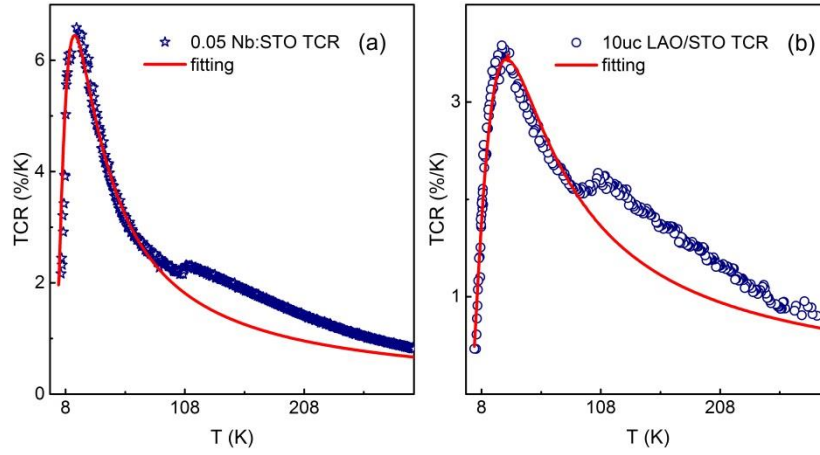
Figure 3.5 (a) and (b) Fitting of the first TCR peak for 0.05wt% NST and 10uc LAO/STO, respectively.

Nb (wt.%)	ρ_0 ($\mu\Omega\bullet$cm)	A ($\mu\Omega\bullet$cm$\bullet$K^{-2})	$T_1=(\rho_0/A)^{1/2}$ (K)	$T_1{}'$ (K)
0.01	79.3	2.02	6.3	9.2
0.05	75.3	0.31	15.5	15.7
0.1	54.6	0.18	17.6	18.7
0.5	48.6	0.03	43.0	39.2

Table 1 Extracted ρ_0, A and T_1 from the fitted data for NST samples with different doping concentration. $T_1{}'$ is the experimental position of the first peak. One can see that T_1 and $T_1{}'$ agree well with each other.

3.3.4 Electron-soft phonon scattering at T_c

As explained in **Section 1.2.1**, the phase transition of STO can be described by the zone corner Γ_{25} (111) soft phonon. We attribute the observed transport

anomaly at 108 K to electron scattering by this soft phonon in STO around its phase transition temperature. This electron-soft phonon scattering has been used to explain the superconductivity in STO by J. Appel [143].

We fit the temperature dependent resistivity (ρ–T) curve of a 0.01wt% NST sample above and below 108 K separately as indicated by the red solid line in Fig. 3.6 (a) due to the discontinuity of dρ/dT at 108 K (inset). This is also supported by the results in Fig. 3.1. The low temperature (2-90 K) ρ is fitted with $\rho_1 = A_1 T^2 + \rho_{01}$, while the high temperature (120-300 K) ρ is fitted with $\rho_2 = A_2 T^m + \rho_{02}$, where A_1, A_2 and m are constants, ρ_{01} and ρ_{02} are high and low temperature residual resistivity, respectively. A peak at T_c in $\Delta\rho$ can be observed after subtracting the fitted background from the experimental ρ–T curve (Fig. 3.6 (c)).

Figure 3.6 (b) shows the zone corner Γ_{25} (111) soft phonon energy dependence on temperature as reprinted from Ref. [16]. It softens from high temperature to T_c and splits into two branches (E_g and A_{1g}) below T_c as the symmetry is lowered from cubic to tetragonal phase. This symmetry breaking doubles the unit cell from cubic to tetragonal phase and consequently the Brillouin zone corner Γ_{25} (111) phonon is folded onto the zone center of the tetragonal phase [16, 17]. The softening of the Γ_{25} phonon leads to a divergence in mode occupation as phonons obey Bose-Einstein distribution [144]. The red dashed line in Fig. 3.6 (c) (upper panel) is the fitting of $\Delta\rho$ with the electron-soft phonon interaction by using the method in Ref. [144]. The fitting function is $\Delta\rho = c \times N$, where N is the Γ_{25} phonon's Bose-Einstein occupation number evaluated using the phonon energies in Fig. 3.6 (b), c is a conversion factor

from N to resistivity. We note that c could be different for high and low temperature region as the wave-vector of the soft phonon changes from $q=\sqrt{3}\pi/a$ to $q=0$ at T_c. The TCR anomaly can also be fitted satisfactorily as shown in the lower panel of Fig. 3.6 (c). Apart from NST, the transport anomaly in SrTiO$_{3-\delta}$, LAO/STO (001), LSAT/STO (001), LAO/STO (110) can also be fitted by using the same method. We show the experimental and fitted data of LAO/STO in Fig. 3.6 (d) as an example for 2DEL.

It should be noted that $|\mathrm{d}n/\mathrm{d}T|$ shows a sudden increase at T_c from high to low temperature, while $|\mathrm{d}\mu/\mathrm{d}T|$ shows a decrease at T_c (Fig. 3.1). As $\sigma=1/\rho=ne\mu$, where σ is conductivity and e is the elementary charge, the anomaly of $|\mathrm{d}n/\mathrm{d}T|$ and $|\mathrm{d}\mu/\mathrm{d}T|$ thus contribute oppositely to the anomaly of $\mathrm{d}\rho/\mathrm{d}T$. As $\mathrm{d}\rho/\mathrm{d}T$ shows a decrease at T_c (Fig. 3.6), the anomaly in $\mathrm{d}\rho/\mathrm{d}T$ and thus in TCR is dominated by $|\mathrm{d}\mu/\mathrm{d}T|$ over $|\mathrm{d}n/\mathrm{d}T|$.
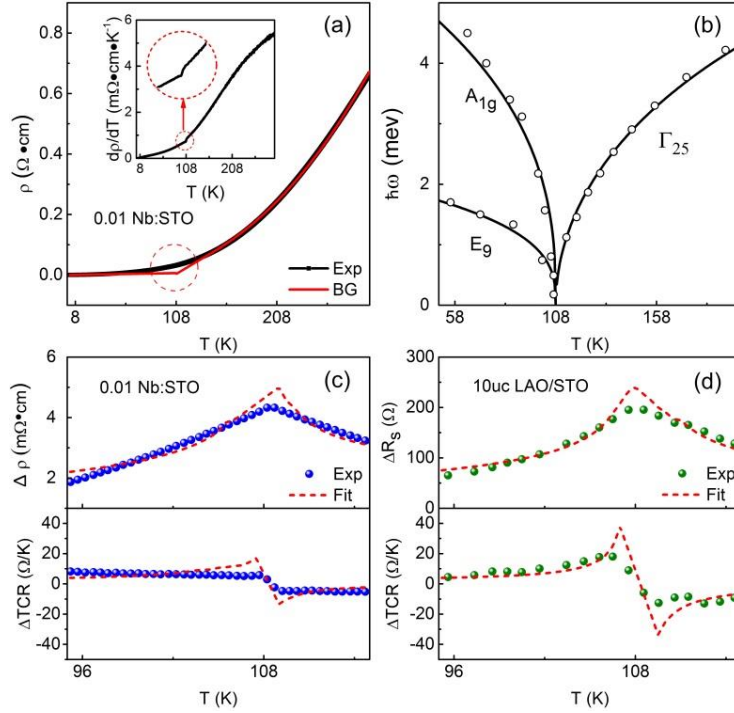
Figure 3.6 Electron-soft phonon scattering at T_c. (a) Temperature dependence of resistivity for a 0.01wt% Nb:STO sample. Solid red line is the background fitted in the low (2-90 K) and high temperature (120-300 K) region. Inset shows temperature dependence of $d\rho/dT$, a drop at 108 K can be seen, as magnified in the red dashed circle. This drop in $d\rho/dT$ at T_c separates the conducting mechanism of STO-based systems into two regimes. (b) Energy dependence on temperature for the Γ_{25} (111) soft phonon, which softens at T_c and splits into two phonon modes below T_c (after Ref. [20]) (c)–(d) Electron-soft phonon scattering fitting for 0.01wt% Nb:STO and 10uc LAO/STO, respectively. (upper panel) Fitting of $\Delta\rho(\Delta R_s)$, which is extracted by subtracting the background from the experimental $\rho(R_s)$ as shown in (a). (lower panel) Fitting of ΔTCR, which is calculated from $\Delta\rho(\Delta R_s)$.

3.4 First-principles calculations

To gain further insights into the relation between the phase transition and transport anomaly in STO-based systems, we perform first-principles band structure calculations for both bulk STO and LAO/STO heterostructure (Fig. 3.7 (a) and (b)) using density-functional theory based Vienna ab initio Simulation Package (VASP) [145, 146]. The Perdew-Burke-Ernzerhof (PBE) approximation for the exchange-correlation functional and the frozen-core all-electron projector-augmented wave (PAW) method are applied here [147, 148].

For bulk STO calculations, the cutoff energy for the plane wave expansion is set to 500 eV. To allow the rotation of the TiO_6 octahedron in tetragonal STO, a minimum supercell containing 20 atoms is required. A similar supercell is used for STO in cubic phase to make a direct comparison. Monkhorst-Pack k-point grids for Brillouin zone sampling are set to 6×6×6 for bulk STO within both cubic and tetragonal phase. The structures are fully relaxed until the forces are smaller than 0.001 eV/Å. The calculated tetragonal STO has an equilibrium structure with $a = b = 3.936$ Å, $c/a = 1.005$, and a rotational angle of 5.09^o for the TiO_6 octahedron along the z axis, while $a = b = c = 3.948$ Å for cubic STO. These parameters are in good agreement with previous reports

[17, 149]. For the LAO/STO heterostructure calculations, LAO is grown on both cubic and tetragonal STO. Superlattice structures with fixed in-plane lattice constant of SrTiO$_3$ are used, the k-meshes are set to 6×6×1, and the forces are considered as convergent if smaller than 0.01 eV/Å.

Figures 3.6 (c)-(d) show top and side view of the LAO/STO supercell in the tetragonal phase used in the calculations. The "antiferrodisplacive" phase transition is introduced by the opposite rotations of the nearest oxygen octahedrons around c axis.

In the case of bulk STO, the conduction band minimum lies at Γ point of the Brillouin zone and is consisted of triply degenerate t_{2g} bands in the cubic phase. Upon phase transition at T_c, the tetragonal crystal field splits the t_{2g} bands into a lower d_{yz} and d_{zx} doublet and a higher d_{xy} band with ΔE≈13 meV. It should be noted that besides the band splitting, the curvature of each band is also changed, which leads to a change in effective mass. All the bands in tetragonal phase have larger effective mass than that in the cubic phase. For the lowest d_{yz} band, in the cubic phase, m_x^*=6.22m_e, m_y^*=0.41m_e, while in the tetragonal phase, m_x^*=11.49m_e, m_y^*=0.70m_e, thus m^*=2 $m_x^* m_y^*/(m_x^*+m_y^*)$ increases from 0.77m_e to 1.32m_e.

For LAO/STO heterostructure, the conduction band minimum also lies at Γ point. However, compared to bulk STO, in the cubic phase, the triply degenerate t_{2g} bands are split into a lower d_{xy} band and an upper d_{yz}, d_{zx} doublet by the interface crystal field [139]. Two features can be observed in the tetragonal phase of LAO/STO heterostructure as compared to its cubic phase. First, the curvature of each band is changed as also observed in bulk

STO, and m^* increases from $0.48m_e$ to $0.53m_e$ for the lowest d_{xy} band. Second, the bandwidth is decreased, the energy difference between the lowest two d_{xy} bands decreases from 0.15 to 0.12 eV. These results indicate that the conduction electrons in the tetragonal phase have a smaller mobility than in the cubic phase, as μ is inversely proportional to m^*. However, experimentally, the mobility of the electrons increases monotonically from 300 to 2K without any observable anomaly. As discussed earlier, the electron mobility in STO is either explained by TO zone centre phonon scattering [23] or LO phonon scattering [29], and the exact origin is still in debate. However, no matter what the underlying scattering mechanism is, it serves as a large background for μ-T for the weak electron-soft phonon scattering. This explains why the μ-T curve is smooth, while a clear anomaly is observed in TCμ.
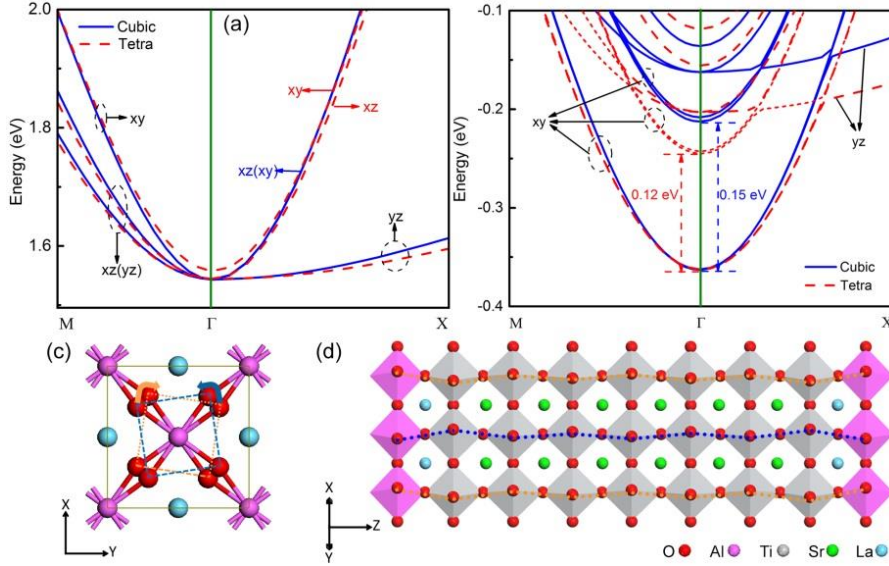
Figure 3.7 Band structure calculations. (a)-(b) Conduction band of cubic (blue solid line) and tetragonal (red dashed line) phase for STO and LAO/STO, respectively. We note that the band structures shown here are zoomed in for clarity. The M and X points denote the directions along which the K points are scattered. (c)-(d) Top and side view of the LAO/STO supercell used in the calculations, respectively. The dashed lines in (c) and (d) are guides to the eyes, showing opposite rotation directions for the nearest oxygen octahedrons around z axis.

In summary, our calculations indicate that both the 3DEL and 2DEL in STO show a small decrease in carrier mobility from cubic to tetragonal phase, due to enhancement of effective mass of the electrons. This band structure change is responsible for the TCμ anomaly at 108 K.

3.5 Carrier density dependence of the magnitude of the anomaly

Measurements on a series of NST samples with different doping concentrations show that the magnitude of the anomaly decreases with increasing carrier density as shown in Fig. 3.8. We define the magnitude of the anomaly as $|\Delta TCR|=|(TCR)_{108K}^{+}-(TCR)_{108K}^{-}|$. $|\Delta TCR|$ decreases approximately three times from around 0.3% to 0.1% as carrier density increases from 10^{18} to 2×10^{20} cm^{-3} (Fig. 3.8 (d)). $|\Delta TC\mu|$ and $|\Delta TCn|$ also decrease with increasing carrier density. Here, TCn is defined as TCn=$(1/n)(dn/dT)$. $|\Delta TC\mu|$ and $|\Delta TCn|$ are defined similarly to $|\Delta TCR|$, i.e. $|\Delta TC\mu|=|(TC\mu)_{108K}^{+}-(TC\mu)_{108K}^{-}|$ and $|\Delta TCn|=|(TCn)_{108K}^{+}-(TCn)_{108K}^{-}|$.

In Fig. 3.9, we show details of the extraction of $|\Delta TCR|$, $|\Delta TC\mu|$ and $|\Delta TCn|$ of a 0.01 wt% NST sample. The high temperature region (108-120 K) and low temperature region (95-108 K) experimental values were fitted separately with linear functions. The magnitude of the anomaly is then defined as the absolute difference of the two linear functions at 108 K.

It should be noted that the TCn anomaly can also be clearly seen in Fig. 3.8 (b). For the most doped sample, the carrier density shows a linear dependence on temperature. As carrier density decreases, the slope change at T_c increases.

The total resistance of STO-based systems is consisted of different scattering mechanisms including Baber scattering, direct electron-phonon scattering, umklapp electron-electron scattering and impurity scattering [25]. To fully account for the small magnitude of the anomaly at T_c would require careful theoretical treatments of all the phonon branches and electrons from different bands, which is beyond the scope of this work. We simplify this problem by considering the bulk STO case in the tetragonal phase, where only Baber electron-electron scattering (R_{e-e}) and electron-soft phonon (R_{e-sp}) scattering are active and the total resistance can be expressed as $R_{tot} = R_{e-e} + R_{e-sp}$. $|\Delta TCR|$ is then proportional to R_{e-sp}/R_{e-e}. We compare the two extreme cases of small carrier density (only the lowest d_{yz} and d_{xz} doublet is occupied) and large carrier density (all the t_{2g} bands are occupied) states, hereafter noted as n_s and n_l state, respectively. In the tetragonal phase, for the d_{xy} bands, $m_1{}^* = 0.41 m_e$, for d_{yz} and d_{xz} bands $m_2{}^* = 1.32 m_e$. In a simplified two-band structure, the strength of the Baber scattering is proportional to $(m_2{}^*/m_1{}^*)^2$, where $m_1{}^*$ and $m_2{}^*$ is effective mass of the light and heavy band, respectively [28]. The strength of the Baber scattering of n_l state is then $(1.32/0.41)^2 \approx 10$ times larger than that of the n_s state. If we assume that the electron-soft phonon scattering does not depend on the details of the energy bands, then R_{e-sp}/R_{e-e} of the n_l state is 10 times smaller than that of the n_s state. According to quantum oscillation measurements in STO, for $n < 10^{18}$ cm^{-3}, the ground state is single band; for $n > 2 \times 10^{19}$ cm^{-3} three bands are occupied [27]. The 0.01wt% ($n \approx 10^{18}$ cm^{-3}) and 0.5wt% NST ($n \approx 2 \times 10^{20}$ cm^{-3}) then correspond to a single-band n_s state and a three-band n_l state, respectively. The corresponding R_{e-sp}/R_{e-e} is thus expected to decrease by 10 times from 0.01wt% to 0.05wt% NST.

Experimentally, |ΔTCR| decreases by ~3 times from 0.01wt% to 0.5wt% NST. Thus both R_{e-sp}/R_{e-e} and |ΔTCR| decrease with increasing carrier density. Similarly, in the case of LAO/STO, as reported by Delugas $et\ al.$, m_1^*=0.7 m_e, m_2^*=1.3m_e, so the strength of the Baber scattering in the n_l state is 3.4 times larger than that of the n_s state [139].

Apart from NST, we also found that, in SrTiO$_{3-\delta}$, the magnitude of the anomaly also decreases with increasing carrier density. In Fig. 3.10, we show the carrier density dependence on temperature for a series of SrTiO$_{3-\delta}$ samples, which were annealed at 800 ℃ in 10^{-7} torr vacuum for 1, 2 and 4 h, respectively. The carrier density of these samples at 100 K are 6.2×10^{16}, 8.6×10^{17} and 1.2×10^{18} cm^{-3}, respectively. One can clearly see that the carrier density anomaly increases with decreasing carrier density.

In summary, the decreasing TCR magnitude with increasing carrier density can be qualitatively explained as follows: when carrier density of the electron liquid increases, more conduction bands will be occupied, the scattering mechanism is then dominated by the Baber electron-electron scattering between different conduction bands and the proportion of the electron-soft phonon scattering in the total resistance decreases, the conduction electrons tends to follow the T^2 Fermi liquid behaviour better.
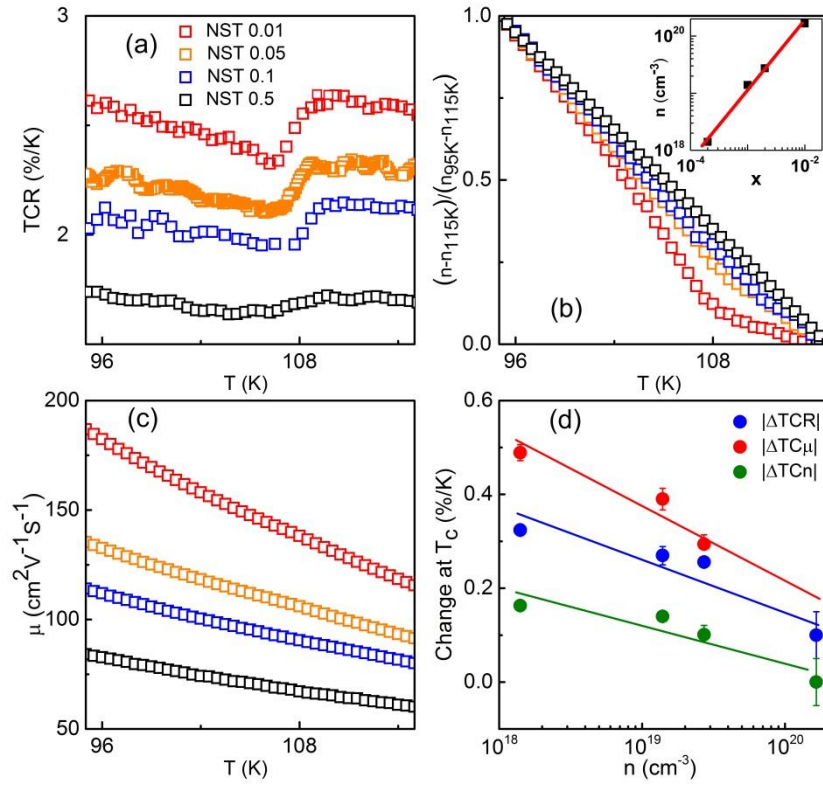
Figure 3.8 Carrier density dependence of the magnitude of the anomaly for NST. (a)-(c) Temperature dependence of TCR, $(n-n_{115K})/(n_{95K}-n_{115K})$ and mobility for 0.01, 0.05, 0.1 and 0.5 wt.% NST, respectively. Here, n is normalized by $(n-n_{115K})/(n_{95K}-n_{115K})$ to simplify comparison. The inset in (b) shows carrier density for the four $SrTi_{1-x}Nb_xO_3$ samples. (d) Carrier density dependence of the magnitude of the anomaly for $|\Delta TCR|$, $|\Delta TC\mu|$ and $|\Delta TCn|$. Here, $|\Delta TCR|$ is defined as $|\Delta TCR|=|(TCR)_{108K}^+-(TCR)_{108K}^-|$, $|\Delta TC\mu|$ and $|\Delta TCn|$ are defined similarly.
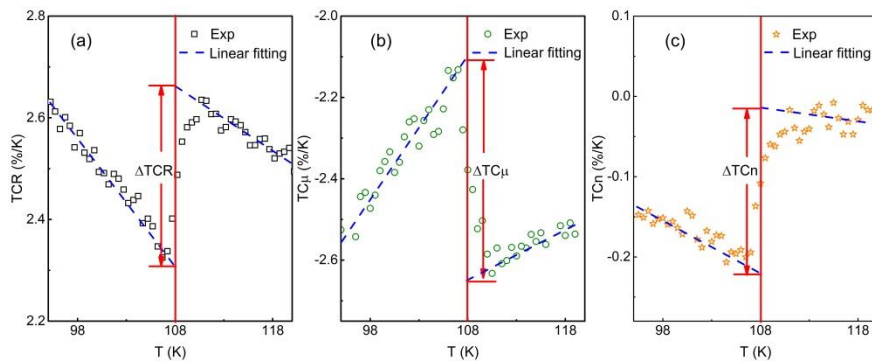
Figure 3.9 Temperature dependence of TCR (a), TCμ (b) and TCn (c) for a 0.01wt% NST sample. Blue dashed lines are linear fittings of the experimental data in high temperature (108-120 K) and low temperature (95-108 K) regions.
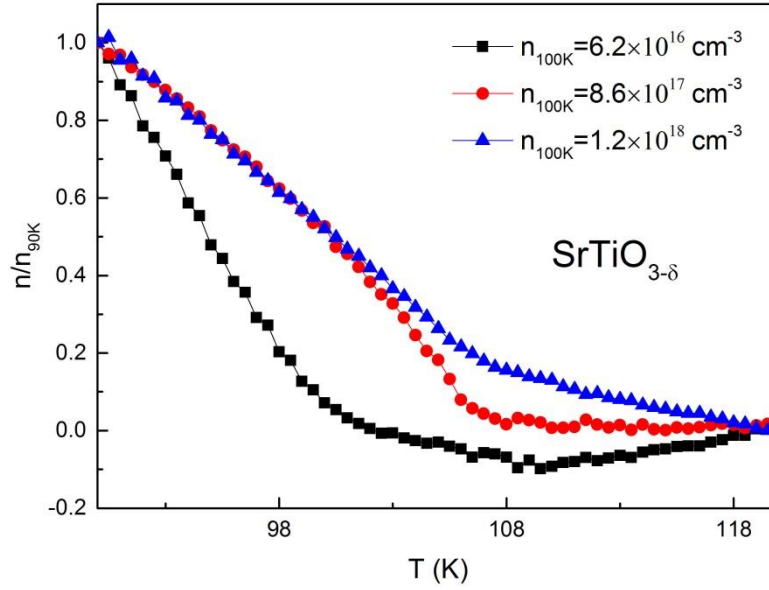
Figure 3.10 Temperature dependence of carrier density for a series of SrTiO$_{3-\delta}$ samples. The black square, red circle and blue triangle stand for samples annealed at 800 ℃ in 10^{-7} torr vacuum for 1, 2 and 4 h, respectively. The carrier density of each sample at 100 K (n_{100K}) is used to represent the sample. The longer is the annealing time, the larger is the carrier density. Carrier densities for these samples are normalized by n/n_{90K} to simplify comparison.

3.6 Suppression of TCR anomaly

As discussed above, the TCR anomaly in STO-based systems is attributed to the cubic-to-tetragonal phase transition of STO at T_c. One question one may ask is that: can the TCR anomaly be suppressed if the phase transition of STO is suppressed?

With this question in mind, we prepared epitaxial LAO/STO heterostructure on LSAT (001) and NGO (110) substrates. As compared to conventional LAO/STO heterostructure, which ultilizes STO as the substrate, epitaxial LAO/STO heterostructure may find its applications in high frequency devices [62]. The epitaxial strain exposed on LAO/STO by the substrate was utilized to control the carrier density and mobility of the 2DEL [97]. In addition, the epitaxial strain also suppresses the phase transition of LAO and STO due to substrate clamping effect [150].

Figure 3.11 shows temperature dependent TCR for a 15 uc LAO/10 uc STO/LSAT (001) sample and a 15 uc LAO/10 uc STO/NGO (110) sample. The inset shows temperature dependence of sheet resistance (R_s-T) for the two samples. Both R_s-T curves show metallic behavior from 300 K to around 100 K and an weak localization upturn below 100 K. The upturn in R_s-T curve around 100 K is attributed to weak localization due to disorder, misfit strain and point defects [62, 151]. From the fact that STO directly grown on LSAT and NGO is insulating, it can be concluded that the observed 2DEL resides at LAO/STO interface. Unlike the results shown in Fig. 3.1, the temperature dependent TCR curves for both samples are smooth without any observable anomaly over the whole temperature range. We believe that this is caused by the substrate clamping effect [150], which suppresses the phase transition of STO thin film when grown on other substrates. The absence of TCR anomaly at 108 K in epitaxial LAO/STO heterostructure further suggests that the TCR anomaly is caused by the phase transition of STO.
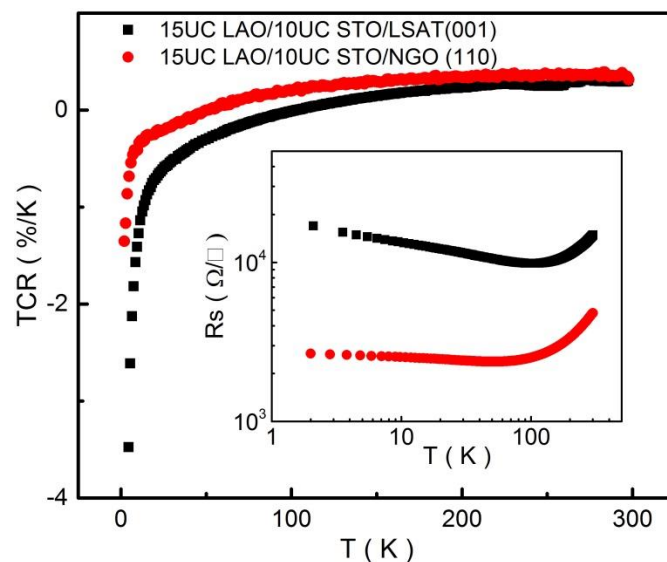
Figure 3.11 Temperature dependence of TCR for a 15 uc LAO/10 uc STO/LSAT (001) sample and a 15 uc LAO/10 uc STO/NGO (110) sample. The inset shows temperature dependence of sheet resistance for the two samples.

3.7 Summary

In conclusion, by using detailed electronic transport measurements, we have revealed the long-sought phase transition induced anomaly in resistivity, carrier density and mobility at T_c in a wide variety of STO-based systems. From the fact that the anomaly is independent of the dimension of the electron liquid (3D or 2D), the origin of the electron liquid (chemical doping or polar catastrophe), the over-layer of the 2DEL (LAO or LSAT) and the crystalline orientation of STO (($1\bar{1}0$) or (001)), we believe that the anomaly is intrinsic to STO-based systems. The suppression of TCR anomaly in epitaxial LAO/STO heterostructures deposited on LSAT and NGO substrates gives further evidence of the correlation between the transport anomaly and the phase transition of STO.

The TCR anomaly around T_c can be well fitted with the electron-Γ_{25} soft phonon scattering. In addition, the TCR anomaly is caused by anomalies in both carrier density and mobility with the latter taking the dominant role. First-principles calculations for both STO bulk and LAO/STO heterostructure show that the mobility anomaly is caused by the electron effective mass enhancement from cubic to tetragonal phase transition. Furthermore, the magnitude of the anomaly decreases with increasing carrier density as a result of competing electron-electron scattering and electron-soft phonon scattering. Although the Γ_{25} soft phonon has been rendered to have no contribution to electron-phonon scattering due to its long wave vector, here we have shown that the electron- Γ_{25} soft phonon scattering has a small but non-trivial effect on the electronic transport properties.

These results may provide new insights about the electronic transport properties, electron-electron scattering, electron-phonon scattering and superconductivity in STO. In addition, as STO is a prototype of the so-called strongly correlated system, the methods reported here may be applied to other strongly correlated materials as well.

Author contributions:

W. X. Zhou and Ariando designed the experiment. W. X. Zhou prepared the samples and performed the electronic transport measurements. J. Zhou conducted the DFT calculations. W. X. Zhou, C. J. Li, Z. Huang, J. Zhou and Ariando analyzed the data. S. W. Zeng, H. J. Harsan Ma, K. Han, Z. S. Lim, D. Y. Wan, L. C. Zhang, T. Venkatesan and Y. P. Feng joined the discussion.

Chapter 4 Coexistence of ferroelectricity and two-dimensional electron gas in LaAlO$_3$/Ba$_x$Sr$_{1-x}$TiO$_3$ heterostructures

Abstract

Ferroelectricity is determined by the delicate balance between long-range Coulomb forces favoring the ferroelectric state and short-range repulsions favoring the paraelectric state. It disappears when the long-range Coulomb forces are suppressed in reduced dimension or screened by itinerant electrons. Here, we explore the possible persistence of ferroelectricity in reduced dimension with itinerant electrons. Our piezoresponse force microscopy, electrical and optical measurements, as well as first-principles calculations, demonstrate the coexistence of ferroelectricity and two-dimensional electron gas in Ba$_x$Sr$_{1-x}$TiO$_3$ thin film of 4 nm thick.

4.1 Motivation

The strong correlation and delicate balance between spin, orbit, charge and lattice in complex oxides serves as a fertile ground to search for multi-functionality, i.e., the coexistence of distinct physical properties, especially the seemingly incompatible ones [8, 45]. One example is the coexistence of ferromagnetism and superconductivity at LaAlO$_3$/SrTiO$_3$ (LAO/STO) interface [57, 67]. Another example is the coexistence of ferromagnetism and ferroelectricity in FeTiO$_3$ [152]. Recently, the coexistence of ferroelectricity and conductivity has attracted considerable attentions [43, 45, 153-155].

As introduced in **section 1.2.2**, in ferroelectrics, the long-range Coulomb forces (which favor the ferroelectric state) compete with the short-range repulsions (which favor the paraelectric state) [41-43]. When the former prevails over the latter, the ferroelectric state is stable, leading to a

spontaneous polarization. The spontaneous polarization is associated with a small displacement between the anions and cations. However, when the latter dominates, the system becomes paraelectric [42]. In this scenario, one question one can ask is that: how long is the corresponding range, in which the ferroelectric state is more stable than the paraelectric state [43, 156] ? In the scientific society, the answer to this question has been changing over time.

Generally, ferroelectricity is considered as a collective phenomenon. It is expected to diminish with reduced dimension. Finally, when the film thickness is below a "critical thickness" (t_c), ferroelectricity disappears [156, 157]. In the 1990s, this t_c has been estimated to be approximately 10 nm [156]. Later, ferroelectricity was found in 4 nm thin films [158]. Most recently, stable ferroelectric state has even been observed in films as thin as 0.8-1.2 nm [159, 160].

In addition to reduced dimension, ferroelectricity can also be eliminated by itinerant electrons. This is realized by screening the long-rang Coulomb forces with itinerant electrons [43, 45]. However, several ferroelectric metals have recently been realized experimentally, for example, $Cd_2Re_2O_7$, $LiOsO_3$ and $BaTiO_{3-\delta}$ (BTO) [43, 45, 153-155]. Theoretically, first-principles calculations have pointed out that the "long-range" Coulomb forces only require a range as short as ~ 0.5 nm to preserve stable ferroelectricity.

The above conclusions have significantly deepened our understanding of the range of the Coulomb forces. This in turn enables us to stabilize ferroelectricity under previously inaccessible conditions, and thus, providing more opportunities to the research society as well as industry.

In this chapter, we try to combine the two effects mentioned above, i.e. reduced dimension and itinerant electrons. We thus push the range of the Coulomb forces in ferroelectrics to the extreme by studying the possible coexistence of ferroelectricity and two-dimensional electron gas (2DEG).

With this goal in mind, we first investigated the structure discussed in Fig. 1.20, i.e. LaAlO$_3$/BaTiO$_3$ (LAO/BTO) (001) heterostructure. As discussed in **section 1.4.2**, a 2DEG has been theoretically predicted in BTO, and thus, the LAO/BTO heterostructure may be utilized to study the coexistence of ferroelectricity and 2DEG in BTO. Figure 4.1 (a) shows an atomic force microscopy (AFM) image of a BTO (001) substrate, the surface is smooth with a root-mean-square roughness of 0.11 nm. However, BTO substrate intrinsically has *a*- and *c*-domains. This is evidenced by the piezoresponse force microscopy (PFM) amplitude image of the BTO (001) substrate, as shown in Fig. 4.1 (b). The stripes represent the domains. These domains deteriorate the formation of 2DEG. As discussed earlier in LAO/STO heterostructure, the substrate quality is crucial for the formation of 2DEG. Experimentally, we did not observe 2DEG at LAO/BTO interface.
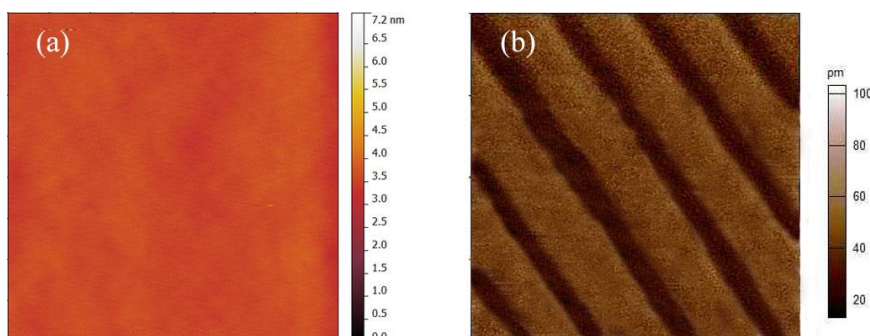
Figure 4.1 AFM (a) and PFM amplitude (b) image of a BTO substrate over the size 4×4 μm^2. The stripes in (b) are *a*- and *c*-domains of BTO.

We next turned our attention to a $LaAlO_3$/$BaTiO_3$/$SrTiO_3$ (LAO/BTO/STO) (001) heterostrucure, where the STO substrate can be controlled to have atomically smooth surface. However, from our first-principles calculations, we found that the charges are transferred from LAO top surface into STO substrate, as shown in Fig. 4.2. In this scenario, the 2DEG (which resides in STO) and ferroelectricity (which comes from BTO) are spatially separated, and thus, this heterostructure is unsuitable for studying the coexistence of ferroelectricity and 2DEG. In addition, experimentally, we did not observe 2DEG in this heterostructure. This is probably because that the ferroelectricity is too strong for the 2DEG to form, as ferroelectricity and 2DEG are two competing properties.
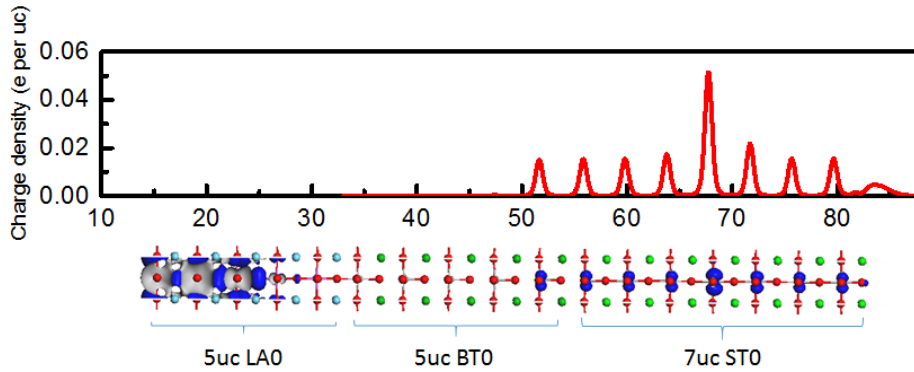
Figure 4.2 First-principles calculations of a LAO/BTO/STO heterostructure. (top panel) Layer-resolved charge density per unit cell. (bottom panel) The supercell used in the calculations.

It is well known that doping Sr in BTO can reduce its ferroelectricity, for example, the magnitude of spontaneous polarization and the Curie temperature [161]. With this in mind, we modified the structure in Fig. 4.2 into $LaAlO_3$/$Ba_xSr_{1-x}TiO_3$/STO (LAO/BST/STO) (001), as shown in Fig. 4.3. In this structure, we found proof for the coexistence of ferroelectricity and 2DEG in ultrathin ferroelectric $Ba_{0.2}Sr_{0.8}TiO_3$ (BST) films. In Ref. [45], the itinerant

93

electrons are doped into ferroelectric BTO by oxygen vacancies. Here, we propose a new mechanism to dope electrons in ferroelectrics, i.e. via electronic reconstruction. Similar to the LAO/STO interface, the LAO/BST interface also has a polar discontinuity. BST has alternating charge-neutral $Sr^{2+}O^{2-}$ (or $Ba^{2+}O^{2-}$) and $Ti^{4+}O_2^{2-}$ sublayers, while LAO has alternating charge positive $(LaO)^+$ and negative $(AlO_2)^-$ sublayers [57, 74]. A 2DEG is expected to form in BST to overcome the polar catastrophe at LAO/BST interface, similar to that of LAO/STO interface.
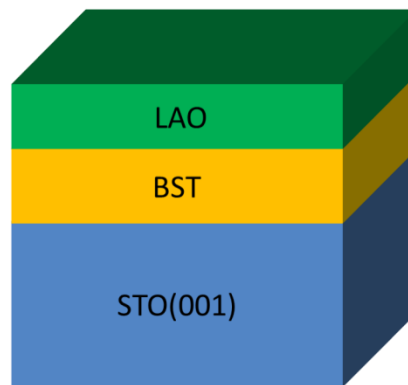
Figure 4.3 Schematic diagram of the LAO/BST/STO (001) heterostructure.

4.2 Experimental methods

All the LAO/BST/STO (001) heterostructures in this chapter were grown by pulsed laser deposition (PLD) equipped with *in-situ* reflection high-energy electron diffraction (RHEED). Prior to the deposition, STO (001) substrates were treated with the method in Section 2.1.1 to obtain atomically sharp surfaces. During the deposition, the temperature and oxygen partial pressure were kept at 760 ℃ and 10^{-4} torr, respectively. BST layer with different thicknesses (0-25 uc) was first deposited on STO substrate. Then, LAO layer with different thicknesses (0-25 uc) was deposited on BST to form the LAO/BST/STO heterostructure. Figures 4.4 (a)-(c) show RHEED patterns for

STO (001) substrate, after BST deposition and after LAO deposition, respectively. The clear Laue circles and Kikuchi lines indicate two-dimensional growth of both BST and LAO. The RHEED oscillations for a 15 uc LAO/25 uc BST/STO sample indicates layer-by-layer growth of both BST and LAO, as shown in Fig. 4.4 (d).
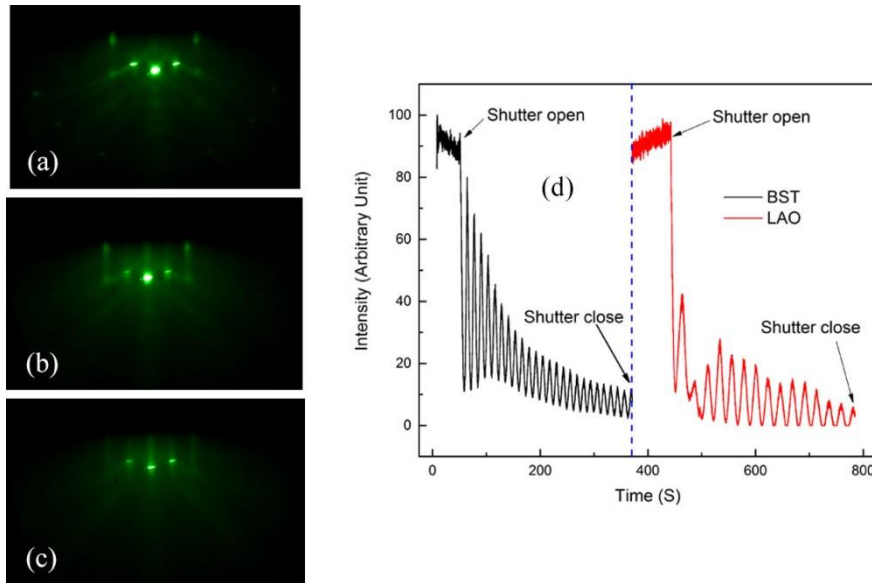
Figure 4.4 (a)-(c) RHEED patterns for STO (001) substrate, after BST deposition and after LAO deposition, respectively. (d) RHEED oscillations for a 15 uc LAO/25 uc BST/STO sample.

A sample with 10 unit cells (uc) of BST on Nb:SrTiO$_3$ (NST) (001) (0.1 wt% Nb doped) substrate was prepared for ferroelectric measurements of the BST thin film. Here, NST was used as a bottom electrode. Ferroelectric properties were measured using piezoresponse force microscope (PFM) and piezoresponse force spectroscopy (PFS) techniques. In this study, a commercial SPM system (MFP-3D, Asylum Research 13.03.70, USA) was used, which was controlled by a commercial software (IGOR PRO 6.34A). In the PFM measurements, amplitude (A) and phase (ϕ) images can be obtained simultaneously by applying an AC bias to the tip. The amplitude image refers

to piezoresponse of the material, whereas the phase image refers to the polarization direction of the material. In the Piezoresponse Force Spectroscopy (PFS) measurement, i.e., the PFM was operated in the spectroscopy mode, the tip with a triangle-square waveform was fixed at a certain location. The frequency of the used waveform was 200 mHz, i.e., the bias-on and bias-off time was 25 ms. To exclude the electrostatic effect, the used phase hysteresis loops, $\phi(E)$ and amplitude loops $A(E)$ here were obtained at bias-off state. In all the measurements, the scan rate was 1 Hz and the bottom electrode of the sample was grounded. A commercial Pt-coated Si tip (AC240TM, Olympus, Japan) with a radius of 15 nm was used in these measurements. The average spring constant is about 2 N/m, and the average resonance frequency is about 65 kHz.

All the electrical transport properties were measured in a Van der Pauw geometry with a Quantum Design Physical Property Measurement System (PPMS), as introduced in **Section 2.3**.

4.3 Structural characterizations

As discussed earlier, a sample with a smooth surface and sharp interfaces are crucial for the study of coexistence of ferroelectricity and 2DEG. Figure 4.5 shows an AFM image of a 15 uc LAO/10 uc BST/STO (001) sample. Clear steps with a step height of ~ 0.4 nm similar to that of STO substrate (Fig. 2.1) can be observed, indicating smooth surface of the sample.
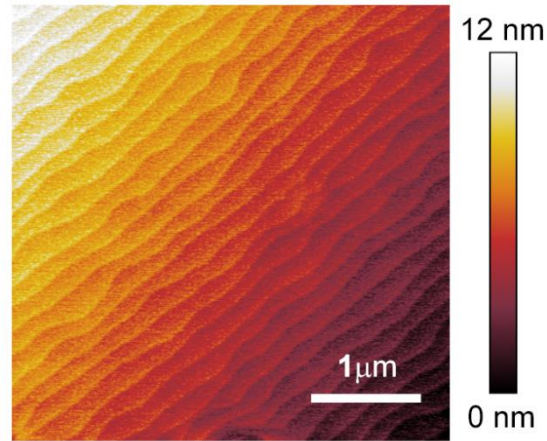
Figure 4.5 Surface characterization. AFM image of a 15 uc LAO/10 uc BST/STO (001) sample.

To check the interface quality of our samples, we performed transmission electron microscopy (TEM) measurements for a 15 uc LAO/10 uc BST/STO sample, as shown in Fig. 4.6. Figure 4.6 (a) shows a bright-field transmission electron microscopy (TEM) image of the sample. LAO/BST interface can be clearly identified from the brightness contrast. Due to the low Ba doping concentration (20%) in BST, the BST/STO interface can not be identified clearly. Nevertheless, one can see that the BST layer has the same quality as that of STO substrate. From the high-resolution TEM image in Fig. 4.6 (b), we can clearly see atomically sharp LAO/BST and BST/STO interfaces.

In summary, from our AFM and TEM measurements, we confirmed that our samples have smooth surface and atomically sharp interfaces.

97
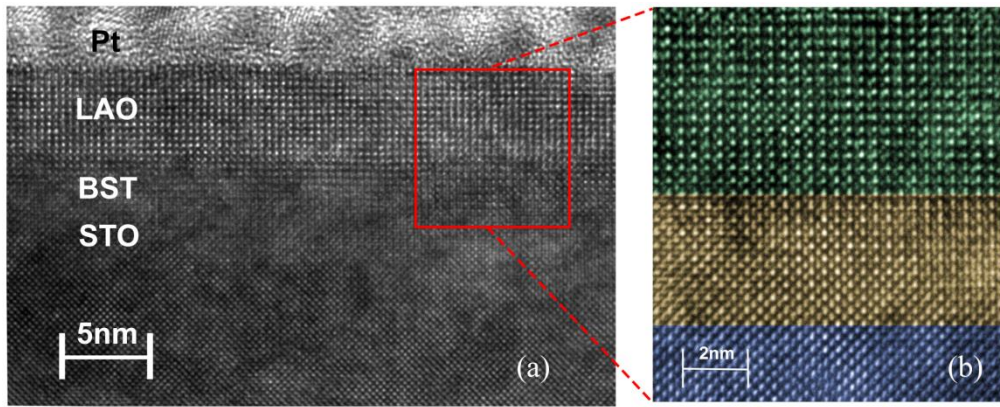
Figure 4.6 Interface characterization. (a) Cross-sectional bright field TEM image of a 15 uc LAO/10 uc BST/STO sample. Here, the Pt layer is a protective layer in TEM measurement. (b) A high-resolution TEM (HRTEM) image of the same sample in (a). Atomically sharp LAO/BST and BST/STO interfaces can be seen. For better visibility, the image is artificially coloured.

4.4 Characterizations of ferroelectricity

4.4.1 PFM characterization

To check the ferroelectricity of our BST thin films, we performed PFM measurements for a 10 uc BST/NST sample, where NST has the same lattice parameter as that of STO and was used as a bottom electrode.

Figure 4.7 shows the hysteresis loops, domain writing and reading experiments on the 10 uc BST/NST sample. Figure 4.7 (a) is a schematic illustration of the PFM setup used in the measurements. The NST substrate was grounded, while a voltage was applied between the tip and the NST substrate. Figure 4.7 (b) shows local PFM phase loops (top panel) and butterfly-like amplitude loops (bottom panel) of the sample measured at room temperature. One can see that the phase change between 4 and -7 V is approximately 180°, which indicates good ferroelectric switching. It should be noted that the loops are shifted to the negative bias side, indicating a built-in electric field of about -2.5×10^6 V/cm, which favors the spontaneous polarization in the (00$\bar{1}$) orientation, *i.e.,* downward or pointing from BST to

NST. Here, the magnitude of the built-in electric field is estimated by dividing the bias shift with the thickness of BST layer.

As an important tool to determine the ferroelectricity of a material, domain writing and reading were also performed by PFM. Figures 4.7 (c) and (d) show amplitude and phase images of the piezoelectric domains formed during the domain writing and reading experiments, respectively. Firstly, a 3×3 μm^2 square region (purple region) was written with a dc tip bias of -8 V. Then, a 1×1 μm^2 square region (orange region) was written with a dc tip bias of +8 V in the centre. Finally, amplitude and phase images were obtained simultaneously by applying a small ac bias (0.2 V) to the tip over a 5×5 μm^2 region. One can see that the central 1×1 μm^2 square shows the same colour (yellow) as that of the as-grown region (the outer 5×5 μm^2 region). This indicates that the as-grown polarization direction is downward (i.e. from BST to NST). The purple region represents switched upward polarization. These results are in accordance with the measurement shown in Fig. 4.7 (b). It should be noted that some partial relaxation was observed in Fig. 4.7 (d). This is probably due to polarization relaxation effect, which is caused by the depolarization field. Polarization relaxation has also been observed in other ferroelectric ultrathin films, such as $BaTiO_3$ [162] and $PbTiO_3$ [163].
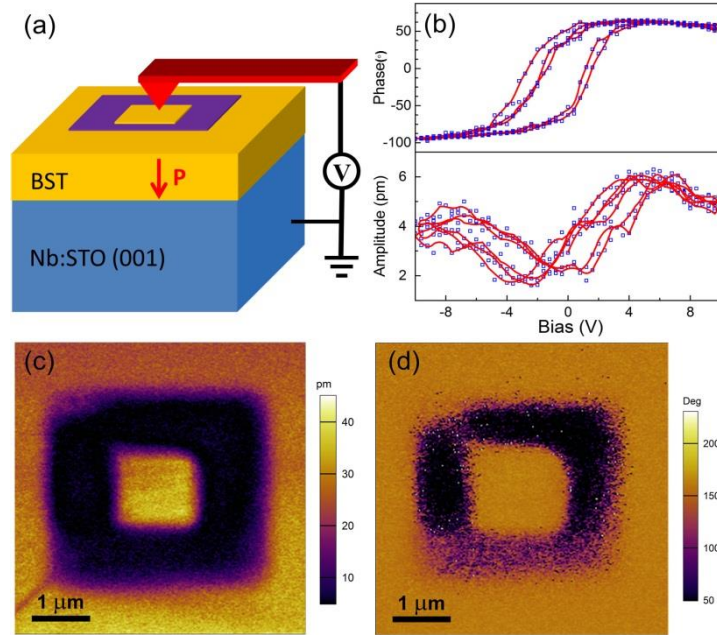
Figure 4.7 PFM characterization of the ferroelectricity of a 10 uc BST/NST sample. (a) Schematic diagram of the PFM setup used in the measurements. (b) Local phase loops (top panel) and amplitude loops (bottom panel) of the sample. (c)-(d) PFM amplitude and phase image of the sample, respectively. The image size is 5×5 μm². The purple and orange squares are 3×3 and 1×1 μm², and were written with tip voltages of -8 and 8 V, respectively. Orange region corresponds to downward polarization, while purple region represents upward polarization.

4.4.2 XRD characterization

It should be noted that the the Curie temperature (T_c) of bulk $Ba_{0.2}Sr_{0.8}TiO_3$ is around 105 K [161]. However, from our PFM measurements, room temperature ferroelectricity of a 10 uc $Ba_{0.2}Sr_{0.8}TiO_3$/NST was observed. The large shift of T_c could be induced by the compressive strain imposed by the substrate, which is known to enhance ferroelectricity in epitaxial thin films [53, 159]. $Ba_{0.2}Sr_{0.8}TiO_3$ and STO have lattice constants of 3.920 Å and 3.905 Å, respectively [164]. The compressive strain on BST exposed by STO is thus 0.4%.

To find out the strain state of the BST thin film, we performed X-ray diffraction (XRD) reciprocal space mapping (RSM) for a 10 nm BST/STO

sample. Figure 4.8 shows the RSM around (002) ((a)-(b)), (-103) (c) and (0-13) (d). One can see that BST is coherently grown on STO substrate without relaxation, i.e. the in-plane lattice constant of BST is fully constrained to that of STO substrate. From these results we calculated the lattice parameters of BST thin film as shown in Table 2. 10 nm BST grown on BST shows a tetragonal structure with $a=b=3.9051$ Å, $c=3.9713$, $\alpha= \beta= \gamma=90°$. So that c/a ratio is 1.017, which is larger than the c/a ratio of bulk $BaTiO_3$ (1.011). This large c/a ratio may be the reason for room-temperature ferroelectricity in our BST thin films. Another possible mechanism for the observed room temperature ferroelectricity is the reduced dimension effect, which was proposed to explain the room temperature ferroelectricity of strain-free STO thin films [52].

In summary, we have observed room temperature ferroelectricity in BST film as thin as 4 nm. The underlying mechanism may be either strain effect or reduced dimension effect.
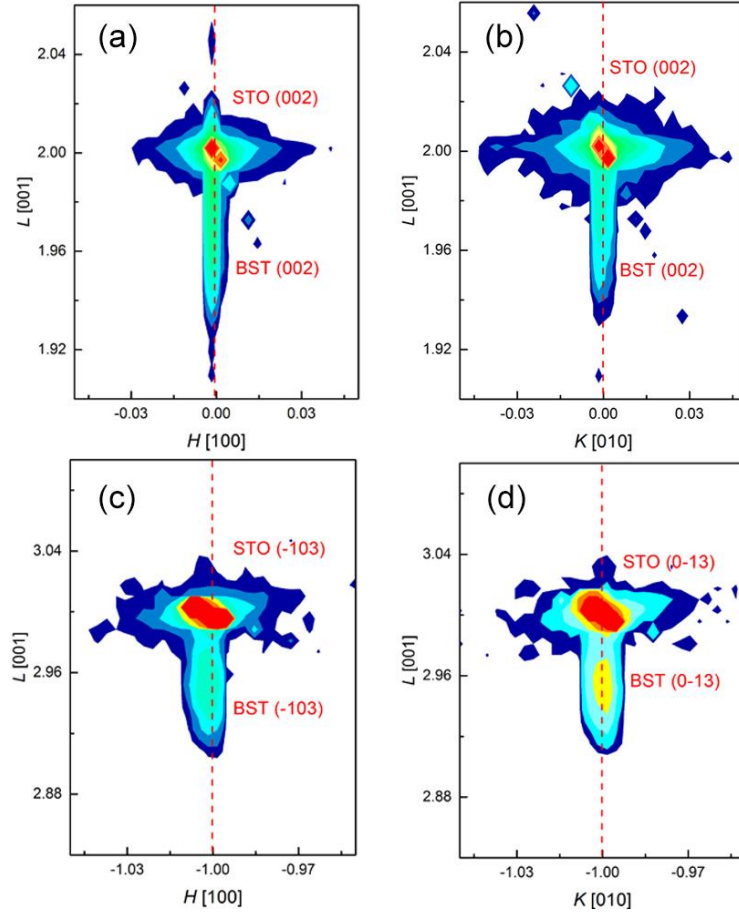
Figure 4.8 XRD reciprocal space mapping around (002) ((a)-(b), (-103) (c) and (0-13) (d) of a 10nm BST/STO sample. The red spots in the figures represent the substrate peak, while the film peak with a much lower intensity lies below the substrate peak.

	a (Å)	b (Å)	c(Å)	α (°)	β (°)	γ (°)
Value	3.9051±0.001	3.9051±0.001	3.9713±0.001	90.0000±0.1714	90.0000±0.1038	90.0000±0.1377

Table 2 Calculated lattice parameters and angels of 10 nm BST grown on STO (001) substrate.

4.5 Electronic and optical properties

Having observed room temperature ferroelectricity of the BST thin films, we grow LAO on BST to form a LAO/BST/STO heterostructure, where a 2DEG was observed at LAO/BST interface. The search for the coexistence of ferroelectricity and 2DEG is to find evidence for the persistence of ferroelectricity of BST with LAO overlayer. However, the LAO overlayer

102

makes it difficult to characterize the ferroelectricity of the underlying BST layer by PFM. Since it has been reported that switchable and hysteretic PFM response can be observed in LAO/STO heterostucture due to oxygen vacancy migration through the LAO overlayer [165]. It is also impossible to show the low-symmetry phases of BST as in Ref. [45] due to the substrate clamping effect [150]. Fortunately, as ferroelectric BST has a depolarization field, we can explore this problem by focusing on the interaction of the built-in electric field of LAO and the depolarization field of BST.

To study the interaction of the built-in electric field of LAO and the depolarization field of BST, two sets of samples were prepared. Set A is LAO/BST/STO samples with 15 uc LAO and different BST thicknesses, set B is LAO/BST/STO samples with 10 uc BST and different LAO thicknesses.

4.5.1 LaAlO$_3$/Ba$_x$Sr$_{1-x}$TiO$_3$/SrTiO$_3$ samples with 15 uc LaAlO$_3$ and different Ba$_x$Sr$_{1-x}$TiO$_3$ thicknesses

Figure 4.9 shows electronic transport properties of set A samples, *i.e.* LAO/BST/STO samples with 15 uc LAO and different BST thicknesses. Figure 4.9 (a) shows sheet resistance dependence on temperature (R_s-T) for these samples. It should be noted that a single layer of BST deposited on STO substrate is insulating, indicating that a LAO layer is required to show conductivity in LAO/BST/STO heterostructure. In high temperature regime (100-300 K), sheet resistance gradually increases as BST thickness increases. However, in low temperature regime (2-20 K), sheet resistance gradually decreases as BST thickness increases. Figures 3(b) and (c) show temperature dependent carrier density (n-T) and mobility (μ-T), respectively. One can see two features in Fig. 4.9 (b): (i) Carrier density gradually decreases with

increasing BST thickness and (ii) n-T curves become less temperature dependent with increasing BST thickness and finally turns into temperature independent when BST exceeds 8 uc. As shown in Fig. 4.9 (c), the carrier mobility of these samples increases monotonically with increasing BST thickness and reaches around 3700 $cm^2V^{-1}s^{-1}$ in the sample with 12 uc BST. This carrier mobility is at least three times larger than that of LAO/STO samples (500-1000 $cm^2V^{-1}s^{-1}$) [30]. We summarize carrier density and mobility dependence on BST thickness in Fig. 4.9 (d). Interestingly, the results in Fig. 3(a)-(d) are strikingly similar to the electric field gating experiments of LAO/STO interface [79, 85], although there is no external electric field applied in our experiments.

We attribute the results in Fig. 4.9 (a)-(d) to the competition between the built-in electric field of LAO and the depolarization field of BST. As shown in Fig. 4.7, the as-grown BST layer has a downward polarization, and thus, a negative bound charge layer is present in BST at the LAO/BST interface. This negative bound charge creates a downward electric field in LAO, which obstructs the charge transfer from LAO surface to LAO/BST interface due to the polar discontinuity. With increasing BST thickness, the magnitude of the polarization increases [162]. Consequently, the electric field created by the negative bound charge increases and less electrons (smaller carrier density) will be transferred to LAO/BST interface. Figure 4.10 shows a schematic illustration of this model.

Next, we focus on feature (ii) of Fig. 4.9 (b), i.e. temperature independent carrier density. The decreasing carrier density with decreasing temperature is generally attributed to freeze-out of oxygen-vacancy-induced carriers [30]. To

detect the oxygen vacancy concentration, we carried out photoluminescence (PL) measurements on our samples. The PL intensity is proportional to oxygen vacancy concentration in STO [21, 31]. As shown in Fig. 4.11, the peak position (490 nm) agrees well with the wavelength reported in Ref. [21]. In addition, the PL intensity gradually decreases with increasing BST thickness, indicating less oxygen vacancies. When BST exceeds 8 uc, the samples show comparable intensity as that of an as-received STO substrate, indicating that they are (nearly) free of oxygen vacancies. Theoretical calculations show that under reducing conditions, oxygen vacancy formation energy in ferroelectrics (such as BTO) is higher than that in STO [166]. We thus believe that oxygen vacancy formation energy in ferroelectric BST is higher than that in paraelectric STO. Thus it's reasonable that oxygen vacancy content decreases as BST thickness increases. When BST thickness is below 8 uc (~3.2nm), 2DEG resides both in STO and BST. Thus a large number of oxygen-vacancy-induced carriers are present in STO. When BST thickness exceeds 8 uc, 2DEG reside mainly in BST. Thus few oxygen-vacancy-induced carriers are present and the carriers mainly come from the polar discontinuity mechansim, leading to observation of temperature-independent carrier density. These results are in good agreement with previous observations, which showed that the thickness of the 2DEG at LAO/STO interface is around 2-4 nm [139-141]. This kind of temperature-independent carrier density has also been observed in polarization-induced 2DEG at AlGaN/GaN interface [167] and $CaZrO_3/SrTiO_3$ interface [168].

As to the mobility enhancement, it is attributed to less electron scattering and less defect scattering as less oxygen vacancies are formed when BST thickness increases.
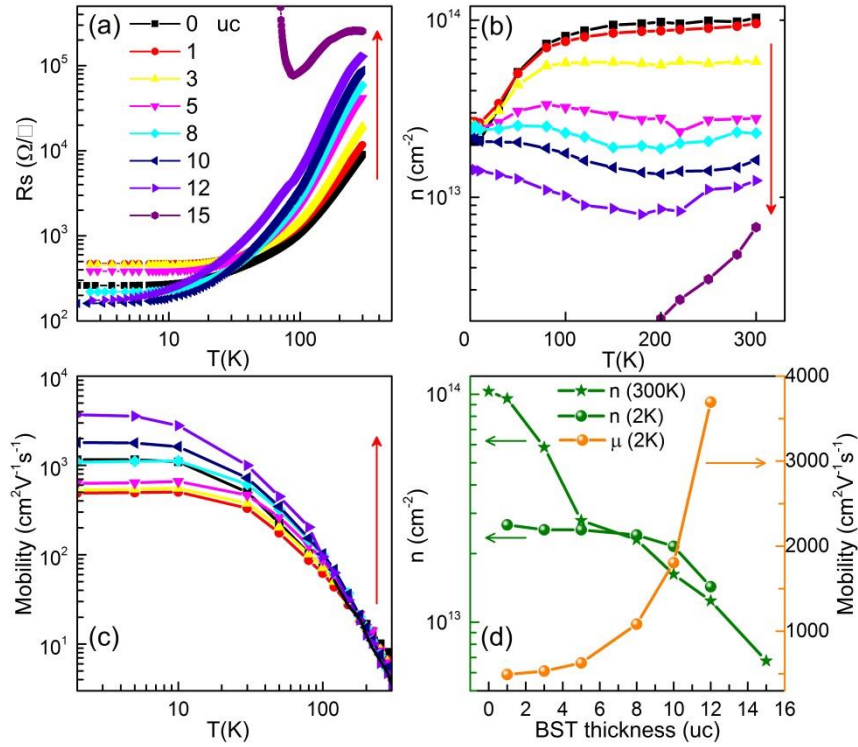
Figure 4.9 Electronic transport characterization of the 2DEG in LAO/BST/STO heterostructure (set A samples). (a) Sheet resistance, (b) carrier density, and (c) mobility dependence on temperature for samples with fixed LAO thickness (15 uc) and different BST thicknesses on STO substrate. Different colors represent samples with different BST thicknesses. Red arrows in (a)-(c) indicate increasing BST thickness. (d) Carrier density (left scale) dependence on BST thickness at 300 K (olive star) and 2 K (olive ball). Electron mobility (right scale) dependence on BST thickness at 2 K (orange ball).
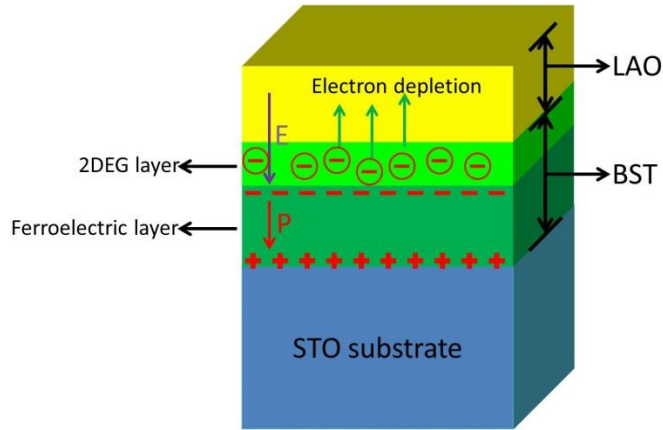
Figure 4.10 Schematic illustration of the bound charge distribution in BST layer and its influence on the 2DEG at LAO/BST interface.
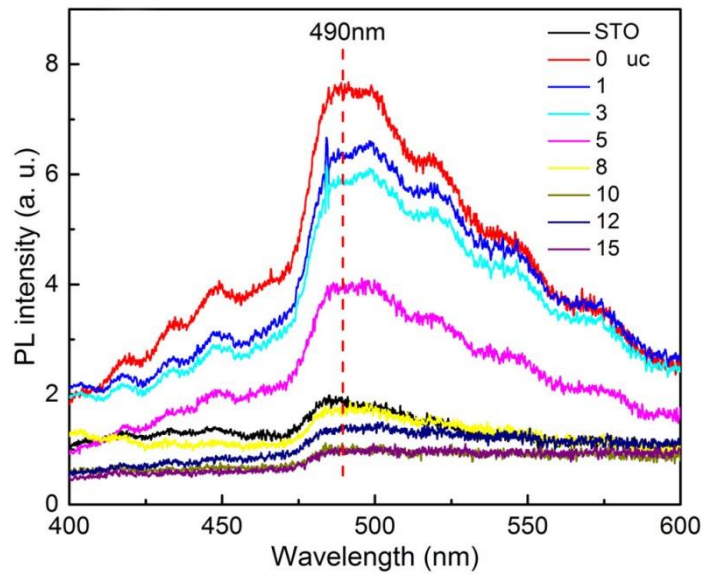
Figure 4.11 Photoluminescence measurement of oxygen vacancy concentration. Room-temperature PL spectra of the same samples in Fig. 4.9 and an as-received STO substrate. Here, STO substrate is used as a reference sample, which is (nearly) free of oxygen vacancy. Different colors indicate different thicknesses of BST, while LAO is fixed to 15 uc.

4.5.2 LaAlO$_3$/Ba$_x$Sr$_{1-x}$TiO$_3$/SrTiO$_3$ samples with 10 uc Ba$_x$Sr$_{1-x}$TiO$_3$ and different LaAlO$_3$ thicknesses

To verify the competition between the built-in electric field of LAO and the depolarization field of BST, another set of sample (set B) with fixed BST thickness (10 uc) and different LAO thicknesses (0-25 uc) was prepared.

Figure 4.12 (a) shows temperature dependent sheet resistance (R_s-T) for these samples. When LAO thickness n is below 8 uc, the samples show bad

107

conductivity and the data are not shown here. For 8 uc $\leq n <$20 uc, R_s-T curves

show fully metallic behavior from 300 to 2 K. The upturn at around 40 K is

observed for samples with $n \geq$ 20 uc, which is probably due to Kondo effect as

also observed in LAO/STO when LAO thickness is larger than 26 uc [65].

Due to the electric field produced by BST, the critical thickness (t_c) of LAO

for insulator-metal transition should be larger than that of LAO/STO

heterostructure. Experimentally, the t_c was found to be 5-8 uc, which is larger

than the t_c of LAO/STO (4 uc). As shown in Fig. 4.12 (b), the conductance of

the 2DEG increases by five orders from 5 to 8 uc of LAO. Here, conductance

is defined as σ=1/R_s.

In addition, the t_c for LAO/ 10 uc BST/STO heterostructure can also be

estimated from built-in electric field in 10 uc BST as deduced from our

previous PFM measurement. The electric field in LAO is estimated to be 3.2

eV/4$\times$4 Å=2$\times$10^7 eV/cm. The built-in electric field in 10 uc BST is 2.5$\times$10^6

V/cm. From a simple electrostatic picture, t_c is estimated to be

$t_c = \frac{3.2 \text{ eV}}{(2-0.25)\times 10^7 \text{eV/cm}} \approx$ 4.6 uc. This estimation is in good agreement with our

experimental observation.

Fig. 4.12 (c) and (d) show temperature dependent carrier density (n-T) and

mobility (μ-T) for set B samples, respectively. Carrier density and mobility of

LAO/STO samples are also shown for comparison. As can be seen in Fig. 4.12

(a), all the LAO/BST/STO samples show smaller carrier density than that of

LAO/STO samples. In addition, all the LAO/BST/STO samples show

temperature independent carrier density, as opposed to LAO/STO samples,

whose carrier density decreases with temperature. These features indicate

ferroelectric depletion of carriers and suppression of oxygen vacancy formation in LAO/BST/STO samples as explained in **Section 4.5.1**. As shown in Fig. 4.12 (d), all the LAO/BST/STO samples show higher mobility (1500-2000 $cm^2V^{-1}s^{-1}$) than that of LAO/STO samples (500-1000 $cm^2V^{-1}s^{-1}$). This is due to less electron scattering and defect scattering as explained in **Section 4.5.1**.
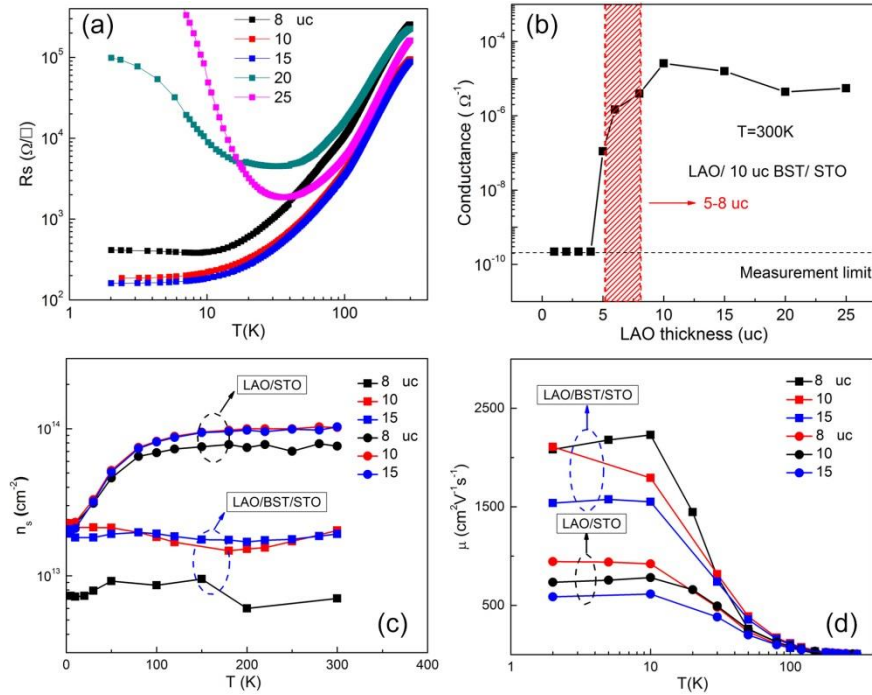
Figure 4.12 Electronic transport characterization of the 2DEG in LAO/BST/STO heterostructure (set B samples). (a) Temperature dependent sheet resistance for these samples. (b) Conductance dependence on LAO thickness. (c) Carrier density and (d) mobility for LAO/STO and LAO/BST/STO samples with different LAO thickness. Here, BST is fixed to 10 uc and different colors represent different LAO thicknesses. The filled circles and rectangles in (c) and (d) indicate LAO/STO and LAO/BST/STO samples, respectively.

In summary of **Section 4.5.1** and **4.5.2**, we have shown the interaction between the built-in electric field of LAO and the depolarization field of BST through detailed transport measurements. As a result of this interaction, the carrier density and mobility of the 2DEG in BST can be modulated.

Meanwhile, the oxygen vacancies can be suppressed by the ferroelectric BST layer.

4.6 First-principles calculations

In order to investigate the relation between charge density and ferroelectricity in LAO/BST/STO heterostrcutre, we performed density-functional theory (DFT) based calculations on the partial charge of conducting electrons and the displacements between anions and cations in BST, as shown in Fig. 4.13. For simplicity of our calculations, instead of using $LaAlO_3/Ba_{0.2}Sr_{0.8}TiO_3/SrTiO_3$ heterostructure, we used $LaAlO_3/ Ba_{0.5}Sr_{0.5}TiO_3/SrTiO_3$ heterostructure.

Our first-principles calculations were performed using density-functional theory based Vienna ab initio Simulation Package (VASP) [145, 146] with the local density approximation (LDA) for the exchange-correlation functional [169] and the frozen-core all-electron projector-augmented wave (PAW) method [147, 148]. The cutoff energy for the plane wave expansion is set to 400 eV. Monkhorst-Pack k-point grids for Brillouin zone sampling are set to $6\times6\times6$ for bulk $SrTiO_3$, $6\times6\times6$ for bulk $LaAlO_3$, $5\times5\times6$ for bulk $Ba_{0.5}Sr_{0.5}TiO_3$, and $5\times5\times1$ ($10\times10\times1$) for $LaAlO_3/Ba_{0.5}Sr_{0.5}TiO_3/SrTiO_3$ superlattice structure relaxation (static calculations), respectively. The structures are fully relaxed until the forces are smaller than 0.01 $eVÅ^{-1}$ for the bulk $LaAlO_3$, $Ba_{0.5}Sr_{0.5}TiO_3$, $SrTiO_3$, and 0.02 $eVÅ^{-1}$ for $LaAlO_3/Ba_{0.5}Sr_{0.5}TiO_3/SrTiO_3$ superlattice structure. The equilibrium lattice constant for $SrTiO_3$ is 3.865 Å. We fix the in-plane lattice constant of $LaAlO_3$ and $Ba_{0.5}Sr_{0.5}TiO_3$ to this number and optimize their c axis into 3.66 and 3.96 Å, respectively. For $Ba_{0.5}Sr_{0.5}TiO_3$, the ratio of Ba and Sr is set to 1:1. We use $\sqrt{2} \times \sqrt{2} \times 1$

supercell for $LaAlO_3/Ba_{0.5}Sr_{0.5}TiO_3/SrTiO_3$ superlattice, which is a symmetric structure with 4.5 uc $SrTiO_3$ in the middle, 5 uc $Ba_{0.5}Sr_{0.5}TiO_3$ on each of its two TiO_2 terminals, and then 3.5 $LaAlO_3$ on top of $Ba_{0.5}Sr_{0.5}TiO_3$ (Fig. 4.13 (c) shows half of this structure).

Figure 4.13 (a) shows layer-resolved charge density distribution in $LaAlO_3/Ba_{0.2}Sr_{0.8}TiO_3/SrTiO_3$ heterostructure, which is calculated by performing a partial charge calculation of the conduction bands below Fermi level. One can see that the electrons mainly locate at Ti atoms in both $Ba_{0.5}Sr_{0.5}TiO_3$ and $SrTiO_3$. In addition, the charge density has the maximum value at $LaAlO_3/Ba_{0.5}Sr_{0.5}TiO_3$ interface (0.21 e/uc), and decays gradually from this interface into $SrTiO_3$.

Figure 4.13 (b) shows layer-resolved displacements between anions and cations in $Ba_{0.5}Sr_{0.5}TiO_3$. All the displacements (Ti-O, Ba-O and Sr-O) gradually decrease from $LaAlO_3/Ba_{0.5}Sr_{0.5}TiO_3$ interface to $Ba_{0.5}Sr_{0.5}TiO_3/SrTiO_3$ interface. In addition, we found that the spontaneous polarization direction of $Ba_{0.5}Sr_{0.5}TiO_3$ on $SrTiO_3$ is pointing-down, which is the same as the case for BST/NST, as confirmed by PFM measurements in Fig. 4.7. Figures 4.14 (a) and (c) show side and top view of the simulation cell of the $LaAlO_3/5$ uc $Ba_{0.5}Sr_{0.5}TiO_3/SrTiO_3$ heterostructure. Figure 4.14 (b) shows that Ti^{4+} and Sr^{2+} (or Ba^{2+}) ions are displaced downward relative to O^{2-}, which creates a downward polarization in BST.

Several mechanisms may contribute to behaviour of the layer-dependent displacement. (i) A depolarizing buckling (or polar distortion) could occur in $Ba_{0.5}Sr_{0.5}TiO_3$ to compensate the built-in electric field in LAO. This buckling

has been widely reported in LAO/STO heterostructure and could lead to the layer-dependent displacement behaviour [170-172]. (ii) Screening of the depolarization field of $Ba_{0.5}Sr_{0.5}TiO_3$ by the insulating $SrTiO_3$ substrate. In an earlier report, Chisholm *et al.* reported that the depolarization field of $PbZr_{0.2}Ti_{0.8}O_3$ in $PbZr_{0.2}Ti_{0.8}O_3/SrTiO_3$ heterostructure could be screened by oxygen vacancies in $SrTiO_3$ [173]. This screening could lead to diminishing displacement in $Ba_{0.5}Sr_{0.5}TiO_3$ in the first few layers away from $Ba_{0.5}Sr_{0.5}TiO_3/SrTiO_3$ interface. (iii) Screening of ferroelectricity by itinerant electrons. As proposed by Wang *et al.*, the critical electron density for stable ferroelectric displacement in $BaTiO_3$ is 0.11 e/uc [43]. Here, we observed large Ti-O displacement (0.17 Å) at the $LaAlO_3/ Ba_{0.5}Sr_{0.5}TiO_3$ interface with an electron density ~0.21 e/uc. This result indicates that several of the above mentioned mechanisms are present in the LAO/BST/STO heterostructure. Nevertheless, the overall effect that one can clearly observe in Fig. 4.13 is the coexistence of 2DEG and ferroelectricity (or the anion-cation displacement).
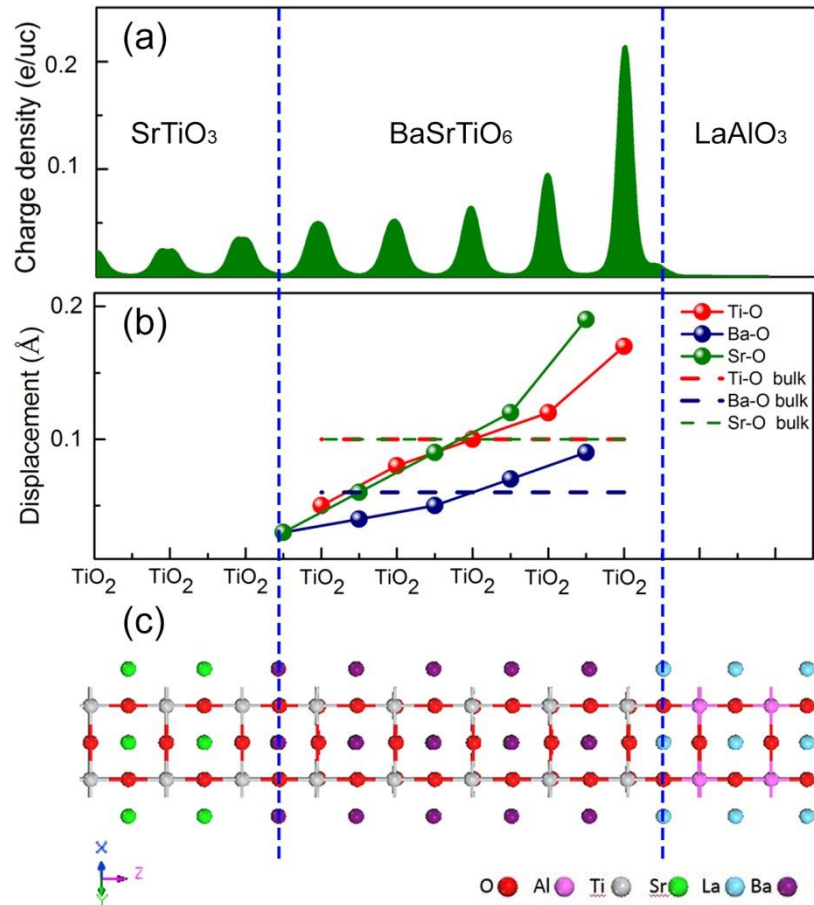
Figure 4.13 First-principles calculations of LaAlO$_3$/Ba$_{0.5}$Sr$_{0.5}$TiO$_3$/SrTiO$_3$ heterostructure. (a) Layer-resolved in-plane average charge density along the <001> direction (b) Layer-resolved displacement between the anions and cations in BST and (c) structural guide for the supercell used in the calculations. The red, blue and green balls in (b) indicate the Ti-O, Ba-O and Sr-O displacements, respectively. The corresponding displacements of Ti-O, Ba-O and Sr-O in bulk BST are shown by red, blue and green dashed lines, respectively.
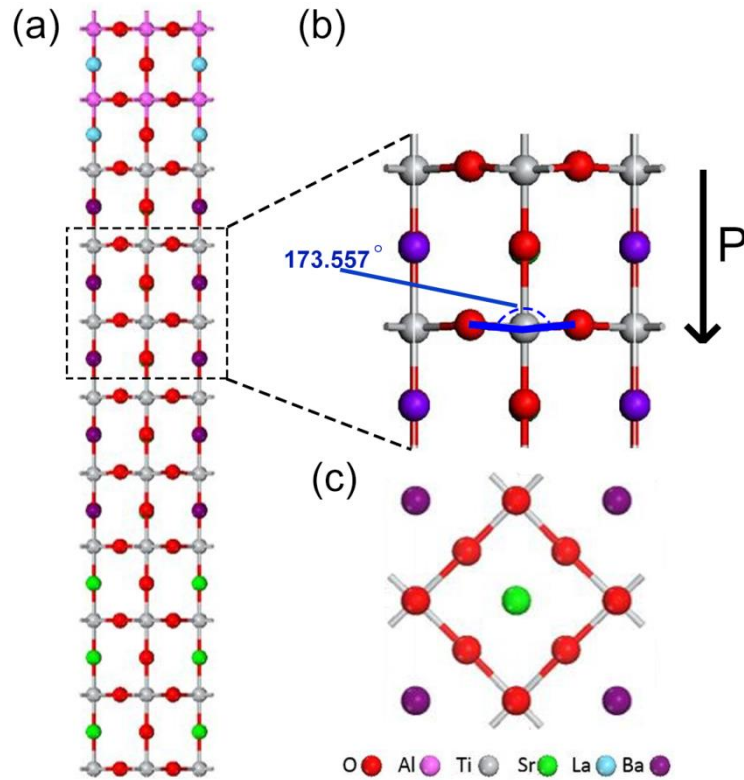
Figure 4.14 (a) Side view of LaAlO$_3$/Ba$_{0.5}$Sr$_{0.5}$TiO$_3$/SrTiO$_3$ heterostructure. (b) Zoom-in of Ba$_{0.5}$Sr$_{0.5}$TiO$_3$ layer showing spatial displacement of Ti-O and Sr – O (Ba-O). This displacement creates a downward polarization in Ba$_{0.5}$Sr$_{0.5}$TiO$_3$. (c) Top view of the Ba$_{0.5}$Sr$_{0.5}$TiO$_3$ layer.

4.7 Summary

In conclusion, by a combination of PFM, electronic transport and optical measurements, we observed systematic change of the transport properties of the 2DEG in LAO/BST/STO heterostructure with increasing BST thickness. This systematic change is attributed to the interaction between the built-in electric field of LAO and the depolarization field of BST, and thus, it signifies the coexistence of ferroelectricity and 2DEG in this heterostructure. Furthermore, through first-principles calculations, we showed layer-resolved carrier density and ferroelectricity in BST.

Author contributions:

W. X. Zhou and Ariando designed the experiment. W. X. Zhou prepared the samples and conducted the electronic transport measurements. J. X. Xiao and W. X. Zhou conducted the PFM measurements. J. Zhou conducted the DFT calculations. P. Yang and W. X. Zhou conducted the XRD measurements. C. G. Li performed the PL measurements. The TEM measurements were conducted by Y. Yang. W. X. Zhou, S. W. Zeng, C. J. Li, Z. Huang, J. Zhou and Ariando analyzed the data. R. Guo, W. M. Lü, H. J. Harsan Ma, K. Han, S. J. Chua, K. Y. Zeng, J. S. Chen, T. Venkatesan and Y. P. Feng joined the discussion.

Chapter 5 Ferroelectricity induced ferromagnetism in paramagnetic Pt thin films

Abstract

Electric and ferroelectric control of magnetic properties is crucial for applications in the field of spintronics and magnetoelectronics. Here, we report ferroelectricity induced room-temperature ferromagnetism in paramagnetic Pt thin films in a $Pt/BaTiO_3/SrTiO_3$ (001) heterostructure at the $Pt/BaTiO_3$ interface. The average magnetic of a 2 nm Pt thin film on 20 unit cells of $BaTiO_3$ at 300 K is ~0.03 μ_B/Pt. Our first-principles calculations indicate that the depolarization field of $BaTiO_3$ and the substitution of Ti with Pt at the $Pt/BaTiO_3$ interface are responsible for the unusual ferromagnetism in Pt. Our findings provide a routine to induce ferromagnetism in an otherwise nonmagnetic material.

5.1 Motivation

Electric-field control of ferromagnetism (FM) has been investigated extensively over the past decades due to its fundamental and technological importance, especially in view of recent developments in magnetoelectronics and spintronics [100-107]. Up to now, electric-field control of ferromagnetic properties has been demonstrated in magnetic semiconductors [100] [103], metals [104, 105] and complex oxides [106, 107]. Some prominent examples are the electric-field control of Curie temperature of (In,Mn)As [100], Co [104] and manganites thin films [107], electric-field control of magnetic anisotropy of (Ga,Mn)As [103], FePt and FePd thin films [105].

A non-volatile control of ferromagnetism can be realized by integrating ferroelectricity (FE) into the system. Ideally, one would expect to find a

material with both ferromagnetic and ferroelectric order, i.e. a single-phase multiferroic material. However, this kind of material is scarce as ferromagnetism normally requires partially filled d^n orbitals, while ferroelectricity prefers empty d^0 orbitals [174]. One important approach to solve or circumvent this problem is epitaxial heterostrucutures, which contain alternating conventional ferromagnetic and ferroelectric thin films, i.e. in a FM/FE configuration. In this configuration, ferroelectric control of ferromagnetism can be realized through interfacial converse magnetoelectric effect or piezostrain effect. For example, ferroelectric control of magnetization of $La_{0.67}Sr_{0.33}MnO_3$ [109] and FeRh [108] in $La_{0.67}Sr_{0.33}MnO_3$/ $BaTiO_3$ and $FeRh/BaTiO_3$ heterostructures by switching the polarization direction of $BaTiO_3$, respectively. One important application of ferroelectric control of ferromagnetism is the so-called multiferroic tunnel junction (MFTJ), which has a FM/FE/FM structure. In a MFTJ, non-volatile ferroelectric control of spin polarization can be realized, for example, in a $Fe/BaTiO_3/La_{0.67}Sr_{0.33}MnO_3$ [102] or a $Co/PbZr_{0.2}Ti_{0.8}O_3/La_{0.7}Sr_{0.3}MnO_3$ [114] heterostructure. The above researches have greatly improved our ability to control ferromagnetism, however, most of the researches were focused on electric-field or ferroelectric-field modulation between two ferromagnetic states. One reasonable question one can ask is: Is it possible to drive a non-magnetic material into ferromagnetic with ferroelectricity?

To investigate the above question, it's important to choose an appropriate non-magnetic material. Pt (or Pd), a non-magnetic metal with large spin-orbit coupling, is an excellent candidate for exploiting this problem. Pt (or Pd) nearly satisfies the Stoner criterion for ferromagnetism, i.e. it lies at the

boundary of ferromagnetism and paramagnetism, and thus a moderate perturbation could be expected to induce ferromagnetism in Pt (or Pd). Ferromagnetism has been widely reported in Pt (or Pd) nanoparticles due to electronic structure modification induced by reduced dimension [175, 176]. Recently, induced ferromagnetism has been reported in Pt thin films deposited on a ferromagnetic $Y_3Fe_5O_{12}$ substrate due to magnetic proximity effect [177, 178]. In addition, by using ionic liquid gating, Shimizu *et al.* have reported electrically induced ferromagnetism in Pt thin films [179].

In this chapter, we report ferroelectricity induced ferromagnetism in paramagnetic Pt thin films in a $Pt/BaTiO_3/SrTiO_3$ (Pt/BTO/STO) (001) heterostructure. We observed anomalous Hall effect (AHE) in the Pt/BTO/STO heterostructure. The AHE was attributed to ferromagnetism of Pt. The magnetic moment of Pt is ~ 0.03 and 0.11 μ_B/Pt at 300 and 2 K, respectively. Our first-principles calculations indicate that the depolarization field of BTO and Ti substitution with Pt at the Pt/BTO interface is essential for the observed ferromagnetism in Pt.

5.2 Experimental methods

5.2.1 Sample growth

The Pt/BTO/STO samples were prepared by a combination of pulsed laser deposition (PLD) and magnetron sputtering process. Prior to the deposition, STO (001) substrates were treated with the method in **Section 2.1.1** to obtain atomically sharp surfaces. The STO substrates were then loaded into a PLD chamber, which is equipped with *in-situ* reflection high-energy electron diffraction (RHEED), to deposit BTO. During the deposition, the temperature

118

and oxygen partial pressure were kept at 800 ℃ and 10^{-3} torr, respectively. Fig. 5.1 (a)-(b) show RHEED patterns for STO (001) substrate and after BTO deposition at 800 ℃, respectively. The clear Laue circles and Kikuchi lines indicate two-dimensional epitaxial growth of BTO on STO. The RHEED oscillations for a 20uc BTO/STO sample indicate layer-by-layer growth, as shown in Fig. 5.1 (c). After BTO deposition, the samples were *in-situ* annealed at 800 ℃ with an oxygen pressure of 1 torr for 1 hour to compensate oxygen vacancies. Subsequently, the samples were cooled down to room temperature at a rate of 10 ℃/min. After the cooling-down process, the samples were *in-situ* transferred into a magnetron sputtering chamber through a transfer chamber without breaking the vacuum. Pt thin films on BTO/STO were deposited at room temperature with magnetron sputtering.
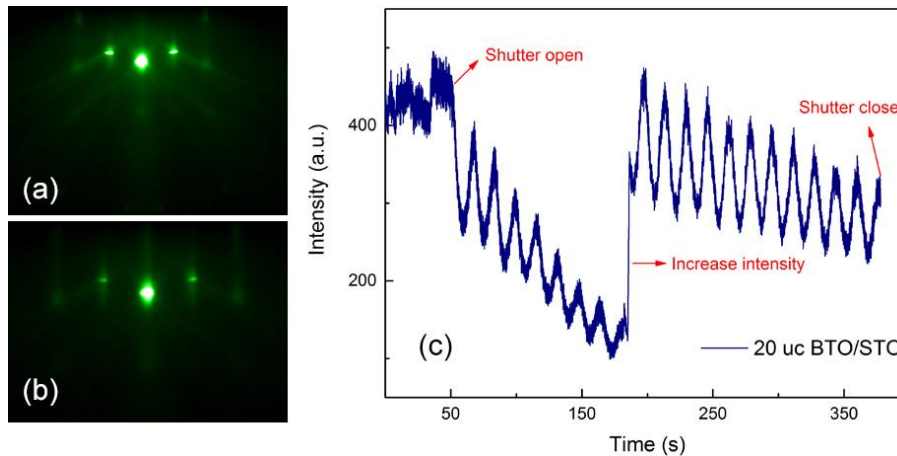
Figure 5.1 RHEED pattern of a STO (001) substrate (a) and after BTO deposition (b) at 800 ℃. (c) RHEED oscillation of 20 uc BTO on STO (001) substrate.

5.2.2 Hall bar fabrication

To facilitate electronic transport measurements, Hall bars were fabricated on a standard 5×5 mm^2 Pt/BTO/STO sample. Firstly, the as-grown Pt/BTO/STO

samples were patterned with photoresist, which covered the Hall bar regions. Subsequently, the regions without photoresist were removed with argon milling. This process was *in-situ* monitored with secondary ion mass spectrometry (SIMS) to make sure that the Pt was fully removed outside the Hall bar regions. Finally, the photoresist was removed by standard lift-off techniques. Figure 5.2 shows optical microscope image of a 5×5 mm^2 2nm Pt/20 uc BTO/STO sample with four Hall bars. The channel dimension of each hall bar is 50×160 μm^2. The Hall bar region has a Pt/BTO/STO heterostructure (which is conducting), while the other region is BTO/STO heterostructure (which is insulating).

Figure 5.2 Optical microscope image of the Hall bars patterned on a 5×5 mm^2 Pt/BTO/STO sample. Four Hall bars were fabricated on the 5×5 mm^2 sample.

5.2.3 Electric and magnetic measurements

The electronic transport properties were measured with a Quantum Design Physical Properties Measurement System (PPMS). The magnetic properties were measured with a Quantum Design Superconducting Quantum Interference Device-Vibrating Sample Magnetometer (SQUID-VSM) system.

5.3 Structural characterizations

5.3.1 Surface characterization

As introduced in previous chapters, a sample with a smooth surface and sharp interfaces are crucial for the physical properties of a heterostructure. Figure 5.3 shows AFM image of a 2 nm Pt/20 uc BTO/STO sample. Clear steps with a step height of ~ 0.4 nm similar to that of STO substrate (Fig. 2.1) can be observed. The root-mean-square (RMS) roughness is ~ 0.2 nm, indicating atomically smooth surface of the sample.
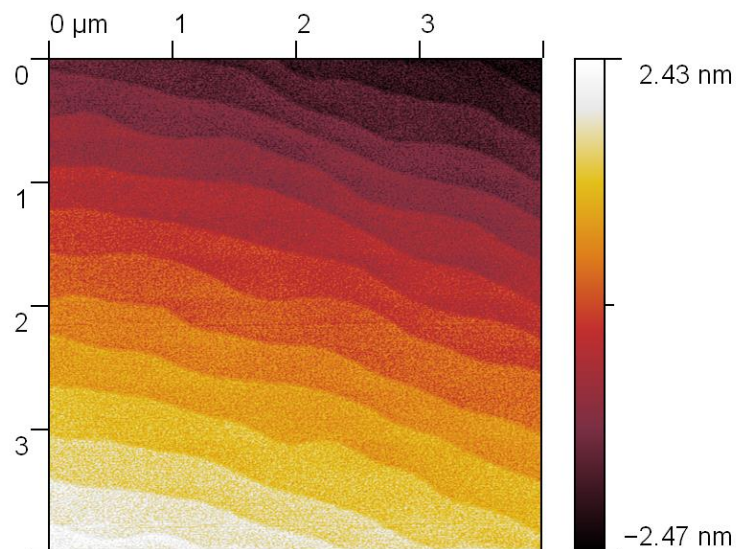
Figure 5.3 AFM image of a 2 nm Pt/20 uc BTO/STO sample over a 4×4 μm^2 region.

5.3.2 XRD

As introduced in Section 4.1, BTO normally has two types of domains, *i.e. a*- and *c*-domain. To check the crystallinity of our BTO thin films, we performed X-ray diffraction (XRD) measurement on a 50 uc BTO/STO (001) sample, as shown in Fig. 5.4. One can see that BTO is epitaxially grown on STO (001) substrate along (001) direction. This indicates that our BTO thin films grown on STO is single crystalline. The out-of-plane constant of BTO thin film is

4.134 Å, which is larger than that of BTO (4.032 Å) [180]. This elongation of out-of-plane lattice constant is caused by the in-plane compressive strain on BTO imposed by STO substrate.
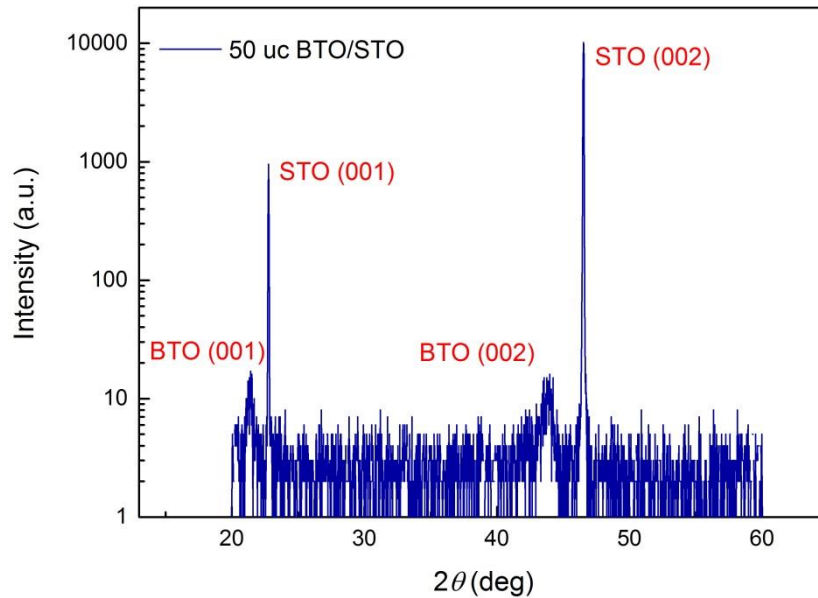
Figure 5.4 XRD measurement of a 50 uc BTO/STO (001) sample. The diffraction peaks for STO and BTO are labeled in the figure.

5.4 Characterizations of ferroelectricity

To characterize the ferroelectricity of the BTO thin films, we prepared a sample with 20 uc BTO deposited on $Nb:SrTiO_3$ (NST) (0.1 wt% Nb doped) (001) substrate, where NST serves as the conducting bottom electrode. The preparation process of the BTO/NST sample was the same as that for BTO/STO samples introduced in **Section 5.2.1**.

Domain writing and reading experiments were carried out on the 20 uc BTO/NST sample with a piezoresponse force microscope (PFM). The details of the PFM setup and experimental procedures have been introduced in Section 4.2 and 4.4.1. Figure 5.5 shows phase image of the piezoelectric domains formed during the domain writing and reading experiments. Here, the

phase image refers to the polarization direction of the material. Firstly, a 2×2 μm² square region (purple region) was written with a dc tip bias of -5 V. Then, the phase image was obtained by applying a small ac bias (0.2 V) to the tip over a 4×4 μm² region. One can see that the phase contrast between the purple and yellow region is ~180°, indicating good switching of the polarization with the external dc bias. From these experiments, we can determine that the as-grown polarization of BTO on NST is downward, i.e. pointing from BTO to NST. The purple region represents switched upward polarization, whereas the yellow region indicates downward spontaneous polarization. These results are very similar to those of BST/NST samples introduced in Section 4.4.1.
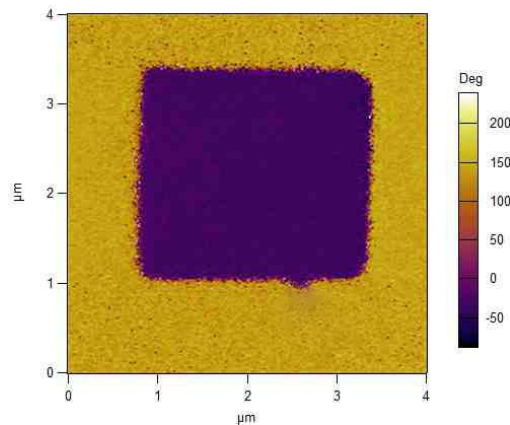
Figure 5.5 PFM phase image of a 20 uc BTO/NST sample. The image size is 4×4 μm². The purple square (2×2 μm²) in the center was written with a dc tip voltage of -5 V. Yellow region corresponds to downward polarization, while purple region represents upward polarization.

5.5 Electronic transport properties

In order to investigate the possible influence of ferroelectricity (or BTO) on magnetic properties of Pt thin films, we prepared two samples: 2 nm Pt/20 uc BTO/STO (001) and 2 nm Pt/STO (001), where the latter serves as a reference sample.

5.5.1 Temperature dependent resistance

Figure 5.6 shows temperature dependent sheet resistance (R_s-T) for the two samples. From the R_s-T curves, one can see that both samples show metallic behavior as Pt is a metal. The small upturn at ~15 K is probably caused by weak localization of electrons due to dimensional effect, as explained by Y. M. Lu *et al.*[178]. The sheet resistance of the reference sample, *i.e.* 2 nm Pt/STO, is in good agreement with previous reports [178, 179].

Interestingly, the 2 nm Pt/20 uc BTO/STO shows significantly smaller sheet resistance than that of the 2 nm Pt/STO sample, although the Pt thickness is the same. The relative resistance change is as large as 40% at room temperature. Here, the relative resistance change is defined as $(R_{ref} - R_{BTO})/R_{ref}$, where R_{ref} and R_{BTO} are sheet resistances of 2 nm Pt/STO and 2 nm Pt/20 uc BTO/STO, respectively. We also investigated samples with different Pt thicknesses, and similar resistance change was observed when Pt thickness is smaller than 4 nm. The sheet resistance for a 4 nm Pt/20 uc BTO/STO sample is almost the same as that of a 4 nm Pt/STO sample.
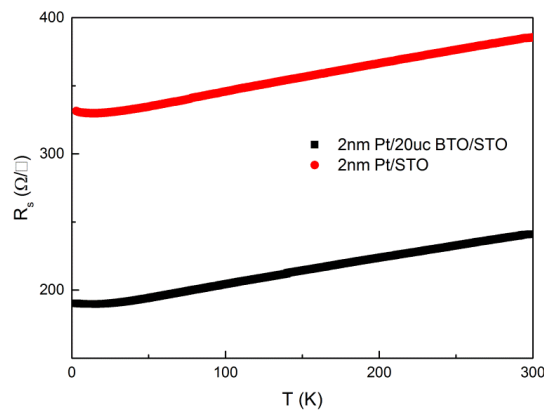
Figure 5.6 Temperature dependent sheet resistance for a 2 nm Pt/20 uc BTO/STO and a 2 nm Pt/STO sample.

5.5.2 Anomalous Hall effect

As Pt is a paramagnetic metal, it should display normal Hall effect if no external stimulus is applied. Figure 5.7 (a) shows Hall resistance dependence on magnetic field (R_H-H) for the 2 nm Pt/STO sample. As can be seen, R_H is linearly dependent on magnetic field, indicating normal Hall effect. In addition, the Hall effect is almost temperature independent. These results are expected as STO is non-magnetic (or diamagnetic) and paraelectric, which does not impose any external stimulus to Pt.

Strikingly, the 2 nm Pt/20 uc BTO/STO sample shows anomalous Hall effect (AHE), as shown in Fig. 5.7 (b). Two main features can be observed in Fig. 5.7 (b). First, R_H is non-linearly dependent on H. Second, the R_H-H curves are strongly temperature dependent and a sign reversal can be observed at ~10 K. Generally, AHE are observed in two types of systems, i.e. multicarrier system and ferromagnetic system. For a system with multiple carriers, for example, $LaAlO_3/SrTiO_3$ superlattices [124] and $LaTiO_3/SrTiO_3$ superlattices [181], the R_H-H curves can be well explained with multiple carriers with different carrier densities and carrier mobilities. We note that Fredrickson *et al.* theoretically predicted a two-dimensional electron gas (2DEG) at $BaTiO_3/SrTiO_3$ (BTO/STO) interface due to the polar discontinuity at this interface similar to that of $LaAlO_3/SrTiO_3$ interface [93]. If there is a 2DEG at the $BaTiO_3/SrTiO_3$ interface, the AHE observed here could be attributed to a multicarrier model. However, experimentally, we found that 20 uc BTO deposited on STO (001) substrate is insulating, with a room-temperature resistance larger than 10^8 Ω (measurement limit). In addition, we performed resistance measurement on a 2 nm Pt/20 uc BTO/STO sample by only contacting Pt without penetrating into

BTO/STO interface. The resistance is the same as that measured with the wire-bonding technique, which penetrates into BTO/STO interface and contacts both Pt and the 2DEG (if any). This indicates that no 2DEG is formed at BTO/STO interface. Moreover, attempts to fit the AHE in Fig. 5.7 (b) with the multicarrier model were unsuccessful, especially at low temperature (e.g. 2.5 K) with the sign reversal. We believe the absence of 2DEG at BTO/STO interface under our preparation conditions is probably because that the polar discontinuity at BTO/STO is compensated by other compensation mechanisms (other than electronic reconstruction), such as atomic reconstruction, domain formation or oxygen vacancy compensation [173].

Due to the similarity of our results with those reported in ionic gating experiment of Pt/Al_2O_3 in Ref. [179] and the proximity effect induced ferromagnetism in $Pt/Y_3Fe_5O_{12}$ in Ref. [177], we attribute the AHE to induced ferromagnetism in Pt thin films.
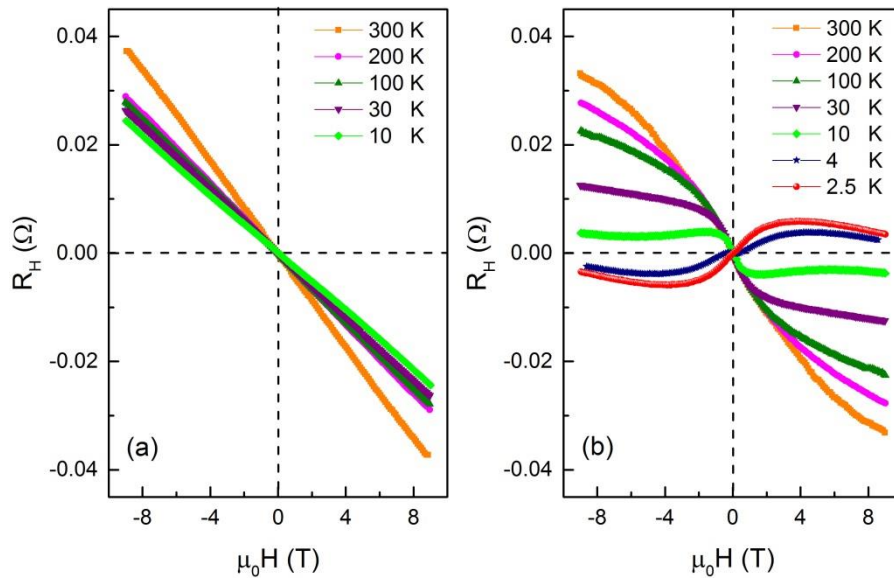
Figure 5.7 Hall effect measurement. Hall resistance (R_H) dependence on magnetic field (*H*) from -9 to 9 T at different temperatures for 2 nm Pt/STO (a) and 2 nm Pt/20 uc BTO/STO (b), respectively. The 2 nm Pt/STO sample

shows normal Hall effect, while the 2 nm Pt/20 uc BTO/STO sample shows anomalous Hall effect.

5.6 Magnetic properties

In order to check the magnetic properties of our Pt/BTO/STO samples, we performed magnetic measurements with a Quantum Design Superconducting Quantum Interference Device-Vibrating Sample Magnetometer (SQUID-VSM) system.

Figure 5.8 shows in-plane magnetic moment dependence on magnetic field (m-H) for a 2 nm Pt/20 uc BTO/STO sample. Narrow hysteresis loops can be observed from 300 to 2 K, indicating ferromagnetism of the sample even at room temperature. The saturation magnetic moment (m_s) increases with decreasing temperature and is $\sim 1 \times 10^{-6}$ and 3.5×10^{-6} emu at 300 and 2 K, respectively. The average saturation magnetic moment per Pt atom is thus 0.03 μ_B/Pt at 300 K and 0.11 μ_B/Pt at 2 K. The coercive field (H_c) is found to be temperature independent, which is $\sim$300 Oe, as shown in the inset of Fig. 5.8.
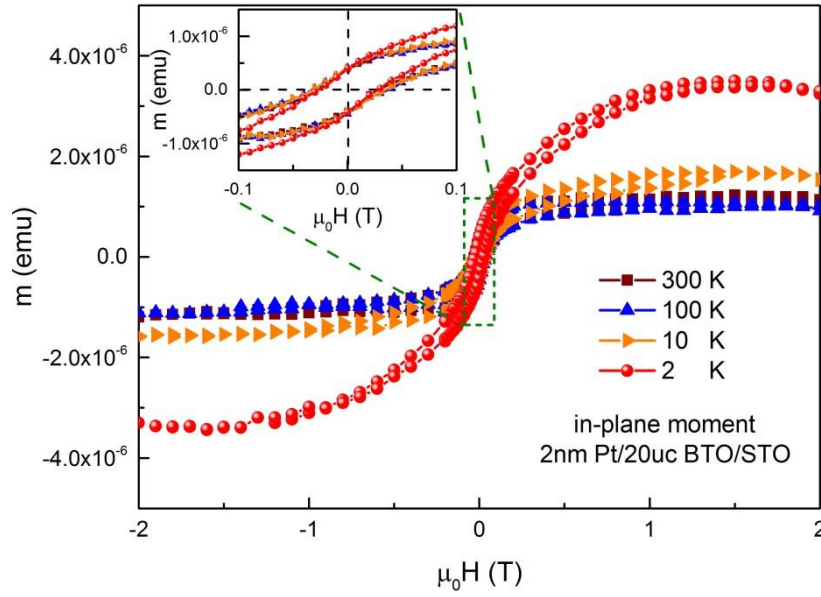
Figure 5.8 In-plane magnetic moment dependence on magnetic field for 2 nm Pt/20 uc BTO/STO from -2 to 2 T at different temperatures. The inset shows magnetic moment dependence on magnetic field from -0.1 to 0.1 T.

5.7 First-principles calculations

To elucidate the mechanism for this unusual ferromagnetism in Pt, first-principles calculations were performed. For the appearance of ferromagnetism of Pt, two conditions must be satisfied: (i) depolarization field of BTO (ii) substitution of Ti by Pt at the Pt/BTO interface.

The simulation cell consists of Pt/BTO superlatice of TiO_2-terminated symmetric BTO and Pt with the interfacial Ti atom replaced by the Pt atom as shown in Fig. 5.9 (a). We use five layers of Pt and ten and half unit cells of BTO. The Pt atoms reside on the top of oxygen. When Pt completely covered BTO, *i.e.* a perfect Pt/BTO interface without any defect or the Ti substitution, the superlattice is nonmagnetic. Only after interfacial Ti is replaced by Pt, magnetization appears at the Pt/BTO interface. BTO remains polarized even after the Pt substitution of Ti at the interface. We define the lower and upper Pt/BTO interfaces as I_1 and I_2, respectively, as shown in Fig. 5.9 (a). Figure

128

5.9 (b) shows Ti-O and Ba-O displacement plotted as function of distance from interface I_1 to I_2. At both interfaces, the displacements are positive, suggesting a polarization pointing to I_2. The resulting depolarizing field leads to electron accumulation at I_2 and depletion at I_1. The resulting electron redistribution leads to increase in density of states at Fermi level at the I_1 interface.

Substitutional Pt on the interfacial Ti site leads to itinerant magnetism in Pt/BTO heterostructure. The non-spin polarized density of state of Pt at interface I_1 (Fig. 5.9 (c) top panel) have a peak at the Fermi energy, resulting large electronic interaction energy. According to Stoner model, the large electronic interaction energy is reduced by spin splitting of bands. Even though such splitting leads to increase in band energy, the gain by exchange energy leads to stabilization of the magnetic system. The well-known Stoner criterion for ferromagnetism $I\rho(E_F)>1$, is satisfied for such enhanced density of states at interface I_1 as we find $I\rho(E_F) =1.02 >1$, here I is the stoner exchange parameter and $\rho(E_F)$ is the density of states at the Fermi level. We use I=0.37 calculated for the bulk Pt. This suggests the existence of itinerant ferromagnetism at Pt/BTO interface.

In Fig. 5.9 (c) (middle and bottom panel), we show the calculated density of states taking into account the full spin polarization. The bands are indeed exchange split with the splitting of $\Delta \sim 0.03$ eV. Such splitting makes the system magnetic. By using the calculated Stoner exchange parameter for bulk Pt, we expect magnetic moment of $m = \frac{\Delta}{I} \sim 0.07\,\mu_B$ in the Pt/BTO heterostructure. In our full spin polarized calculation we find the overall

magnetic moment of ~0.13 μ_B with the moment of ~0.05 μ_B located at the substituted Pt site at the interface consistent with the Stoner model for itinerant magnets. The in-plane oxygen bonded with the Pt also gets magnetized with moment ~0.03 μ_B, while the other ions/atoms in the heterostructure are nonmagnetic. It should be noted that the calculated overall magnetic moment (~ 0.13 μ_B) is in good agreement with our magnetic measurements shown in Fig. 5.8.

We note that although Pt is a noble metal, and thus, inert to chemical environment. We found that there is a sizable bonding between Pt and surrounding oxygens, which makes our model plausible. In industry, Pt is often used as automobile catalysts to oxidize carbon monoxide. The oxidation activity of Pt is attributed to the presence of a superficial platinum oxide layer under oxygen-rich conditions [182]. This means that our assumption of a sizable bonding between Pt and surrounding oxygens is reasonable.

The atomic and electronic structure of the system are obtained using density functional theory (DFT) as implemented in Vienna *ab initio* simulation package (VASP) [147, 183]. The projected augmented plane wave (PAW) method is used to approximate the electron-ion potential [148]. The exchange and correlation potential is calculated in local density approximation (LDA). In the calculation, we use a kinetic cutoff energy of 340 eV for the plane wave expansion of the PAWs and 14×14×1 and grid of k points [184] for the Brillouin zone integration. The in-plane lattice constant is fixed to that of SrTiO$_3$ substrate. The c/a ratio and the internal atomic coordinates are relaxed until the Hellman-Feynman force on each atom is less then | 0.01| eV/Å.
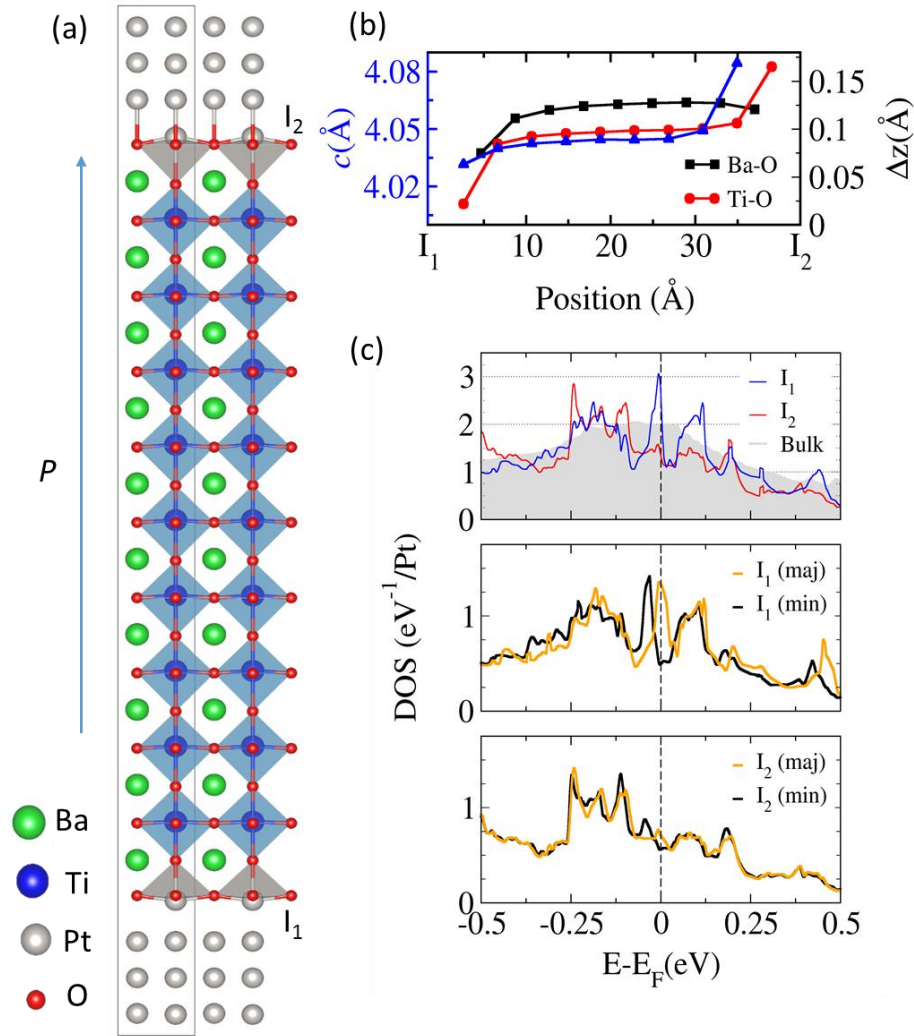
Figure 5.9 Structure and interfacial electronic structure of Pt/BTO superlatice. (a) The computational cell contains symmetric BTO cell with Pt covered on both sides. (b) Cation-anion displacement (ΔZ) and out of plane lattice constant of BTO plotted as a function of distance from I_1 to I_2 showing polarization pointing to I_2. (c) The non-magnetic density of states of interfacial substitutional Pt compared to that of bulk Pt (top panel), the majority and minority density of states of interfacial substitutional Pt at interface I_1 (middle panel) and I_2 (bottom panel). The in plane lattice constant in the calculation was fixed to that of substrate STO.

5.8 Numerical fitting of AHE

Having explained the origin of the induced ferromagnetism in Pt, we next turn to simulate the AHE data in Fig. 5.7 with classic Langevin function. The Hall resistance of a ferromagnetic metal is generally composed of two terms, viz.

$$R_H = R_H^0 + R_H^A \qquad \text{(eq. 5.1)}$$

where R_H^0 (which scales linearly with external magnetic field) and R_H^A are the ordinary Hall resistance and anomalous Hall resistance, respectively. Figure 5.10 shows the anomalous Hall resistance dependence on magnetic field for a 2 nm Pt/20 uc BTO/STO sample at different temperatures. The anomalous Hall resistance was obtained by subtracting the ordinary Hall resistance from the original data in Fig. 5.7. The ordinary Hall resistance was deduced by fitting the original data in Fig. 5.7 at high magnetic field with a linear function. One can see that R_H^A is negative at high temperature (>30 K) and positive at low temperature (<10 K). At 10 K, R_H^A has both negative and positive contributions. These results are strikingly similar to those reported in Ref. [179]. Here, we analyze our AHE data by using the three-component model proposed in Ref. [179]. In this model, R_H^A is assumed to be composed of two components, i.e. a negative component $R_H^{A^-}$ and a positive component $R_H^{A^+}$. So, R_H can be written as:

$$R_H = R_H^0 + R_H^A = R_H^0 + R_H^{A^-} + R_H^{A^+} \qquad \text{(eq. 5.2)}$$

In this model, it's assumed that $R_H^{A^-}$ is temperature independent, while $R_H^{A^+}$ is temperature dependent and plays a major role in determining R_H^A. The relation between the anomalous Hall resistance R_H^A and magnetization M can be written as:

$$R_H^A = \alpha M = \alpha N \frac{k_B T}{k_B T_F} \mu L(\frac{\mu H}{k_B T}) = \alpha N \frac{k_B T}{k_B T_F} \mu [\coth\left(\frac{\mu H}{k_B T}\right) - \frac{k_B T}{\mu H}] \quad \text{(eq.5.3)}$$

where α is the extraordinary Hall coefficient, N is the number of magnetic moments per unit volume, k_B is Boltzmann constant, T is temperature, T_F is

Fermi temperature, μ is the magnitude of the magnetic moments, $L(x)$ is

Langevin function and H is magnetic field. We note here that the term $\frac{k_B T}{k_B T_F}$

appears because that, in itinerant electron systems, only the electrons on the

Fermi surface within energy range $\sim k_B T$ will respond to the magnetic field.

Hence the total number of electrons contributing to M is reduced by the factor

$\frac{k_B T}{k_B T_F}$. To fit the anomalous Hall resistance R_H^A at different temperatures, for

example at 2.5 K, we define ΔR_H as:

$$\Delta R_H = R_H^A(2.5\text{ K}) - R_H^A(150\text{ K}) \sim R_H^{A^+}(2.5\text{ K}) - R_H^{A^+}(150\text{ K}) =$$

$$\alpha[M(2.5\text{ K}) - M(150\text{ K})] = \alpha\Delta M \qquad\qquad \text{(eq. 5.4)}$$

where ΔM is the difference between the magnetizations at 2.5 and 150 K,

respectively.

Figure 5.11 shows ΔR_H dependence on magnetic field for a 2 nm Pt/20 uc

BTO/STO sample at different temperatures. One can see that the experimental

data can be well fitted with eq. 5.4, except at the lowest temperature 2.5 K.

This deviation might be caused by the exchange interaction between induced

magnetic moments at low temperature. The exchange interaction was

neglected in eq. 5.4. During the fitting, we fixed the magnitude of the

magnetic moments μ to 8 μ_B/Pt, set the number of magnetic moments per unit

volume N to a fix value and allowed the extraordinary Hall coefficient α to

change. We note that at 2.5 K, the estimated μ from the fitting (8 μ_B/Pt) seems

significantly larger than the average magnetic moment deduced from SQUID

measurements (0.11 μ_B/Pt). However, this is reasonable as we have explained

that only the Pt atoms which replaced Ti at the Pt/BTO interface are magnetized.
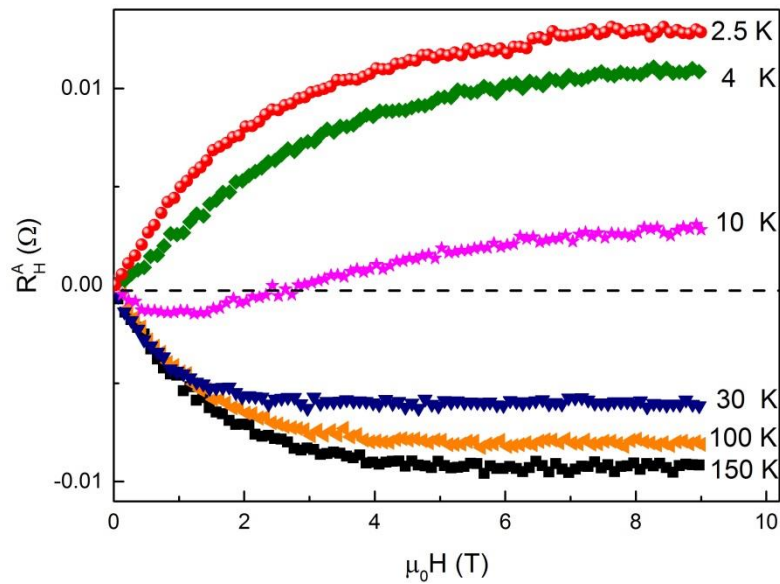
Figure 5.10 Anomalous Hall resistance dependence on magnetic field for a 2 nm Pt/20 uc BTO/STO sample at different temperatures.
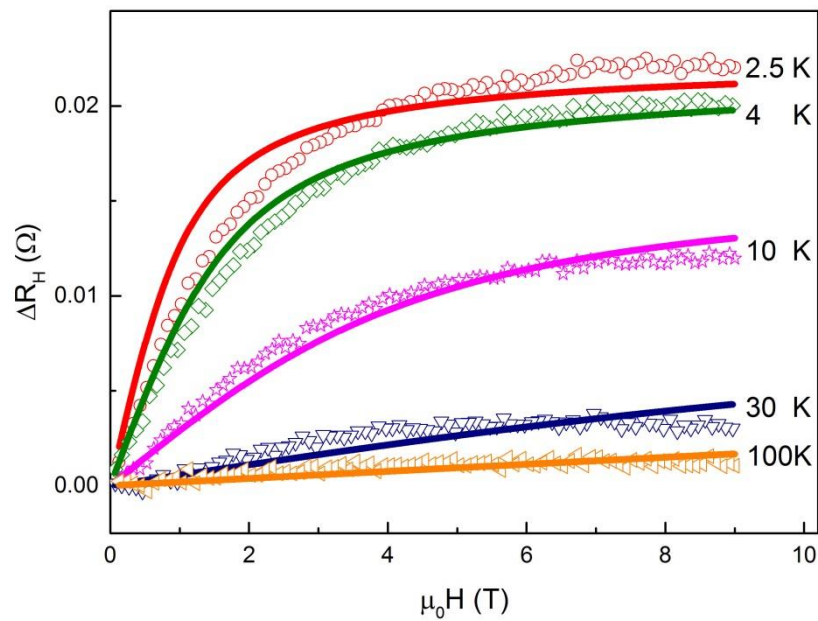
Figure 5.11 Numerical fitting of the anomalous Hal resistance with the Langevin function at different temperatures for a 2 nm Pt/20 uc BTO/STO sample. The hollow symbols represent experimental data, while the solid lines represent fitting data with eq. 5.4. Different colors stand for different temperatures.

5.9 Pt thickness dependence of AHE

Next, we study the AHE with different Pt thickness, while keeping BTO at 20 uc. Figure 5.12 (a) and (c) show AHE for 3 nm Pt/20 uc BTO/STO and 4 nm Pt/20 uc BTO/STO, respectively. As can be seen, the magnitude of AHE is much smaller in 3 nm Pt/20 uc BTO/STO and 4 nm Pt/20 uc BTO/STO, as compared to that of 2 nm Pt/20 uc BTO/STO shown in Fig. 5.7 (b). Nevertheless, the sign reversal of AHE can still be observed at low temperature (for example, 2.5 K). The 3 nm Pt/STO and 4 nm Pt/STO samples show normal Hall effect, as shown in Fig. 5.12 (b) and (d).

In Fig. 5.13, we show the anomalous Hall resistance (R_H^A) dependence on temperature $(R_H^A - T)$ for the Pt/20 uc BTO/STO samples with 2, 3 and 4 nm Pt. As can be seen, R_H^A is negative at high temperature and becomes positive at low temperature for all the samples. Moreover, the magnitude of R_H^A decreases quickly with increasing Pt thickness, indicating that the effect is an interface effect. These results are very similar to those reported in Ref. [178] and [179]. In addition, the $R_H^A - T$ curves recalls the Curie-like temperature dependence of magnetization, providing further evidence for ferromagnetism in Pt.

Here, we comment on the negative anomalous Hall resistance $R_H^{A^-}$. As pointed out in Ref. [179] and also in our data, $R_H^{A^-}$ seems fairly temperature independent, at least above 100 K (Fig. 5.13). However, the origin of $R_H^{A^-}$ can not be determined by our work here and we leave it as an open question.
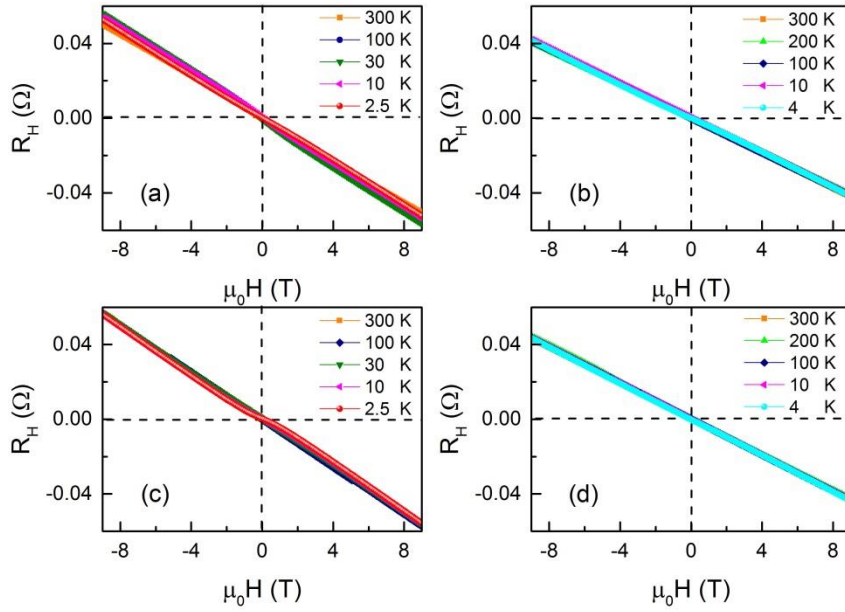
Figure 5.12 Hall resistance dependence on magnetic field for 3 nm Pt/20 uc BTO/STO (a), 3 nm Pt/STO (b), 4 nm Pt/20 uc BTO/STO (c) and 4nm Pt/STO (d), respectively. Different colors represent different temperatures.
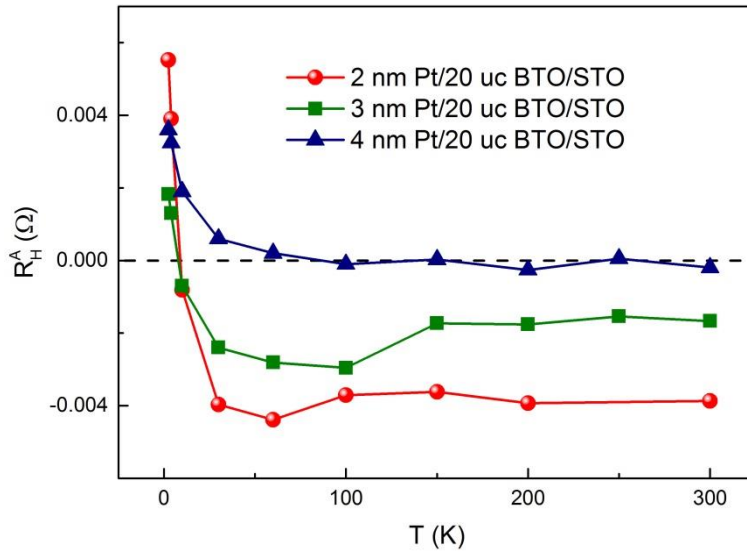
Figure 5.13 Extracted anomalous Hall resistance dependence on temperature for Pt/20 uc BTO/STO samples with 2 nm, 3 nm and 4 nm Pt, respectively.

5.10 Summary

In conclusion, we have observed AHE in a Pt/BTO/STO heterostructure. The AHE is attributed to the ferromagnetism of Pt. From the SQUID measurement, the average magnetic moment of Pt at 300 K is determined to be ~0.03 μ_B/Pt.

Both the depolarization of BTO and the interfacial substitution of Ti by Pt are essential for the appearance of ferromagnetism in Pt.

Our work provides a routine to induce ferromagnetism in an otherwise paramagnetic material. This shall, in principle, add a new member to the multiferroic material family, as both ferroelectricity and ferromagnetism exist in the heterostructure. By switching the polarization direction of the $BaTiO_3$ layer, the magnetic properties of the Pt overlayer could be expected to be modulated. In addition, due to the nature of ferroelectricity, the modulation should be non-volatile. We also note that Pt is often used in ferroelectric tunneling junctions (FTJ) as a top electrode, for example $Pt/BaTiO_3/Nb:SrTiO_3$ [185]. Our finding could thus pave the way for possible multiferroic tunneling junctions (MFTJ) with Pt.

Author contributions:

W. X. Zhou, H. Wang and Ariando designed the experiment. W. X. Zhou and H. Wang prepared the samples. W. X. Zhou conducted the electronic and magnetic transport measurements, XRD and PFM measurements. W. X. Zhou, N. Bao and C. J. Li conducted the SQUID measurements. T. Paudel and Evgeny Y. Tsymbal conducted the DFT calculations. W. X. Zhou, C. J. Li and Ariando analyzed the data. S. W. Zeng, J. Zhou, Z. Huang, K. Han, T. Venkatesan, J. S. Chen joined the discussion.

Chapter 6 Summary and future work

6.1 Summary

In this section, I summarize the main results and their implications of the three projects, which were introduced in Chapter 3-5.

6.1.1 Electron-soft phonon scattering in *n*-type SrTiO$_3$

In this project, we studied the electronic transport properties in *n*-type SrTiO$_3$ (STO), which is the "silicon" of oxide electronics.

In both the three-dimensional electron liquid (3DEL) and two-dimensional electron liquid (2DEL) hosted by STO, electronic transport anomalies were observed at the cubic-to-tetragonal phase transition temperature (T_c) of STO. A small peak of the temperature dependent temperature coefficient of resistance (TCR) can be observed at T_c, regardless of the origin of the charge carriers, the dimension of the electron liquid and the crystalline direction. This TCR peak, which can be well fitted with the electron- Γ_{25} (111) soft phonon scattering, is caused by anomalies in both carrier density and carrier mobility, with the latter taking the dominant role. Our first-principles calculations show that the mobility anomaly is caused by effective mass enhancement of the electrons from cubic to tetragonal phase. Furthermore, we found that the magnitude of the anomaly decreases with increasing carrier density as a result of competing electron-electron and electron-soft phonon scattering.

Although there have been reports showing the electron-soft phonon scattering in La$_{1-x}$Sr$_x$MnO$_3$/SrTiO$_3$ heterostructure through interfacial coupling between the charge carriers in La$_{1-x}$Sr$_x$MnO$_3$ and the Γ_{25} (111) soft phonon STO [144]. As far as we know, our results explicitly show, for the first time, the electron

scattering by the Brillouin zone corner Γ_{25} (111) soft phonon in STO itself. Our results, which should improve our understanding of the electron-electron scattering and electron-phonon scattering in STO, highlight the importance of the electron-soft phonon scattering in STO. In addition, as the electron-soft phonon scattering has been applied to explain the mechanism of the superconductivity in STO, our work may also provide some insights into the superconductivity in STO [143].

6.1.2 Coexistence of ferroelectricity and two-dimensional electron gas

In this project, we studied the coexistence of ferroelectricity and two-dimensional electron gas (2DEG) in $Ba_xSr_{1-x}TiO_3$ thin films in a $LaAlO_3$/ $Ba_xSr_{1-x}TiO_3$/$SrTiO_3$ (LAO/BST/STO) heterostructure.

By using piezoresponse force microscopy (PFM), electronic and optical measurements, we observed systematic change of the transport properties of the 2DEG in LAO/BST/STO heterostructure. This systematic change is attributed to the competition between the built-in electric field of LAO and the depolarization field of BST. This competition signifies the coexistence of ferroelectricity and 2DEG in this heterostructure. Furthermore, through first-principles calculations, we showed layer-resolved carrier density and ferroelectricity in BST.

On the other hand, the LAO/BST/STO heterostructure can be used to tune the electronic transport properties of the 2DEG by changing the BST thickness. As shown in Chapter 4, clear electric field effect has been observed in LAO/BST/STO heterostructure with different BST thicknesses. These results

suggest that, by inserting a ferroelectric BST layer between LAO and STO, the electronic transport properties of the 2DEG can be systematically tuned.

6.1.3 Ferroelectricity induced ferromagnetism in paramagnetic Pt thin films

In this project, we found unusual room-temperature ferromagnetism in Pt thin films in a Pt/BaTiO$_3$/SrTiO$_3$ (Pt/BTO/STO) heterostructure. The ferromagnetism was evidenced by anomalous Hall effect (AHE), magnetic measurements and first-principles calculations. The average magnetic moment was found to be ~0.03 μ_B/Pt at 300 K. The origin of the ferromagnetism is the depolarization field of BTO and the interfacial substitution of Ti with Pt.

Our work provides a routine to induce ferromagnetism in an otherwise paramagnetic material. This routine can be used to induce ferromagnetism in other paramagnetic materials as well, such as Pd. We also note that Pt is often used in ferroelectric tunneling junctions (FTJ) as a top electrode, for example Pt/BaTiO$_3$/Nb:SrTiO$_3$ [185], our finding could thus pave the way for possible multiferroic tunneling junctions (MFTJ) with Pt.

6.2 Future work

6.2.1 Electron-soft phonon scattering in *n*-type SrTiO$_3$

In the future, it would be interesting if we could do first-principles calculations on the electron-soft phonon scattering in *n*-type STO by considering all the electrons from different conduction bands and phonons from different branches. This shall give us a comprehensive picture of the conduction mechanism of *n*-type STO and the role of the electron-soft phonon scattering in the overall electron-electron and electron-phonon scattering in STO.

6.2.2 Coexistence of ferroelectricity and two-dimensional electron gas

In the future, we plan to switch the polarization direction of the BST layer in LAO/BST/STO heterostructure. This switching may significantly influence the conductivity of the 2DEG, leading to a high-resistance state and a low-resistance state depending on the different polarization direction of the BST layer. Furthermore, this switching should be non-volatile due to the nature of ferroelectricity. This switching experiment may be realized by using Nb:STO as the substrate instead of STO. Nb:STO has the same lattice constant as that of STO and can be used as the bottom electrode in the switching experiment. Thus, in this LAO/BST/Nb:STO heterostruture, we may construct a ferroelectric field effect transistor, which might be useful for future applications.

6.2.3 Ferroelectricity induced ferromagnetism in paramagnetic Pt thin films

To further expand our approach to induce ferromagnetism in non-magnetic materials with ferroelectricity, we would like to study the magnetic proeperties of Pd thin films in a $Pd/BaTiO_3/SrTiO_3$ heterostructure. As Pd and Pt have very similar magnetic properties, the approach proposed in Chapter 5 might also induce ferromagnetism in Pd in a $Pd/BaTiO_3/SrTiO_3$ heterostructure.

On the other hand, we can do ionic liquid gating experiment in Pt/BTO/STO heterostructure. In this way, the magnetic properties of Pt can be modulated with two electric fields (one electric field comes from BTO, while the other electric field comes from the ionic liquid gating). Ionic liquid gating provides an additional electric field to the system. This electric field can be used to enhance or weaken the induced ferromagnetism in Pt.

In addition, it would be of great interest if one can construct a MFTJ with a Pt/BaTiO$_3$/Nb:SrTiO$_3$ heterostructure. This can be realized by switching the spin polarization with external magnetic field and switching the ferroelectric polarization with external electric field while measuring the tunneling resistance. However, this might be very challenging as the small magnetic moment (~ 0.05 μ_B/Pt) may not give any measurable TMR change.

REFERENCES

[1] G.E. Moore, Cramming more components onto integrated circuits, *Proceedings of the IEEE*, 86 (1998) 82-85.

[2] W.P. Halperin, Quantum size effects in metal particles, *Reviews of Modern Physics*, 58 (1986) 533-606.

[3] http://en.wikipedia.org/wiki/Moore's_law.

[4] I. Žutić, J. Fabian, S. Das Sarma, Spintronics: Fundamentals and applications, *Reviews of Modern Physics*, 76 (2004) 323-410.

[5] T.D. Ladd, F. Jelezko, R. Laflamme, Y. Nakamura, C. Monroe, J.L. O'Brien, Quantum computers, *Nature*, 464 (2010) 45-53.

[6] C.X.F. Lam, X.M. Mo, S.H. Teoh, D.W. Hutmacher, Scaffold development using 3D printing with a starch-based polymer, *Materials Science and Engineering: C*, 20 (2002) 49-56.

[7] J.J. Gu, Y.Q. Liu, Y.Q. Wu, R. Colby, R.G. Gordon, P.D. Ye, First experimental demonstration of gate-all-around III-V MOSFETs by top-down approach, *Electron Devices Meeting (IEDM), 2011 IEEE International*, 2011, pp. 33.2.1-33.2.4.

[8] H.Y. Hwang, Y. Iwasa, M. Kawasaki, B. Keimer, N. Nagaosa, Y. Tokura, Emergent phenomena at oxide interfaces, *Nat Mater*, 11 (2012) 103-113.

[9] Y. Tokura, H.Y. Hwang, Condensed-matter physics: Complex oxides on fire, *Nat Mater*, 7 (2008) 694-695.

[10] J. Mannhart, D.G. Schlom, Oxide interfaces-an opportunity for electronics, *Science*, 327 (2010) 1607-1611.

[11] K. Nomura, H. Ohta, K. Ueda, T. Kamiya, M. Hirano, H. Hosono, Thin-film transistor fabricated in single-crystalline transparent oxide semiconductor, *Science*, 300 (2003) 1269-1272.

[12] http://www.sharpusa.com/ForHome/HomeEntertainment/LCDTV/igzo.aspx

[13] N. Izyumskaya, Y.I. Alivov, S.J. Cho, H. Morkoç, H. Lee, Y.S. Kang, Processing, structure, properties, and applications of PZT Thin Films, *Critical Reviews in Solid State and Materials Sciences*, 32 (2007) 111-202.

[14] L. Yu, A.S. Nagra, E.G. Erker, P. Periaswamy, T.R. Taylor, J. Speck, R.A. York, $BaSrTiO_3$ interdigitated capacitors for distributed phase shifter applications, *IEEE Microwave and Guided Wave Letters*, 10 (2000) 448-450.

[15] K. van Benthem, C. Elsasser, R.H. French, Bulk electronic structure of $SrTiO_3$: Experiment and theory, *Journal of Applied Physics*, 90 (2001) 6156-6164.

[16] J.F. Scott, Soft-mode spectroscopy: Experimental studies of structural phase transitions, *Reviews of Modern Physics*, 46 (1974) 83-128.

[17] L.F. Mattheis, Effect of 110 K phase transition on $SrTiO_3$ conduction bands, *Physical Review B*, 6 (1972) 4740-4753.

[18] F. El-Mellouhi, E.N. Brothers, M.J. Lucero, G.E. Scuseria, Modeling of the cubic and antiferrodistortive phases of $SrTiO_3$ with screened hybrid density functional theory, *Physical Review B*, 84 (2011) 115122.

[19] H.P.R. Frederikse, W.R. Thurber, W.R. Hosler, Electronic transport in strontium titanate, *Physical Review*, 134 (1964) A442-A445.

[20] D. van der Marel, J.L.M. van Mechelen, Mazin, II, Common Fermi-liquid origin of T^2 resistivity and superconductivity in *n*-type $SrTiO_3$, *Physical Review B*, 84 (2011).

[21] D.S. Kan, T. Terashima, R. Kanda, A. Masuno, K. Tanaka, S.C. Chu, H. Kan, A. Ishizumi, Y. Kanemitsu, Y. Shimakawa, M. Takano, Blue-light emission at room temperature from Ar^+-irradiated $SrTiO_3$, *Nature Materials*, 4 (2005) 816-819.

[22] J.F. Schooley, W.R. Hosler, M.L. Cohen, Superconductivity in semiconducting $SrTiO_3$, *Physical Review Letters*, 12 (1964) 474.

[23] S.H. Wemple, M. DiDomenico, A. Jayaraman, Electron scattering in perovskite-oxide ferroelectric semiconductors, *Physical Review*, 180 (1969) 547-556.

[24] J.L.M. van Mechelen, D. van der Marel, C. Grimaldi, A.B. Kuzmenko, N.P. Armitage, N. Reyren, H. Hagemann, Mazin, II, Electron-phonon interaction and charge carrier mass enhancement in $SrTiO_3$, *Physical Review Letters*, 100 (2008).

[25] S.N. Klimin, J. Tempere, D. van der Marel, J.T. Devreese, Microscopic mechanisms for the Fermi-liquid behavior of Nb-doped strontium titanate, *Physical Review B*, 86 (2012) 8.

[26] A. Spinelli, M.A. Torija, C. Liu, C. Jan, C. Leighton, Electronic transport in doped $SrTiO_3$: Conduction mechanisms and potential applications, *Physical Review B*, 81 (2010).

[27] X. Lin, B. Fauqué, K. Behnia, Scalable T^2 resistivity in a small single-component Fermi surface, *Science*, 349 (2015) 945-948.

[28] W.G. Baber, The contribution to the electrical resistance of metals from collisions between electrons, *Proceedings of the Royal Society of London Series a-Mathematical and Physical Sciences*, 158 (1937) 0383-0396.

[29] H.P.R. Frederikse, W.R. Hosler, Hall mobility in $SrTiO_3$, *Physical Review*, 161 (1967) 822.

[30] Z.Q. Liu, C.J. Li, W.M. Lü, X.H. Huang, Z. Huang, S.W. Zeng, X.P. Qiu, L.S. Huang, A. Annadi, J.S. Chen, J.M.D. Coey, T. Venkatesan, Ariando, Origin of the two-dimensional electron gas at $LaAlO_3$/$SrTiO_3$ interfaces: The role of oxygen vacancies and electronic reconstruction, *Physical Review X*, 3 (2013).

[31] A. Kalabukhov, R. Gunnarsson, J. Borjesson, E. Olsson, T. Claeson, D. Winkler, Effect of oxygen vacancies in the $SrTiO_3$ substrate on the electrical properties of the $LaAlO_3$/$SrTiO_3$ interface, *Physical Review B*, 75 (2007) 121404(R).

[32] J.M.D. Coey, Magnetism and magnetic materials, *Cambridge University Press*, 2010.

[33] M. Lee, J.R. Williams, S. Zhang, C.D. Frisbie, D. Goldhaber-Gordon, Electrolyte gate-controlled Kondo effect in $SrTiO_3$, *Physical Review Letters*, 107 (2011) 256601.

[34] P. Moetakef, J.R. Williams, D.G. Ouellette, A.P. Kajdos, D. Goldhaber-Gordon, S.J. Allen, S. Stemmer, Carrier-controlled ferromagnetism in $SrTiO_3$, *Physical Review X*, 2 (2012) 021014.

[35] Z.Q. Liu, W.M. Lü, S.L. Lim, X.P. Qiu, N.N. Bao, M. Motapothula, J.B. Yi, M. Yang, S. Dhar, T. Venkatesan, Ariando, Reversible room-temperature ferromagnetism in Nb-doped $SrTiO_3$ single crystals, *Physical Review B*, 87 (2013) 220405.

[36] I.R. Shein, A.L. Ivanovskii, First principle prediction of vacancy-induced magnetism in non-magnetic perovskite $SrTiO_3$, *Physics Letters A*, 371 (2007) 155-159.

[37] Y. Zhang, J. Hu, E. Cao, L. Sun, H. Qin, Vacancy induced magnetism in $SrTiO_3$, *Journal of Magnetism and Magnetic Materials*, 324 (2012) 1770-1775.

[38] D.G. Schlom, L.-Q. Chen, X. Pan, A. Schmehl, M.A. Zurbuchen, A thin film approach to engineering functionality into oxides, *Journal of the American Ceramic Society*, 91 (2008) 2429-2454.

[39] M. Kawasaki, K. Takahashi, T. Maeda, R. Tsuchiya, M. Shinohara, O. Ishiyama, T. Yonezawa, M. Yoshimoto, H. Koinuma, Atomic control of the $SrTiO_3$ crystal surface, *Science*, 266 (1994) 1540-1542.

[40] G. Koster, B.L. Kropman, G. Rijnders, D.H.A. Blank, H. Rogalla, Quasi-ideal strontium titanate crystal surfaces through formation of strontium hydroxide, *Applied Physics Letters*, 73 (1998) 2920-2922.

[41] W. Cochran, Crystal stability and the theory of ferroelectricity, *Advances in Physics*, 9 (1960) 387-423.

[42] R.E. Cohen, Origin of ferroelectricity in perovskite oxides, *Nature*, 358 (1992) 136-138.

[43] Y. Wang, X. Liu, J.D. Burton, S.S. Jaswal, E.Y. Tsymbal, Ferroelectric instability under screened Coulomb interactions, *Physical Review Letters*, 109 (2012) 247601.

[44] S.H. Wemple, Polarization fluctuations and the optical-absorption edge in $BaTiO_3$, *Physical Review B*, 2 (1970) 2679-2689.

[45] T. Kolodiazhnyi, M. Tachibana, H. Kawaji, J. Hwang, E. Takayama-Muromachi, Persistence of ferroelectricity in $BaTiO_3$ through the Iinsulator-metal transition, *Physical Review Letters*, 104 (2010).

[46] Y. Luspin, J.L. Servoin, F. Gervais, Soft mode spectroscopy in barium titanate, *Journal of Physics C: Solid State Physics*, 13 (1980) 3761.

[47] A.A. Sirenko, C. Bernhard, A. Golnik, A.M. Clark, J. Hao, W. Si, X.X. Xi, Soft-mode hardening in $SrTiO_3$ thin films, *Nature*, 404 (2000) 373-376.

[48] D. Fu, M. Itoh, Role of Ca off-centering in tuning the ferroelectric phase transitions in $Ba(Zr,Ti)O_3$ system, arXiv:1503.00406

[49] B. Zalar, V.V. Laguta, R. Blinc, NMR evidence for the coexistence of order-disorder and displacive components in barium titanate, *Physical Review Letters*, 90 (2003) 037601.

[50] J. Hlinka, T. Ostapchuk, D. Nuzhnyy, J. Petzelt, P. Kuzel, C. Kadlec, P. Vanek, I. Ponomareva, L. Bellaiche, Coexistence of the phonon and relaxation soft modes in the terahertz dielectric response of tetragonal $BaTiO_3$, *Physical Review Letters*, 101 (2008) 167402.

[51] R. Comes, M. Lambert, A. Guinier, The chain structure of $BaTiO_3$ and $KNbO_3$, *Solid State Communications*, 6 (1968) 715-719.

[52] D. Lee, H. Lu, Y. Gu, S.-Y. Choi, S.-D. Li, S. Ryu, T.R. Paudel, K. Song, E. Mikheev, S. Lee, S. Stemmer, D.A. Tenne, S.H. Oh, E.Y. Tsymbal, X. Wu, L.-Q. Chen, A. Gruverman, C.B. Eom, Emergence of room-temperature ferroelectricity at reduced dimensions, *Science*, 349 (2015) 1314-1317.

[53] J.H. Haeni, P. Irvin, W. Chang, R. Uecker, P. Reiche, Y.L. Li, S. Choudhury, W. Tian, M.E. Hawley, B. Craigo, A.K. Tagantsev, X.Q. Pan, S.K. Streiffer, L.Q. Chen, S.W. Kirchoefer, J. Levy, D.G. Schlom, Room-temperature ferroelectricity in strained $SrTiO_3$, *Nature*, 430 (2004) 758-761.

[54] H.W. Jang, A. Kumar, S. Denev, M.D. Biegalski, P. Maksymovych, C.W. Bark, C.T. Nelson, C.M. Folkman, S.H. Baek, N. Balke, C.M. Brooks, D.A. Tenne, D.G. Schlom, L.Q. Chen, X.Q. Pan, S.V. Kalinin, V. Gopalan, C.B. Eom, Ferroelectricity in strain-free $SrTiO_3$ thin films, *Physical Review Letters*, 104 (2010).

[55] K.J. Choi, M. Biegalski, Y.L. Li, A. Sharan, J. Schubert, R. Uecker, P. Reiche, Y.B. Chen, X.Q. Pan, V. Gopalan, L.Q. Chen, D.G. Schlom, C.B. Eom, Enhancement of ferroelectricity in strained $BaTiO_3$ thin films, *Science*, 306 (2004) 1005-1009.

[56] A.R. Damodaran, E. Breckenfeld, Z. Chen, S. Lee, L.W. Martin, Enhancement of ferroelectric Curie temperature in $BaTiO_3$ films via strain-induced defect dipole alignment, *Advanced Materials*, 26 (2014) 6341-6347.

[57] A. Ohtomo, H.Y. Hwang, A high-mobility electron gas at the $LaAlO_3/SrTiO_3$ heterointerface, *Nature*, 427 (2004) 423-426.

[58] X.R. Wang, C.J. Li, W.M. Lü, T.R. Paudel, D.P. Leusink, M. Hoek, N. Poccia, A. Vailionis, T. Venkatesan, J.M.D. Coey, E.Y. Tsymbal, Ariando, H. Hilgenkamp, Imaging and control of ferromagnetism in $LaMnO_3/SrTiO_3$ heterostructures, *Science*, 349 (2015) 716-719.

[59] S. Dong, R. Yu, S. Yunoki, G. Alvarez, J.M. Liu, E. Dagotto, Magnetism, conductivity, and orbital order in $(LaMnO_3)_{2n}/(SrMnO_3)_n$ superlattices, *Physical Review B*, 78 (2008) 201102.

[60] J. Chrosch, E.K.H. Salje, Temperature dependence of the domain wall width in LaAlO$_3$, *Journal of Applied Physics*, 85 (1999) 722-727.

[61] S.A. Hayward, S.A.T. Redfern, E.K.H. Salje, Order parameter saturation in LaAlO$_3$, *Journal of Physics: Condensed Matter*, 14 (2002) 10131.

[62] Z. Huang, X.R.S. Wang, Z.Q. Liu, W.M. Lu, S.W. Zeng, A. Annadi, W.L. Tan, X.P. Qiu, Y.L. Zhao, M. Salluzzo, J.M.D. Coey, T. Venkatesan, Ariando, Conducting channel at the LaAlO$_3$/SrTiO$_3$ interface, *Physical Review B*, 88 (2013).

[63] S. Thiel, G. Hammerl, A. Schmehl, C.W. Schneider, J. Mannhart, Tunable quasi-two-dimensional electron gases in oxide heterostructures, *Science*, 313 (2006) 1942-1945.

[64] N. Reyren, S. Thiel, A.D. Caviglia, L.F. Kourkoutis, G. Hammerl, C. Richter, C.W. Schneider, T. Kopp, A.S. Ruetschi, D. Jaccard, M. Gabay, D.A. Muller, J.M. Triscone, J. Mannhart, Superconducting interfaces between insulating oxides, *Science*, 317 (2007) 1196-1199.

[65] A. Brinkman, M. Huijben, M. Van Zalk, J. Huijben, U. Zeitler, J.C. Maan, W.G. Van der Wiel, G. Rijnders, D.H.A. Blank, H. Hilgenkamp, Magnetic effects at the interface between non-magnetic oxides, *Nature Materials*, 6 (2007) 493-496.

[66] L. Li, C. Richter, J. Mannhart, R.C. Ashoori, Coexistence of magnetic order and two-dimensional superconductivity at LaAlO$_3$/SrTiO$_3$ interfaces, *Nature Physics*, 7 (2011) 762-766.

[67] J.A. Bert, B. Kalisky, C. Bell, M. Kim, Y. Hikita, H.Y. Hwang, K.A. Moler, Direct imaging of the coexistence of ferromagnetism and superconductivity at the LaAlO$_3$/SrTiO$_3$ interface, *Nat Phys*, 7 (2011) 767-771.

[68] Ariando, X. Wang, G. Baskaran, Z.Q. Liu, J. Huijben, J.B. Yi, A. Annadi, A.R. Barman, A. Rusydi, S. Dhar, Y.P. Feng, J. Ding, H. Hilgenkamp, T. Venkatesan, Electronic phase separation at the LaAlO$_3$/SrTiO$_3$ interface, *Nature Communications*, 2 (2011).

[69] D.A. Dikin, M. Mehta, C.W. Bark, C.M. Folkman, C.B. Eom, V. Chandrasekhar, Coexistence of superconductivity and ferromagnetism in two dimensions, *Physical Review Letters*, 107 (2011) 056802.

[70] A.D. Caviglia, S. Gariglio, C. Cancellieri, B. Sacépé, A. Fête, N. Reyren, M. Gabay, A.F. Morpurgo, J.M. Triscone, Two-dimensional quantum oscillations of the conductance at LaAlO$_3$/SrTiO$_3$ interfaces, *Physical Review Letters*, 105 (2010) 236802.

[71] M. Ben Shalom, A. Ron, A. Palevski, Y. Dagan, Shubnikov-De Haas oscillations in SrTiO$_3$/ LaAlO$_3$ interface, *Physical Review Letters*, 105 (2010) 206401.

[72] A.D. Caviglia, M. Gabay, S. Gariglio, N. Reyren, C. Cancellieri, J.M. Triscone, Tunable Rashba spin-orbit interaction at oxide interfaces, *Physical Review Letters*, 104 (2010) 126803.

[73] M. Ben Shalom, M. Sachs, D. Rakhmilevitch, A. Palevski, Y. Dagan, Tuning spin-orbit coupling and superconductivity at the SrTiO$_3$/LaAlO$_3$ interface: A magnetotransport study, *Physical Review Letters*, 104 (2010) 126802.

[74] N. Nakagawa, H.Y. Hwang, D.A. Muller, Why some interfaces cannot be sharp, *Nature Materials*, 5 (2006) 204-209.

[75] L. Yu, A. Zunger, A polarity-induced defect mechanism for conductivity and magnetism at polar–nonpolar oxide interfaces, *Nat Commun*, 5 (2014).

[76] Y. Segal, J.H. Ngai, J.W. Reiner, F.J. Walker, C.H. Ahn, X-ray photoemission studies of the metal-insulator transition in LaAlO$_3$/SrTiO$_3$ structures grown by molecular beam epitaxy, *Physical Review B*, 80 (2009) 241107.

[77] P.R. Willmott, S.A. Pauli, R. Herger, C.M. Schlepütz, D. Martoccia, B.D. Patterson, B. Delley, R. Clarke, D. Kumah, C. Cionca, Y. Yacoby, Structural basis for the

conducting interface between $LaAlO_3$ and $SrTiO_3$, *Physical Review Letters*, 99 (2007) 155502.

[78] http://volga.eng.yale.edu/index.php/FlashDrives/MethodsAndMaterials

[79] C. Bell, S. Harashima, Y. Kozuka, M. Kim, B.G. Kim, Y. Hikita, H.Y. Hwang, Dominant mobility modulation by the electric field effect at the $LaAlO_3$/$SrTiO_3$ interface, *Physical Review Letters*, 103 (2009).

[80] A.D. Caviglia, S. Gariglio, N. Reyren, D. Jaccard, T. Schneider, M. Gabay, S. Thiel, G. Hammerl, J. Mannhart, J.M. Triscone, Electric field control of the $LaAlO_3$/$SrTiO_3$ interface ground state, *Nature*, 456 (2008) 624-627.

[81] M. Hosoda, Y. Hikita, H.Y. Hwang, C. Bell, Transistor operation and mobility enhancement in top-gated $LaAlO_3$/$SrTiO_3$ heterostructures, *Applied Physics Letters*, 103 (2013) 103507.

[82] C. Cen, S. Thiel, G. Hammerl, C.W. Schneider, K.E. Andersen, C.S. Hellberg, J. Mannhart, J. Levy, Nanoscale control of an interfacial metal-insulator transition at room temperature, *Nat Mater*, 7 (2008) 298-302.

[83] C. Cen, S. Thiel, J. Mannhart, J. Levy, Oxide nanoelectronics on demand, *Science*, 323 (2009) 1026-1030.

[84] G. Cheng, P.F. Siles, F. Bi, C. Cen, D.F. Bogorin, C.W. Bark, C.M. Folkman, J.-W. Park, C.-B. Eom, G. Medeiros-Ribeiro, J. Levy, Sketched oxide single-electron transistor, *Nat Nano*, 6 (2011) 343-347.

[85] S. Zeng, W. Lü, Z. Huang, Z. Liu, K. Han, K. Gopinadhan, C. Li, R. Guo, W. Zhou, H.H. Ma, L. Jian, T. Venkatesan, Ariando, Liquid-gated high mobility and quantum oscillation of the two-dimensional electron gas at an oxide interface, *ACS Nano*, 10 (2016) 4532-4537.

[86] W.-N. Lin, J.-F. Ding, S.-X. Wu, Y.-F. Li, J. Lourembam, S. Shannigrahi, S.-J. Wang, T. Wu, Electrostatic modulation of $LaAlO_3$/$SrTiO_3$ interface transport in an electric double-layer transistor, *Advanced Materials Interfaces*, 1 (2014) 1300001.

[87] F. Bi, D.F. Bogorin, C. Cen, C.W. Bark, J.W. Park, C.B. Eom, J. Levy, "Water-cycle" mechanism for writing and erasing nanostructures at the $LaAlO_3$/$SrTiO_3$ interface, *Applied Physics Letters*, 97 (2010).

[88] S.-I. Kim, D.-H. Kim, Y. Kim, S.Y. Moon, M.-G. Kang, J.K. Choi, H.W. Jang, S.K. Kim, J.-W. Choi, S.-J. Yoon, H.J. Chang, C.-Y. Kang, S. Lee, S.-H. Hong, J.-S. Kim, S.-H. Baek, Non-volatile control of 2DEG conductivity at oxide interfaces, *Advanced Materials*, 25 (2013) 4612-4617.

[89] V.T. Tra, J.W. Chen, P.C. Huang, B.C. Huang, Y. Cao, C.H. Yeh, H.J. Liu, E.A. Eliseev, A.N. Morozovska, J.Y. Lin, Y.C. Chen, M.W. Chu, P.W. Chiu, Y.P. Chiu, L.Q. Chen, C.L. Wu, Y.H. Chu, Ferroelectric control of the conduction at the $LaAlO_3$/$SrTiO_3$ heterointerface, *Advanced Materials*, 25 (2013) 3357-3364.

[90] C. Mix, S. Finizio, M. Klaeui, G. Jakob, Conductance control at the $LaAlO_3$/$SrTiO_3$-interface by a multiferroic BiFeO3 ad-layer, *Applied Physics Letters*, 104 (2014).

[91] M.K. Niranjan, Y. Wang, S.S. Jaswal, E.Y. Tsymbal, Prediction of a switchable two-dimensional electron gas at ferroelectric oxide interfaces, *Physical Review Letters*, 103 (2009).

[92] Z. Zhang, P. Wu, L. Chen, J. Wang, First-principles prediction of a two dimensional electron gas at the $BiFeO_3$/$SrTiO_3$ interface, *Applied Physics Letters*, 99 (2011).

[93] K.D. Fredrickson, A.A. Demkov, Switchable conductivity at the ferroelectric interface: Nonpolar oxides, *Physical Review B*, 91 (2015).

[94] S. Nazir, M. Behtash, K. Yang, Towards enhancing two-dimensional electron gas quantum confinement effects in perovskite oxide heterostructures, *Journal of Applied Physics*, 117 (2015) 115305.

[95] Y.-Q. Gao, P. Li, N. Wang, H. Xing, C.-L. Chen, The ferroelectric field effect on the two-dimensional electron gas at LaAlO$_3$/SrTiO$_3$ (001) interface: Insights from first principle simulations, *Physica E: Low-dimensional Systems and Nanostructures*, 80 (2016) 195-201.

[96] A. Tebano, E. Fabbri, D. Pergolesi, G. Balestrino, E. Traversa, Room-temperature giant persistent photoconductivity in SrTiO$_3$/LaAlO$_3$ heterostructures, *Acs Nano*, 6 (2012) 1278-1283.

[97] C.W. Bark, D.A. Felker, Y. Wang, Y. Zhang, H.W. Jang, C.M. Folkman, J.W. Park, S.H. Baek, H. Zhou, D.D. Fong, X.Q. Pan, E.Y. Tsymbal, M.S. Rzchowski, C.B. Eom, Tailoring a two-dimensional electron gas at the LaAlO$_3$/SrTiO$_3$ (001) interface by epitaxial strain, *Proceedings of the National Academy of Sciences of the United States of America*, 108 (2011) 4720-4724.

[98] Y.J. Shi, S. Wang, Y. Zhou, H.F. Ding, D. Wu, Tuning the carrier density of LaAlO$_3$/SrTiO$_3$ interfaces by capping La$_{1-x}$Sr$_x$MnO$_3$, *Applied Physics Letters*, 102 (2013).

[99] Y.W. Xie, Y. Hikita, C. Bell, H.Y. Hwang, Control of electronic conduction at an oxide heterointerface using surface polar adsorbates, *Nature Communications*, 2 (2011).

[100] H. Ohno, D. Chiba, F. Matsukura, T. Omiya, E. Abe, T. Dietl, Y. Ohno, K. Ohtani, Electric-field control of ferromagnetism, *Nature*, 408 (2000) 944-946.

[101] C.H. Ahn, J.M. Triscone, J. Mannhart, Electric field effect in correlated oxide systems, *Nature*, 424 (2003) 1015-1018.

[102] V. Garcia, M. Bibes, L. Bocher, S. Valencia, F. Kronast, A. Crassous, X. Moya, S. Enouz-Vedrenne, A. Gloter, D. Imhoff, C. Deranlot, N.D. Mathur, S. Fusil, K. Bouzehouane, A. Barthelemy, Ferroelectric control of spin polarization, *Science*, 327 (2010) 1106-1110.

[103] D. Chiba, M. Sawicki, Y. Nishitani, Y. Nakatani, F. Matsukura, H. Ohno, Magnetization vector manipulation by electric fields, *Nature*, 455 (2008) 515-518.

[104] D. Chiba, S. Fukami, K. Shimamura, N. Ishiwata, K. Kobayashi, T. Ono, Electrical control of the ferromagnetic phase transition in cobalt at room temperature, *Nat Mater*, 10 (2011) 853-856.

[105] M. Weisheit, S. Fähler, A. Marty, Y. Souche, C. Poinsignon, D. Givord, Electric field-induced modification of magnetism in thin-film ferromagnets, *Science*, 315 (2007) 349-351.

[106] B. Cui, C. Song, G. Wang, Y. Yan, J. Peng, J. Miao, H. Mao, F. Li, C. Chen, F. Zeng, F. Pan, Reversible ferromagnetic phase transition in electrode-gated manganites, *Advanced Functional Materials*, 24 (2014) 7233-7240.

[107] H. Tanaka, J. Zhang, T. Kawai, Giant electric field modulation of double exchange ferromagnetism at room temperature in the perovskite manganite/titanate *p-n* junction, *Physical Review Letters*, 88 (2001) 027204.

[108] R.O. Cherifi, V. Ivanovskaya, L.C. Phillips, A. Zobelli, I.C. Infante, E. Jacquet, V. Garcia, S. Fusil, P.R. Briddon, N. Guiblin, A. Mougin, A.A. Ünal, F. Kronast, S. Valencia, B. Dkhil, A. Barthélémy, M. Bibes, Electric-field control of magnetic order above room temperature, *Nat Mater*, 13 (2014) 345-351.

[109] W. Eerenstein, M. Wiora, J.L. Prieto, J.F. Scott, N.D. Mathur, Giant sharp and persistent converse magnetoelectric effects in multiferroic epitaxial heterostructures, *Nat Mater*, 6 (2007) 348-351.

[110] Y.-H. Chu, L.W. Martin, M.B. Holcomb, M. Gajek, S.-J. Han, Q. He, N. Balke, C.-H. Yang, D. Lee, W. Hu, Q. Zhan, P.-L. Yang, A. Fraile-Rodriguez, A. Scholl, S.X. Wang, R. Ramesh, Electric-field control of local ferromagnetism using a magnetoelectric multiferroic, *Nat Mater*, 7 (2008) 478-482.

[111] C.A.F. Vaz, J. Hoffman, Y. Segal, J.W. Reiner, R.D. Grober, Z. Zhang, C.H. Ahn, F.J. Walker, Origin of the magnetoelectric coupling effect in Pb(Zr$_{0.2}$Ti$_{0.8}$)O$_3$/La$_{0.8}$Sr$_{0.2}$MnO$_3$ multiferroic heterostructures, *Physical Review Letters*, 104 (2010) 127202.

[112] E.Y. Tsymbal, A. Gruverman, V. Garcia, M. Bibes, A. Barthélémy, Ferroelectric and multiferroic tunnel junctions, *MRS Bulletin*, 37 (2012) 138-143.

[113] Y.W. Yin, M. Raju, W.J. Hu, X.J. Weng, X.G. Li, Q. Li, Coexistence of tunneling magnetoresistance and electroresistance at room temperature in La$_{0.7}$Sr$_{0.3}$MnO$_3$/(Ba, Sr)TiO$_3$/ La$_{0.7}$Sr$_{0.3}$MnO$_3$ multiferroic tunnel junctions, *Journal of Applied Physics*, 109 (2011) 07D915.

[114] D. Pantel, S. Goetze, D. Hesse, M. Alexe, Reversible electrical switching of spin polarization in multiferroic tunnel junctions, *Nat Mater*, 11 (2012) 289-293.

[115] M. Hambe, A. Petraru, N.A. Pertsev, P. Munroe, V. Nagarajan, H. Kohlstedt, Crossing an interface: Ferroelectric control of tunnel currents in magnetic complex oxide heterostructures, *Advanced Functional Materials*, 20 (2010) 2436-2441.

[116] P. Yu, W. Luo, D. Yi, J.X. Zhang, M.D. Rossell, C.-H. Yang, L. You, G. Singh-Bhalla, S.Y. Yang, Q. He, Q.M. Ramasse, R. Erni, L.W. Martin, Y.H. Chu, S.T. Pantelides, S.J. Pennycook, R. Ramesh, Interface control of bulk ferroelectric polarization, *Proceedings of the National Academy of Sciences*, 109 (2012) 9710-9715.

[117] D. Dijkkamp, T. Venkatesan, X.D. Wu, S.A. Shaheen, N. Jisrawi, Y.H. Min‐Lee, W.L. McLean, M. Croft, Preparation of Y-Ba-Cu oxide superconductor thin films using pulsed laser evaporation from high T_c bulk material, *Applied Physics Letters*, 51 (1987) 619-621.

[118] A. Ichimiya, P.I. Cohen., Reflection high-energy electron diffraction, *Cambridge University Press*, 2004.

[119] G. Binnig, C.F. Quate, C. Gerber, Atomic force microscope, *Physical Review Letters*, 56 (1986) 930-933.

[120] G. Haugstad, Overview of AFM, in: Atomic Force Microscopy, *John Wiley & Sons, Inc.*, 2012, pp. 1-32.

[121] G. Haugstad, Distance-Dependent Interactions, in: Atomic Force Microscopy, *John Wiley & Sons, Inc.*, 2012, pp. 33-90.

[122] L. van der PAUYV, A method of measuring specific resistivity and Hall effect of discs of arbitrary shape, *Philips Res. Rep.*, 13 (1958) 1-9.

[123] N. Nagaosa, J. Sinova, S. Onoda, A.H. MacDonald, N.P. Ong, Anomalous Hall effect, *Reviews of Modern Physics*, 82 (2010) 1539-1592.

[124] H.J.H. Ma, Z. Huang, W.M. Lü, A. Annadi, S.W. Zeng, L.M. Wong, S.J. Wang, T. Venkatesan, Ariando, Tunable bilayer two-dimensional electron gas in LaAlO$_3$/SrTiO$_3$ superlattices, *Applied Physics Letters*, 105 (2014) 011603.

[125] M. Viret, D. Vignoles, D. Cole, J.M.D. Coey, W. Allen, D.S. Daniel, J.F. Gregg, Spin scattering in ferromagnetic thin films, *Physical Review B*, 53 (1996) 8464-8468.

[126] M. Reis, Fundamentals of magnetism, *Elsevier*, 2013.

[127] Z.Q. Liu, D.P. Leusink, X. Wang, W.M. Lu, K. Gopinadhan, A. Annadi, Y.L. Zhao, X.H. Huang, S.W. Zeng, Z. Huang, A. Srivastava, S. Dhar, T. Venkatesan, Ariando, Metal-insulator transition in SrTiO$_{3-x}$ thin films induced by frozen-out carriers, *Physical Review Letters*, 107 (2011).

[128] X. Lin, G. Bridoux, A. Gourgout, G. Seyfarth, S. Kramer, M. Nardone, B. Fauque, K. Behnia, Critical doping for the onset of a two-band superconducting ground state in SrTiO$_{3-\delta}$, *Physical Review Letters*, 112 (2014).

[129] Y. Lee, C. Clement, J. Hellerstedt, J. Kinney, L. Kinnischtzke, X. Leng, S.D. Snyder, A.M. Goldman, Phase diagram of electrostatically doped SrTiO$_3$, *Physical Review Letters*, 106 (2011).

[130] M. Sato, Y. Soejima, N. Ohama, A. Okazaki, H.J. Scheel, K.A. Müller, The lattice constant vs. temperature relation around the 105 K transition of a flux-grown $SrTiO_3$ crystal, *Phase Transitions*, 5 (1985) 207-218.

[131] E.K.H. Salje, M.C. Gallardo, J. Jiménez, F.J. Romero, J.d. Cerro, The cubic-tetragonal phase transition in strontium titanate: excess specific heat measurements and evidence for a near-tricritical, mean field type transition mechanism, *Journal of Physics: Condensed Matter*, 10 (1998) 5535.

[132] H.W. Willemsen, R.L. Armstrong, P.P. Meincke, Thermal expansion near the displacive phase transition in $SrTi O_3$, *Physical Review B*, 14 (1976) 3644.

[133] R.O. Bell, G. Rupprecht, Elastic constants of strontium titanate, *Physical Review*, 129 (1963) 90-94.

[134] A. Biswas, P.B. Rossen, C.-H. Yang, W. Siemons, M.-H. Jung, I.K. Yang, R. Ramesh, Y.H. Jeong, Universal Ti-rich termination of atomically flat $SrTiO_3$ (001), (110), and (111) surfaces, *Applied Physics Letters*, 98 (2011) 051904.

[135] Z.Q. Liu, W.M. Lu, X. Wang, Z. Huang, A. Annadi, S.W. Zeng, T. Venkatesan, Ariando, Magnetic-field induced resistivity minimum with in-plane linear magnetoresistance of the Fermi liquid in $SrTiO_{3-x}$ single crystals, *Physical Review B*, 85 (2012).

[136] Z. Huang, K. Han, S. Zeng, M. Motapothula, A.Y. Borisevich, S. Ghosh, W. Lü, C. Li, W. Zhou, Z. Liu, M. Coey, T. Venkatesan, Ariando, The effect of polar fluctuation and lattice mismatch on carrier mobility at oxide interfaces, *Nano Letters*, 16 (2016) 2307-2313.

[137] Y.Z. Chen, N. Bovet, F. Trier, D.V. Christensen, F.M. Qu, N.H. Andersen, T. Kasama, W. Zhang, R. Giraud, J. Dufouleur, T.S. Jespersen, J.R. Sun, A. Smith, J. Nygård, L. Lu, B. Büchner, B.G. Shen, S. Linderoth, N. Pryds, A high-mobility two-dimensional electron gas at the spinel/perovskite interface of γ-Al_2O_3/$SrTiO_3$, *Nat Commun*, 4 (2013) 1371.

[138] J. Biscaras, N. Bergeal, A. Kushwaha, T. Wolf, A. Rastogi, R.C. Budhani, J. Lesueur, Two-dimensional superconductivity at a Mott insulator/band insulator interface $LaTiO_3$/$SrTiO_3$, *Nat Commun*, 1 (2010) 89.

[139] P. Delugas, A. Filippetti, V. Fiorentini, D.I. Bilc, D. Fontaine, P. Ghosez, Spontaneous 2-dimensional carrier confinement at the *n*-type $SrTiO_3$/$LaAlO_3$ interface, *Physical Review Letters*, 106 (2011).

[140] A. Dubroka, M. Roessle, K.W. Kim, V.K. Malik, L. Schultz, S. Thiel, C.W. Schneider, J. Mannhart, G. Herranz, O. Copie, M. Bibes, A. Barthelemy, C. Bernhard, Dynamical response and confinement of the electrons at the $LaAlO_3$/$SrTiO_3$ interface, *Physical Review Letters*, 104 (2010).

[141] M. Sing, G. Berner, K. Goss, A. Muller, A. Ruff, A. Wetscherek, S. Thiel, J. Mannhart, S.A. Pauli, C.W. Schneider, P.R. Willmott, M. Gorgoi, F. Schafers, R. Claessen, Profiling the interface electron gas of $LaAlO_3$/$SrTiO_3$ heterostructures with hard X-ray photoelectron spectroscopy, *Physical Review Letters*, 102 (2009).

[142] A. Annadi, Q. Zhang, X. Renshaw Wang, N. Tuzla, K. Gopinadhan, W.M. Lü, A. Roy Barman, Z.Q. Liu, A. Srivastava, S. Saha, Y.L. Zhao, S.W. Zeng, S. Dhar, E. Olsson, B. Gu, S. Yunoki, S. Maekawa, H. Hilgenkamp, T. Venkatesan, Ariando, Anisotropic two-dimensional electron gas at the $LaAlO_3$/$SrTiO_3$ (110) interface, *Nat Commun*, 4 (2013) 1838.

[143] J. Appel, Soft-mode superconductivity in $SrTiO_{3-x}$, *Physical Review*, 180 (1969) 508-516.

[144] Y. Segal, K.F. Garrity, C.A.F. Vaz, J.D. Hoffman, F.J. Walker, S. Ismail-Beigi, C.H. Ahn, Dynamic evanescent phonon coupling across the $La_{1-x}Sr_xMnO_3$/$SrTiO_3$ interface, *Physical Review Letters*, 107 (2011).

[145] G. Kresse, J. Hafner, *Ab initio* molecular dynamics for liquid metals, *Physical Review B*, 47 (1993) 558-561.

[146] G. Kresse, J. Hafner, *Ab initio* molecular-dynamics simulation of the liquid-metal-amorphous-semiconductor transition in germanium, *Physical Review B*, 49 (1994) 14251-14269.

[147] G. Kresse, D. Joubert, From ultrasoft pseudopotentials to the projector augmented-wave method, *Physical Review B*, 59 (1999) 1758-1775.

[148] P.E. Blochl, Projector augmented-wave method, *Physical Review B*, 50 (1994) 17953-17979.

[149] F. El-Mellouhi, E.N. Brothers, M.J. Lucero, G.E. Scuseria, Modeling of the cubic and antiferrodistortive phases of $SrTiO_3$ with screened hybrid density functional theory, *Physical Review B*, 84 (2011).

[150] F.Z. He, B.O. Wells, Z.G. Ban, S.P. Alpay, S. Grenier, S.M. Shapiro, W.D. Si, A. Clark, X.X. Xi, Structural phase transition in epitaxial perovskite films, *Physical Review B*, 70 (2004).

[151] T. Hernandez, C.W. Bark, D.A. Felker, C.B. Eom, M.S. Rzchowski, Localization of two-dimensional electron gas in $LaAlO_3/SrTiO_3$ heterostructures, *Physical Review B*, 85 (2012).

[152] T. Varga, A. Kumar, E. Vlahos, S. Denev, M. Park, S. Hong, T. Sanehira, Y. Wang, C.J. Fennie, S.K. Streiffer, X. Ke, P. Schiffer, V. Gopalan, J.F. Mitchell, Coexistence of weak ferromagnetism and ferroelectricity in the high pressure $LiNbO_3$-type phase of $FeTiO_3$, *Physical Review Letters*, 103 (2009) 047601.

[153] Y. Shi, Y. Guo, X. Wang, A.J. Princep, D. Khalyavin, P. Manuel, Y. Michiue, A. Sato, K. Tsuda, S. Yu, M. Arai, Y. Shirako, M. Akaogi, N. Wang, K. Yamaura, A.T. Boothroyd, A ferroelectric-like structural transition in a metal, *Nat Mater*, 12 (2013) 1024-1027.

[154] J. Fujioka, A. Doi, D. Okuyama, D. Morikawa, T. Arima, K.N. Okada, Y. Kaneko, T. Fukuda, H. Uchiyama, D. Ishikawa, A.Q.R. Baron, K. Kato, M. Takata, Y. Tokura, Ferroelectric-like metallic state in electron doped $BaTiO_3$, *Scientific Reports*, 5 (2015) 13207.

[155] I.A. Sergienko, V. Keppens, M. McGuire, R. Jin, J. He, S.H. Curnoe, B.C. Sales, P. Blaha, D.J. Singh, K. Schwarz, D. Mandrus, Metallic ``Ferroelectricity'' in the Pyrochlore $Cd_2Re_2O_7$, *Physical Review Letters*, 92 (2004) 065501.

[156] P. Ghosez, K.M. Rabe, Microscopic model of ferroelectricity in stress-free $PbTiO_3$ ultrathin films, *Applied Physics Letters*, 76 (2000) 2767-2769.

[157] J. Junquera, P. Ghosez, Critical thickness for ferroelectricity in perovskite ultrathin films, *Nature*, 422 (2003) 506-509.

[158] T. Tybell, C.H. Ahn, J.-M. Triscone, Ferroelectricity in thin perovskite films, *Applied Physics Letters*, 75 (1999) 856-858.

[159] D.D. Fong, G.B. Stephenson, S.K. Streiffer, J.A. Eastman, O. Auciello, P.H. Fuoss, C. Thompson, Ferroelectricity in ultrathin perovskite films, *Science*, 304 (2004) 1650-1653.

[160] C. Li, L. Huang, T. Li, W. Lü, X. Qiu, Z. Huang, Z. Liu, S. Zeng, R. Guo, Y. Zhao, K. Zeng, M. Coey, J. Chen, Ariando, T. Venkatesan, Ultrathin $BaTiO_3$-based ferroelectric tunnel junctions through interface engineering, *Nano Letters*, 15 (2015) 2568-2573.

[161] A. Kumar, U.C. Naithani, B.S. Semwal, Specific heat of $Ba_xSr_{1-x}TiO3$ ferroelectric perovskites, *British Ceramic Transactions*, 103 (2004) 153-157.

[162] D.J. Kim, J.Y. Jo, Y.S. Kim, Y.J. Chang, J.S. Lee, J.G. Yoon, T.K. Song, T.W. Noh, Polarization relaxation induced by a depolarization field in ultrathin ferroelectric $BaTiO_3$ capacitors, *Physical Review Letters*, 95 (2005).

[163] D.D. Fong, A.M. Kolpak, J.A. Eastman, S.K. Streiffer, P.H. Fuoss, G.B. Stephenson, C. Thompson, D.M. Kim, K.J. Choi, C.B. Eom, I. Grinberg, A.M. Rappe, Stabilization of monodomain polarization in ultrathin $PbTiO_3$ films, *Physical Review Letters*, 96 (2006).

[164] H. Tang, H.A. Sodano, Ultra high energy density nanocomposite capacitors with fast discharge using $Ba_{0.2}Sr_{0.8}TiO_3$ nanowires, *Nano Letters*, 13 (2013) 1373-1379.

[165] C.W. Bark, P. Sharma, Y. Wang, S.H. Baek, S. Lee, S. Ryu, C.M. Folkman, T.R. Paudel, A. Kumar, S.V. Kalinin, A. Sokolov, E.Y. Tsymbal, M.S. Rzchowski, A. Gruverman, C.B. Eom, Switchable induced polarization in $LaAlO_3/SrTiO_3$ heterostructures, *Nano Letters*, 12 (2012) 1765-1771.

[166] H.S. Lee, T. Mizoguchi, T. Yamamoto, S.J.L. Kang, Y. Ikuhara, First-principles calculation of defect energetics in cubic-$BaTiO_3$ and a comparison with $SrTiO_3$, *Acta Materialia*, 55 (2007) 6535-6540.

[167] J.P. Ibbetson, P.T. Fini, K.D. Ness, S.P. DenBaars, J.S. Speck, U.K. Mishra, Polarization effects, surface states, and the source of electrons in AlGaN/GaN heterostructure field effect transistors, *Applied Physics Letters*, 77 (2000) 250-252.

[168] Y. Chen, F. Trier, T. Kasama, D.V. Christensen, N. Bovet, Z.I. Balogh, H. Li, K.T.S. Thyden, W. Zhang, S. Yazdi, P. Norby, N. Pryds, S. Linderoth, Creation of high mobility two-dimensional electron gases via strain induced polarization at an otherwise nonpolar complex oxide interface, *Nano Letters*, 15 (2015) 1849-1854.

[169] J.P. Perdew, A. Zunger, Self-interaction correction to density-functional approximations for many-electron systems, *Physical Review B*, 23 (1981) 5048-5079.

[170] R. Pentcheva, W.E. Pickett, Avoiding the polarization catastrophe in $LaAlO_3$ overlayers on $SrTiO_3$ (001) through polar distortion, *Physical Review Letters*, 102 (2009) 107602.

[171] S.A. Pauli, S.J. Leake, B. Delley, M. Björck, C.W. Schneider, C.M. Schlepütz, D. Martoccia, S. Paetel, J. Mannhart, P.R. Willmott, Evolution of the interfacial structure of $LaAlO_3$ on $SrTiO_3$, *Physical Review Letters*, 106 (2011) 036101.

[172] J. Zhou, T.C. Asmara, M. Yang, G.A. Sawatzky, Y.P. Feng, A. Rusydi, Interplay of electronic reconstructions, surface oxygen vacancies, and lattice distortions in insulator-metal transition of $LaAlO_3/SrTiO_3$, *Physical Review B*, 92 (2015) 125423.

[173] M.F. Chisholm, W. Luo, M.P. Oxley, S.T. Pantelides, H.N. Lee, Atomic-scale compensation phenomena at polar interfaces, *Physical Review Letters*, 105 (2010) 197602.

[174] N.A. Hill, Why are there so few magnetic ferroelectrics?, *The Journal of Physical Chemistry B*, 104 (2000) 6694-6709.

[175] X. Liu, M. Bauer, H. Bertagnolli, E. Roduner, J. van Slageren, F. Phillipp, Structure and magnetization of small monodisperse platinum clusters, *Physical Review Letters*, 97 (2006) 253401.

[176] B. Sampedro, P. Crespo, A. Hernando, R. Litrán, J.C. Sánchez López, C. López Cartes, A. Fernandez, J. Ramírez, J. González Calbet, M. Vallet, Ferromagnetism in fcc twinned 2.4 nm size Pd nanoparticles, *Physical Review Letters*, 91 (2003) 237203.

[177] S.Y. Huang, X. Fan, D. Qu, Y.P. Chen, W.G. Wang, J. Wu, T.Y. Chen, J.Q. Xiao, C.L. Chien, Transport magnetic proximity effects in Platinum, *Physical Review Letters*, 109 (2012).

[178] Y.M. Lu, Y. Choi, C.M. Ortega, X.M. Cheng, J.W. Cai, S.Y. Huang, L. Sun, C.L. Chien, Pt magnetic polarization on $Y_3Fe_5O_{12}$ and magnetotransport characteristics, *Physical Review Letters*, 110 (2013) 147207.

[179] S. Shimizu, K.S. Takahashi, T. Hatano, M. Kawasaki, Y. Tokura, Y. Iwasa, Electrically tunable anomalous Hall effect in Pt thin films, *Physical Review Letters*, 111 (2013).

[180] I.K. Jeong, S. Lee, S.-Y. Jeong, C.J. Won, N. Hur, A. Llobet, Structural evolution across the insulator-metal transition in oxygen-deficient $BaTiO_{3-\delta}$ studied using neutron total scattering and Rietveld analysis, *Physical Review B*, 84 (2011) 064125.

[181] J.S. Kim, S.S.A. Seo, M.F. Chisholm, R.K. Kremer, H.U. Habermeier, B. Keimer, H.N. Lee, Nonlinear Hall effect and multichannel conduction in $LaTiO_3/SrTiO_3$ superlattices, *Physical Review B*, 82 (2010) 201407.

[182] N. Seriani, W. Pompe, L.C. Ciacchi, Catalytic oxidation activity of Pt_3O_4 surfaces and thin films, *The Journal of Physical Chemistry B*, 110 (2006) 14860-14869.

[183] G. Kresse, J. Furthmüller, Efficient iterative schemes for *ab initio* total-energy calculations using a plane-wave basis set, *Physical Review B*, 54 (1996) 11169-11186.

[184] H.J. Monkhorst, J.D. Pack, Special points for Brillouin-zone integrations, *Physical Review B*, 13 (1976) 5188-5192.

[185] Z. Wen, C. Li, D. Wu, A.D. Li, N.B. Ming, Ferroelectric-field-effect-enhanced electroresistance in metal/ferroelectric/semiconductor tunnel junctions, *Nature Materials*, 12 (2013) 617-621.